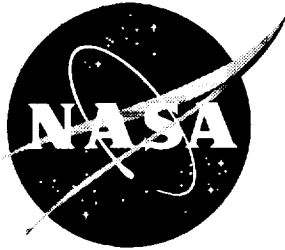


NASA/TP-1999-209541



# Navier-Stokes Simulation of Several High-Lift Reference H Configurations

*Wendy B. Lessard*  
*Langley Research Center, Hampton, Virginia*

---

December 1999

## The NASA STI Program Office . . . in Profile

Since its founding, NASA has been dedicated to the advancement of aeronautics and space science. The NASA Scientific and Technical Information (STI) Program Office plays a key part in helping NASA maintain this important role.

The NASA STI Program Office is operated by Langley Research Center, the lead center for NASA's scientific and technical information. The NASA STI Program Office provides access to the NASA STI Database, the largest collection of aeronautical and space science STI in the world. The Program Office is also NASA's institutional mechanism for disseminating the results of its research and development activities. These results are published by NASA in the NASA STI Report Series, which includes the following report types:

- **TECHNICAL PUBLICATION.** Reports of completed research or a major significant phase of research that present the results of NASA programs and include extensive data or theoretical analysis. Includes compilations of significant scientific and technical data and information deemed to be of continuing reference value. NASA counterpart of peer-reviewed formal professional papers, but having less stringent limitations on manuscript length and extent of graphic presentations.
- **TECHNICAL MEMORANDUM.** Scientific and technical findings that are preliminary or of specialized interest, e.g., quick release reports, working papers, and bibliographies that contain minimal annotation. Does not contain extensive analysis.
- **CONTRACTOR REPORT.** Scientific and technical findings by NASA-sponsored contractors and grantees.

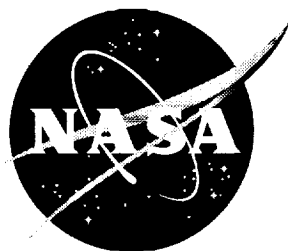
- **CONFERENCE PUBLICATION.** Collected papers from scientific and technical conferences, symposia, seminars, or other meetings sponsored or co-sponsored by NASA.
- **SPECIAL PUBLICATION.** Scientific, technical, or historical information from NASA programs, projects, and missions, often concerned with subjects having substantial public interest.
- **TECHNICAL TRANSLATION.** English-language translations of foreign scientific and technical material pertinent to NASA's mission.

Specialized services that complement the STI Program Office's diverse offerings include creating custom thesauri, building customized databases, organizing and publishing research results . . . even providing videos.

For more information about the NASA STI Program Office, see the following:

- Access the NASA STI Program Home Page at <http://www.sti.nasa.gov>
- Email your question via the Internet to [help@sti.nasa.gov](mailto:help@sti.nasa.gov)
- Fax your question to the NASA STI Help Desk at (301) 621-0134
- Telephone the NASA STI Help Desk at (301) 621-0390
- Write to:  
NASA STI Help Desk  
NASA Center for AeroSpace Information  
7121 Standard Drive  
Hanover, MD 21076-1320

NASA/TP-1999-209541



# Navier-Stokes Simulation of Several High-Lift Reference H Configurations

*Wendy B. Lessard*  
*Langley Research Center, Hampton, Virginia*

National Aeronautics and  
Space Administration

Langley Research Center  
Hampton, Virginia 23681-2199

---

December 1999

---

Available from:

NASA Center for AeroSpace Information (CASI)  
7121 Standard Drive  
Hanover, MD 21076-1320  
(301) 621-0390

National Technical Information Service (NTIS)  
5285 Port Royal Road  
Springfield, VA 22161-2171  
(703) 605-6000

## Summary

The objective of this study is to predict the subsonic flow field around several High Speed Research Reference H configurations at various pitch and yaw angles. The configurations achieve a high lift-to-drag ratio with leading- and trailing-edge flap deflections that are optimized to minimize flow separation around the leading edge and flap hinge lines. A sequence of structured-viscous grids was generated for the high-lift Reference H configuration. The first grid modeled the wing-body high-lift geometry, and the second grid incorporated the nacelles and the horizontal tail. The third grid modeled the full-span geometry for sideslip calculations, and was obtained by mirroring a coarser version of the second grid. The CFL3D code, a Reynolds averaged, thin-layer Navier-Stokes flow solver for structural grids, was used for the flow solver and modeled the free-air Reference H high-lift configuration at wind tunnel conditions of Mach number 0.24 and Reynolds number of  $1.4 \times 10^5$  per in. Pitch sweeps were performed at angles of attack from  $6^\circ$  to  $15^\circ$ . Sideslip angle sweeps at  $0^\circ \leq \beta \leq +18^\circ$  were performed at an angle of attack of  $8^\circ$ .

The lateral and longitudinal performance characteristics were well predicted and very good force and moment comparisons are seen. The pressure distributions show generally good comparison and trend at the lower angles of attack; however, comparisons diverge when the predicted flow on the outboard portion of the wing becomes extensively separated, which occurs at about  $12^\circ$  angle of attack. A very complex multiple vortical system is predicted at the higher angles of attack. Also, at the higher sideslip angles, an extensive area of stalled flow forms on the left side of the vertical tail. Postprocessing of the numerical solutions provided detailed surface and off-surface flow quantities, not obtained in the wind tunnel. The plotted off-surface pressure contours of the computational vortical flow field was very insightful in interpreting the wind tunnel data and provided a comprehensive three-dimensional understanding of the flow.

## Introduction

The development of technologies for an economically feasible high speed civil transport by NASA and the U.S. aerospace industry is currently underway, and is the main focus for the High Speed Research program. Similar to the Supersonic Cruise Research program, which was initiated in July 1972 by NASA, the High Speed Research program has focused on the potential benefits and trade-offs of advancements in aerodynamic efficiency, structures and materials, propulsion systems, and stability and control requirements applied to advanced supersonic cruise aircraft concepts. From a performance point of view, the aircraft would be designed for high

aerodynamic efficiency in supersonic cruise and have good low-speed characteristics. For efficient supersonic cruise, the aircraft must have highly swept, low-aspect-ratio wings; however, this type of configuration is inefficient in the subsonic flight regimes. During take-off and approach, the flow separates from the leading edge of the wing and forms a vortex system, which causes an increase in drag. The additional thrust required from the engines to overcome the increased drag and the low speed performance deficiencies, generates an unacceptable high level of engine noise. The environmental impact of the engine-generated noise can be minimized by reducing flow separation, which maximizes the take-off lift-to-drag ratio. The environmental impact is minimized by incorporating special leading- and trailing-edge devices or attached-flow flaps onto the aircraft.

The focus of this investigation is the accurate prediction of the subsonic flow field about a Reference H model with leading- and trailing-edge flaps using a proven viscous numerical method. Computations were performed at various pitch and yaw angles using structured viscous grids for the wing-body, for the wing-body with nacelles and horizontal tail, and for the wing-body with nacelles and horizontal and vertical tail configurations.

## Symbols and Abbreviations

$b$	wing span, in.
$C_D$	drag coefficient, $\text{Drag}/q_\infty S$
$C_L$	lift coefficient, $\text{Lift}/q_\infty S$
$C_l$	rolling-moment coefficient (positive right wing down), $\text{Rolling moment}/(q_\infty S b)$ , body axis
$C_m$	pitching-moment coefficient about $0.50c$ (positive nose up), $\text{Pitching moment}/(q_\infty S c)$
$C_{m,0}$	pitching-moment coefficient at zero lift
$C_n$	yawing-moment coefficient (positive nose right), $\text{Yawing moment}/(q_\infty S b)$ , body axis
$C_p$	static pressure coefficient, $(p - p_\infty)/q_\infty$
$C_Y$	side force coefficient (positive right), $\text{Side force}/(q_\infty S)$
$c$	mean aerodynamic chord, in.
$c_l$	local chord, in.
$i,j,k$	grid index
$M$	free-stream Mach number
$p$	static pressure, psi
$p_t$	total pressure, psi
$p_\infty$	free-stream static pressure, psi
$q_\infty$	free-stream dynamic pressure, psi

$Re_L$	Reynolds number per unit length, $L/in.$
$S$	reference area, $in^2$
$V_\infty$	free-stream velocity, $in/sec$
$x_l$	local $x$ coordinate, zero at leading edge, $in.$
$x/c_l$	fraction of local chord
$x, y, z$	body axis coordinates, $in.$
$y^+$	law-of-the-wall coordinate
$y/(b/2)_l$	fraction of local semispan
$\alpha$	angle of attack, $deg$
$\beta$	angle of sideslip, $deg$
$\delta_{LE}$	leading-edge flap deflection angle (positive down), $deg$
$\delta_{TE}$	trailing-edge flap deflection angle (positive down), $deg$
$\xi, \eta, \zeta$	curvilinear coordinates
Abbreviations:	
config1	wing-body configuration
config2	wing-body with nacelle and horizontal tail configuration
config3	full-span wing-body with nacelle and horizontal and vertical tail configuration
LE	leading edge
TE	trailing edge
MBL	model buttline station, $in.$
MFS	model fuselage station, $in.$
MW	megaword

## Test and Model

The NASA Langley 14- by 22-Foot Subsonic Tunnel is a closed circuit, single-return atmospheric tunnel. The test section is 14.5 ft high by 21.75 ft wide and was configured with closed walls and ceiling for this test. A more detailed description of the wind tunnel is given in reference 1. The computational results obtained in this report are compared with experimental data from two separate wind tunnel entries with test numbers T421 and T437. (Data is in computer storage at the Subsonic Aerodynamics Branch and is available from the author.) Unpublished experimental wing-body data from T421 were compared with computational data for the wing-body high-lift Reference H configuration. Unpublished data from T437 were used for comparison to the computational data for the wing-body with nacelles and horizontal tail and wing-body with nacelles and horizontal and vertical tail for the sideslip calculations. The wind tunnel data (surface pressures and force and moment data) from both tests were obtained at a nominal dynamic pressure of 0.60 psi, which produced a test Mach number of approximately 0.24 with slight varia-

tions due to temperature changes and a test  $Re_L$  of approximately  $1.4 \times 10^5$  per  $in.$  Pitch sweeps were performed at angles of attack from  $-4^\circ$  to  $+30^\circ$ . Sideslip angle sweeps at  $-30^\circ \leq \beta \leq +30^\circ$  were performed at angles of attack of  $8^\circ$ ,  $10^\circ$ , and  $12^\circ$ .

A photograph of the model mounted in the tunnel is shown in figure 1. The model is the 0.06-scale Reference H high-lift configuration designed by the Boeing Commercial Aircraft Group. The model was mounted on a close-coupled tandem post mount, which was composed of a main post and a pitch strut. The same post was used for both T421 and T437. A six-component, strain-gauge, internal balance measured the forces and moments. A spring-loaded sliding seal was fitted to the inside of the model to minimize the opening around the post mount. A two-point, floor-mounted pedestal support system attached near the model aerodynamic center provided yaw rotation about the vertical axis for sideslip variation and provided pitch rotation about the front support point for angle-of-attack variation. The experimental data were not corrected for any strut and support interference effects. Forebody grit was applied around the nose and along the lower sides of the forebody; there was no grit on the wing. A three-view sketch of the model is presented in figure 2. Table 1 presents a list of the model components and their description. The wing is projected to the centerline (see the dotted lines in fig. 2) to determine reference area and root chord.

Table 1. Geometric Characteristics of Model

Wing	
Aspect ratio	2.367
Reference area, $in^2$	3680.64
Reference mean aerodynamic chord, $in.$	61.937
Span, $in.$	93.343
Root chord (at the fuselage centerline), $in.$	116.054
Outboard break chord, $in.$	28.282
Tip chord, $in.$	7.599
Location of 0.50c	MFS 126.354, MBL 14.486
Inboard LE sweep, $deg$	+75.9
Inboard TE sweep, $deg$	-50.2
Mid LE sweep, $deg$	+68.5
Mid TE sweep, $deg$	-8.8
Outboard LE sweep, $deg$	+48.0
Outboard TE sweep, $deg$	+10.4
Vertical tail	
Exposed span, $in.$	13.49
Exposed aspect ratio	0.864
Exposed root chord	25.392
Tip chord, $in.$	5.978
Horizontal tail	
Exposed span	10.847 $in./side$
Exposed aspect ratio	1.297
Exposed root chord, $in.$	26.752
Tip chord, $in.$	6.702

The pressure ports are located on the Reference H model as depicted in figure 3. Though the pressure port locations for the upper surface are depicted on the right wing and the lower port locations are depicted on the left wing, the model had both upper and lower ports on the left wing. The experimental pressure distributions at the seven designated MFS's and five designated MBL's are used to correlate with the computational results.

## Computational Grids

The grids used in this study were provided by the Langley-sponsored Geometry Laboratory, which is an on-site contracting service. Each grid was generated in several stages. First the Initial Graphics Exchange Specification data are read into the Integrated Computer-Aided Engineering and Manufacturing software system where the grid block topology is set up and the coarse Euler volume grids are generated. The block faces are refined by GRIDGEN2D (an interactive software program used to generate grids) to ensure smoothness and orthogonality. Additional grid points are distributed in the boundary layer for the viscous spacing requirement and the volume grids are generated accordingly.

Several grids of the high-lift Reference H configuration were generated, all of which had leading-edge flaps deflected at  $30^\circ$  normal to the hinge line,  $\delta_{LE} = 30^\circ$ , and the trailing-edge flaps deflected normal to the hingeline at  $10^\circ$ ,  $\delta_{TE} = 10^\circ$ . Two of the configurations modeled the semispan: the wing-body (config1) and the wing-body with nacelles and horizontal tail (config2). The third grid modeled the full span wing-body with nacelles and empennage (config3) for the sideslip calculations. A description of the geometries and conditions solved are tabulated in table 2, where a  $\checkmark$  denotes the presence of a component. The wing thickness transitions from a blunt leading-edge airfoil to a sharp leading-edge airfoil at the planform break, which is located at the 24.35 in. MBL. The wind tunnel model makes this transition abruptly, resulting in a sharp step; however, the numerical model uses a linear interpolation over a region of 0.30 in. to smooth this sharp transition region and to simplify the grid generation. The leading-edge flaps immediately inboard and outboard of the crank are blended together so there are no spaces between the flaps. The wind tunnel model was also blended together in this region with a filler material. The numerical grid did not include the wind tunnel walls nor did it model the post support, which was used to mount the model in the tunnel; all calculations were done in free air. A far-field view of the surface and volume grid illustrating the overall blocking structure, as well as the grid topology, can be seen in figure 4. The forebody is a C-O topology and the wing and wake region have a C-H topology. A near-field view of the surface is shown in figure 5 and reveals the complex

blocking structure around the trailing-edge flaps and nacelles. The blocking strategy on the lower surface around the nacelles is shown in more detail in figure 6. The grid geometry on the flaps and flap edges is depicted in figure 7, and a close-up view (insert) shows the side-of-flap region and flow-through region. An innovative multiblock strategy was employed at the trailing edge of the wing, which allowed one-to-one matching across the trailing-edge flap block interfaces.

Table 2. Configuration Geometries and Conditions

Geometry	Wing-body	Nacelles	Horizontal tail	Vertical tail	Condition
config1	$\checkmark$				$\alpha = 6, 8, 10, 12, 15^\circ$
config2	$\checkmark$	$\checkmark$	$\checkmark$		$\alpha = 8, 10, 12^\circ$
config3	$\checkmark$	$\checkmark$	$\checkmark$	$\checkmark$	$\alpha = 8^\circ$ $\beta = 0, 6, 12, 18^\circ$

The full-span surface grid configuration of the Reference H  $\delta_{LE} = 30^\circ$ ,  $\delta_{TE} = 10^\circ$  with nacelles and empennage is depicted in figure 8. This grid was generated by first coarsening the grid of config2. The reduction in points was necessary to ensure that the full-span grid could be run in the maximum memory category; compromises are discussed in the section "Results." This point reduction affected the forebody, the wing upstream of the trailing-edge flap hingelines, and the wake regions. All other blocks remained the same. The streamwise cuts on the wing were decreased by 8, and the grid points in the normal directions were reduced by 8. The forebody grid was reduced by 48 points circumferentially and 8 points in the normal direction. The upper and lower wake regions were decreased by 69 points circumferentially and 8 points in the normal direction. These adjustments resulted in the reduction of over a million grid points for the semispan grid. The coarsened grid was then mirrored to the other side and point-to-point connections were then specified in the longitudinal direction at the fuselage centerline. The vertical tail was also incorporated onto the geometry. Table 3 summarizes the number of blocks, number of grid points, and number of patched and point-to-point continuous interfaces for each of the above mentioned configurations.

Table 3. Number of Configuration Blocks, Grid Points, and Interfaces

Geometry	Blocks	Grid points	Continuous interfaces	
			Patched	Point-to-point
config1	14	3,988,514	2	23
config2	37	4,595,343	38	83
config3	74	7,085,708	96	163

## Computational Method

The subsonic flow field about config1, config2, and config3 was simulated using CFL3D. This code solves Reynolds averaged, thin-layer, three-dimensional, time-dependent, compressible Navier-Stokes equations in conservation law form. More details about the computational method and code can be found in reference 2. The interpolated coefficient values between the patched interfaces were determined using RONNIE (ref. 3) and PATCHER (ref. 4). The RONNIE code was used for all calculations involving config1 and config2, and the PATCHER code was used for the full-span calculations on config3.

Viscous cell spacing normal to the forebody, wing-fuselage-afterbody and wake region was  $2 \times 10^{-6} c$ , which was required for  $y^+ = 1.0$  to accurately simulate turbulence. A single exponential function was used for grid expansion. To minimize the total number of grid points, viscous spacing was not specified around the nacelle surfaces or at the sides of the trailing-edge flaps. The coarse grid spacing at the side of trailing-edge flaps is  $7.3 \times 10^{-4} c$ . The far-field boundary extends approximately  $5.8c$  upstream of the fuselage,  $5c$  circumferentially away from the center line, and  $3.7c$  downstream of the afterbody. Although the model was strut mounted in the wind tunnel, the computations did not simulate the strut; all computations done were free-air calculations. As previously noted, the experimental data were not corrected for any strut and support interference effects. The conditions of no-slip and impermeability with zero-normal-gradient for pressure and temperature are imposed at the solid boundaries. Symmetry conditions are used along the vertical plane of symmetry for the semispan grids. One-dimensional characteristic inflow/outflow boundary conditions are used in the far field. Flow-through boundary conditions are specified between the trailing-edge flaps and at the nacelle inlet and exit.

The location of flow transition was not experimentally determined and therefore unknown. The flow was assumed to be fully turbulent for all calculations. The field equation turbulence model of Spalart-Allmaras was attempted but the model was unable to handle the singular lines in the triangular-shaped regions around the trailing-edge flaps. The algebraic turbulence model developed by Baldwin and Lomax was therefore used in this investigation. For separated flow regions, the method of Degani and Schiff was used to determine the proper length scale for the turbulence model. The turbulent viscous terms were calculated only in the direction normal to the wall.

All computations were performed on the numerical aerodynamic simulation Cray-2 computer, located at Ames Research Center. Convergence was accelerated

using mesh sequencing and three levels of multigrid. The residual and  $C_L$  history plots are shown in figure 9 for the Reference H config2 at  $\alpha = 10^\circ$ . The mesh sequencing process consists of approximately 1700 iterations computed on the coarse level, 1500 iterations computed on the medium level, and 1000 iterations computed on the fine level. An almost 3.5 order of magnitude reduction in the residual is observed for the config2 case. Config1 results showed similar convergence histories. The residual and  $C_L$  history plots for the config3 case at  $\beta = 6^\circ$  and  $\alpha = 8^\circ$  are shown in figure 10, and a similar mesh sequencing strategy was followed. A 3.0 order of magnitude decrease is noted for the config3 case. The algorithm takes approximately 10  $\mu$ sec per iteration per grid point. At approximately 37 words per grid point, the config3 case requires 262 MW of memory and the config1 case requires about 170 MW. A typical config2 case took about 18 hours to converge and config3 took about 25 hours.

## Results

The computational results for the three configurations are presented below. The general format is presentation, discussion, and comparison of the computational data and experimental data. Comparison of forces and moments, as well as surface pressure distributions, are discussed for each case. Detailed computational off-surface and surface flow visualization are presented to help explain the experimental data.

### Config1 Results

The force and moment comparisons for config1 at  $6^\circ \leq \alpha \leq 15^\circ$  are shown in figure 11. The computational results compare well with experiment, and the trends are predicted well. Computational results show that at about  $\alpha = 12^\circ$ , a vortex-dominated flow develops. The vortex-dominated flow causes the nonlinear  $C_L$  characteristics, increase in drag, and nose down pitching moment due to greater lift aft of the moment center. A notable difference between the computational and experimental results occurs at the higher angles of attack ( $\alpha > 11^\circ$ ) and at  $\alpha = 6^\circ$ . The computational lift and drag values are higher than the experiment; this difference is most likely due to the greater influence of the predicted vortical flow. Unlike the experimental  $C_m$  curve, which is relatively flat for  $\alpha < 8^\circ$ , the computations show a decrease in  $C_m$  at  $\alpha = 6^\circ$ .

Computational pressure distributions are compared with experiment in figures 12–21. As discussed previously,  $C_p$  data for the seven MFS and five MBL (fig. 3) are plotted. The computational  $C_p$  distributions on the wing and leading- and trailing-edge flap surfaces match well with experiment for the lower angles of attack. The



comparison between computation and experiment begins to show poor agreement somewhere around  $\alpha = 12^\circ$ . In particular, the outboard pressures on the wing, including the crank, show poor comparisons at  $\alpha = 12^\circ$  and  $15^\circ$ . The surface flow computations indicate a rather massive region of separated flow, and the effects of this separation are seen as suction peak reductions (see figs. 18 and 20 at  $x \geq 126.86$  in. and fig. 21 at  $y \geq 28.90$  in.). These reductions in the suction peaks occur directly as a result of vortex dissipation over the wing near the trailing edge, and will be presented and discussed later. These phenomena do not occur experimentally.

To show the flow physics on this high-lift high-speed civil transport, six crossflow planes showing total pressure  $p_t$  contours are plotted on the Reference H upper surface and forebody for  $\alpha = 6^\circ, 8^\circ, 10^\circ, 12^\circ$ , and  $15^\circ$  (figs. 22–26). The planes shown represent actual grid stations and correspond to the following streamwise dimensions, which are referenced at the wing leading edge:  $x = 70.2$  in.,  $84.2$  in.,  $103.8$  in.,  $120.2$  in.,  $131.8$  in., and  $154.7$  in. At  $\alpha = 6^\circ$  and  $8^\circ$ , the flow over the wing is attached, except for a small inboard vortex and a tip vortex (labeled as A and B in figs. 22 and 23). The inboard vortex emanates from the wing apex and travels downstream near the wing-fuselage junction. The contour lines show a possible vortex forming on the fuselage, but examination of the velocity vectors in that region only reveals that the flow is just turning sharply.  $p_t$  contours plotted in crossflow planes at  $\alpha = 10^\circ$  are shown in figure 24. A more interesting and complex flow field develops at this angle of attack. A vortex (C) emanates from the forebody and forms over the fuselage. In addition to the apex vortex which appears in the two previous angle-of-attack cases, a weak elongated vortex (D) separates from the leading-edge flap hingeline and forms just outboard of the apex vortex. This vortex first appears at about  $x = 120.2$  in. and continues to the trailing edge. Another small flat vortex (E) forms at the crank and travels along the leading-edge flap until it reaches the wing tip and merges with the tip vortex (B).

The flow field characteristics just described are similar for the  $\alpha = 12^\circ$  case; however, dissipation of the combined crank and leading-edge vortices (E) over the outboard section of the wing causes extensive flow separation (F and G). At  $\alpha = 15^\circ$  (fig. 26), a vortex (A) emanates from the wing apex similar to the lower angles of attack; however, the vortex is larger in shape and magnitude and its footprint traces a more outboard path on the wing due to the increased spanwise flow. Just adjacent to and outboard of the apex vortex, a leading-edge flap hinge line vortex develops (D), which is also stronger and more defined than the one predicted at  $\alpha = 10^\circ$  and  $12^\circ$ . A vortex (C) forms on the forebody and remains confined to the upper fuselage, and is similar in shape to

the one at the lower angles of attack. Just upstream from the crank, another vortex (not shown) separates from the leading edge of the wing and remains on the flap. This vortex does not remain distinct very long since it merges quickly with the crank vortex. This combined outboard crank and leading-edge vortex elongates and moves onto the upper surface of the wing as it propagates downstream and forms vortex H.

## Config2 Results

The nacelles and horizontal tail were added to config1 to create config2. The force and moment data are plotted with experiment in figure 27 at  $\alpha = 8^\circ, 10^\circ$ , and  $12^\circ$ , and very good comparisons are seen. The experimental  $C_L$ ,  $C_D$ , and  $C_m$  curves are very similar to those for config1 shown in figure 11. It should be noted that the wind tunnel model used for config2 had the empennage attached; however, the computational model only had the horizontal tail. The influence of the vertical tail on the longitudinal performance and wing surface pressures are expected to be minimal so numerical modeling of the vertical tail was not included. The numerical  $C_p$  distributions are compared to experiment in figures 28–33 for  $\alpha = 8^\circ, 10^\circ$ , and  $12^\circ$ . A cross section of the geometry that shows the location of nacelles and trailing-edge flaps are included for the last three fuselage stations. This cross section facilitates the interpretation of the pressure plots that have the spikes around the nacelles and flap edges. Comparison with experiment is good for  $\alpha = 8^\circ$  and  $10^\circ$ , and in general the  $C_p$  distributions are similar to the Reference H wing-body configuration, which suggests a similar flow pattern for each.

The effect of the nacelles influences the surface pressures close to the trailing edge of the wing since the trailing-edge flaps are deflected. As expected, higher  $C_p$  values are seen on the lower surface in the vicinity of the nacelles (particularly at  $x = 143.39$  in.). The computational  $C_p$  results for config1 and config2 at  $x > 135.13$  in. (figs. 18 and 32) and for  $y = 28.90$  in. (figs. 19 and 33) show nonsmooth pressure distributions and poor comparisons with experiment. These nonsmooth computational pressures may be due to some flow unsteadiness that occurred as a consequence of the flow separation on the outboard portion of the wing. The associated computational convergence oscillations are more apparent for config2 and may be due to grid definition. To accommodate the extra grid points required by the nacelles and horizontal tail, fewer points were used in the wake region than for the wing-body alone (config1). The effect of using fewer points in the wake may have influenced the upstream wing pressures to a certain extent.

Off-surface  $C_p$  contours are depicted in figures 34–36 for  $\alpha = 8^\circ, 10^\circ$ , and  $12^\circ$ , respectively.

Figures 34(a), 35(a), and 36(a) depict results of config1 and figures 34(b), 35(b), and 36(b) show results for config2. Each cross-sectional plane was obtained by slicing through the volume grid and solution at a specified constant  $x$  station. These planes are located at  $x = 150$  in. (cuts across the trailing-edge flaps near the wing tip),  $x = 180$  in. (cuts through the fuselage between the wing trailing edge and the empennage), and 208 in. (cuts through the tip chord of the horizontal tail).

Analysis of the off-surface flow of config1 and config2 reveal similar vortical flow patterns at  $y \leq 23$  in. In this region, the nacelles generally reduce the negative pressure values in the vortical cores at  $x = 180$  in. and affect the locations of the vortices at  $x = 208$  in. Outboard of that region, the vortical patterns generated by each configuration become more dissimilar. Some of this dissimilarity may be due to the difference in the wake grid density as previously mentioned. The biggest discrepancy in the vortical flow patterns between the nacelle on and off case is evident for  $\alpha = 12^\circ$  at  $y > 16$  in. and at  $x = 150$  in. and 208 in., as shown in figures 36(a) and 36(b). It appears that the horizontal tail has little effect on the flow field at all angles of attack when compared to the tail-off contours. In fact, the local flow characteristics appear to remain almost the same with increasing angle of attack.

### Config3 Results

The results for config3 are presented in figures 37–52. As previously stated, config3 modeled the full-span high-lift Reference H geometry including nacelles and vertical and horizontal tails. Computational results were obtained for  $\beta = 0^\circ, 6^\circ, 12^\circ$ , and  $18^\circ$ , at  $\alpha = 8^\circ$ . Force and moment comparisons between experiment and computation are shown in figure 37, and fairly good comparisons are seen. The experimental  $C_L$  values remain almost constant from  $-3^\circ \leq \beta \leq 3^\circ$  and then a gradual decrease in lift occurs over the remaining range of sideslip angles. The computational results predict the same trend but a more gradual decrease in lift is predicted. The numerical  $C_D$  and  $C_m$  results also compare well with experiment; however, since there is an almost constant difference between the computational and experimental pitching moment, a  $C_{m,0}$  shift is suspected.

There are no significant changes in the experimental  $C_D$  and  $C_m$  curves until the sideslip angle exceeds  $15^\circ$ . At  $\beta > 15^\circ$ , an increase in drag occurs, which peaks at  $\beta = 21^\circ$ . The pitching-moment curve shows decreasing slope and transitions to a steep positive slope at  $15^\circ \leq \beta \leq 21^\circ$ . This change in slope is most likely due to an increase in the vortical flow forward of the moment reference center (0.05c), which causes a nose-up pitching moment and an increase in drag. The measured side force

coefficient  $C_Y$  values for  $\beta \leq 15^\circ$  are linear for that range; however, the predicted side forces, which are generally underpredicted, depict a nonlinear trend. The numerical rolling moment  $C_l$  and yawing moment  $C_n$  compare well with experiment. Consistent with the  $C_D$  and  $C_m$  curve characteristics in the interval,  $15^\circ \leq \beta \leq 21^\circ$ , the  $C_l$  and  $C_n$  curves show an increase in slope. A negative  $C_l$  slope is seen for  $0^\circ \leq \beta \leq 21^\circ$  and means that the aircraft is directionally stable in roll due to sideslip. Likewise the positive  $C_n$  curve slope over the same sideslip interval indicates that the aircraft is directionally stable in yaw. The fuselage and nacelles may contribute to or detract from the airplane lateral stability, depending on whether the side force of these components acts below the center of gravity. The side force acting on the vertical tail diminishes the bank angle at the lower yaw angles and produces stabilizing characteristics. However, at the larger sideslip angles such as those greater than or equal to  $18^\circ$ , the flow on the left side of vertical tail stalls and produces destabilizing characteristics.

The  $C_p$  comparisons for config3 are presented in figures 38–47. The spanwise distance plotted on the abscissa ranges from  $-1.0$  to  $+1.0$ , in which  $-1.0$  to  $0$  represents the left side of the wing and  $0$  to  $+1.0$  represents the right side. Good comparisons are seen for the  $\beta = 0^\circ$  case shown in figures 38 and 39. As previously mentioned, the grid for config3 was coarser in some areas compared to the grid for config2. A detailed description of the grids for each configuration was discussed in the section "Computational Grids." A grid study was not attempted here since any grid refinement would exceed the maximum memory allocation. Since the calculations had already been done for config2 at  $\alpha = 8^\circ$  and  $\beta = 0^\circ$ , the config2 results are compared to the config3 results, and the effect of the mesh on the solution and flow physics is addressed. The effect of grid density on the solution is studied by plotting the  $C_p$  distributions for both cases together as shown in figures 40 and 41. The numerical  $C_p$  distributions are the same though a small  $y$  shift of the inboard suction peak is predicted for config2 at  $x = 135.13$  in. and  $x = 143.39$  in. Most of the notable differences occur on the outboard portion of the wing near the trailing edge and wing tip. Examination of the pressures at the buttock stations in figure 41 shows differences occurring at the trailing edge ( $y = 28.90$  in. and  $y = 34.52$  in.) as well as near the wing tip at  $y = 42.0$  in.

The  $C_p$  comparisons for  $\beta = 6^\circ, 12^\circ$ , and  $18^\circ$  for config3 are shown in figures 42–47. Note the asymmetric  $C_p$  distributions characterized by higher suction peaks on the right wing compared to the left wing, which causes a negative rolling moment (see fig. 37). The increased effect of the fuselage, nacelles, and trailing-edge flaps is evident in the pressure plots as  $\beta$  increases through  $12^\circ$

and contributes to increased lateral stability (steeper  $C_l$  and  $C_n$  curve slopes are evident in the interval  $15^\circ \leq \beta \leq 21^\circ$ ). At  $\beta = 18^\circ$ , these components have an even greater effect on the surface flow, and very erratic and unsmooth pressure distributions are seen at  $y/(b/2)_l = 143.39$  in. and  $150.00$  in. The effect of the fuselage on the pressure distributions is seen in figure 46, which shows a dramatic increase in negative  $C_p$  around  $y/(b/2)_l = 0$ .

While the pressure comparisons are generally good for  $\beta = 6^\circ$ ,  $12^\circ$ , and  $18^\circ$ , some of the predicted suction peaks deviate in location or just are not seen in the experimental results. For example, the predicted suction peak at  $y/(b/2)_l = -0.5$  ( $x = 135.13$  in. and  $x = 143.39$  in. shown in fig. 42) appears to be inboard of the experimental peak, which is located at  $y/(b/2)_l = -0.65$ . Another predicted suction peak, which occurs at  $x = 143.39$  in. and  $y/(b/2)_l = -0.70$  at  $\beta = 12^\circ$  (fig. 44), is not verified by the experimental data at all. At  $\beta = 18^\circ$  the numerical results in the region of the wing leading edge did not match well with experiment as shown in the first three MFS's in figure 46. Comparisons at the MBL stations were good, and it is noted that the suction peak that consistently occurred at  $x/c_l = 0.65$  at butline station 42.00 for the entire range of sideslip angles was not computationally predicted.

Additional details of the flow around config3 at various sideslip angles are seen in figures 48–52. All cases were run at  $\alpha = 8^\circ$ . For each sideslip angle, the flow characteristics are first examined by plotting pressure contours on the upper surface as shown in figures 48–50. The flow about the empennage is extracted from the numerical solution at  $x = 200$  in., which bisects the vertical tail at the tip and cuts through the horizontal tail just upstream of its tip. The off-surface  $C_p$  contours and velocity vectors are shown in figures 48 and 51, respectively. To further interpret this empennage flow, streamlines on the left side of the vertical tail and upper aft portion of the fuselage are plotted in figure 52.

Several noteworthy flow characteristics develop as the sideslip angle is increased. The suction pressures on the right side of the wing increase, which is seen in the surface pressure contour plots (figs. 48–50). Examination of the off-surface pressure contours and velocity vectors about the empennage show the increasing effect of the crossflow with increasing sideslip angle. The pressure contours (fig. 51) plotted on the left side of vertical tail for  $\beta = 18^\circ$  reveal a very disorganized pattern of vortical flow, and the velocity vectors (fig. 52) show increased circulation in this area, as well as the formation of additional vortices. This increased circulation contributes to the extensive region of stalled flow. The surface streamlines, shown in figure 53, reveal a highly three-

dimensional flow field characterized by complex vortical flows and extensive separated regions. For all sideslip angles, a primary vortex separates from the sharp leading edge of the vertical tail and reattaches near the trailing edge of the tail. At  $\beta = 12^\circ$ , the flow on vertical tail reveals two saddle points, which develop as a result of the surrounding flow converging to one node or point. Secondary and tertiary separation lines are also evident from this figure. At  $\beta = 18^\circ$ , the flow on the left side of the vertical tail reveals a rather extensive region of stalled flow. The streamlines confirm the existence of the stalled flow and a saddle point (larger than the ones seen at  $\beta = 12^\circ$ ) develops. As the sideslip angle is increased to  $21^\circ$  and beyond, the increased effect of the stalled flow on the tail may contribute to the destabilizing characteristics, which were discussed previously (fig. 37). This type of separated flow appears to contribute to the increase in drag and pitching moment that occurs for the interval of  $15^\circ \leq \beta \leq 21^\circ$ .

## Conclusions

The subsonic flow field about several high-lift (leading-edge flap deflection angle of  $30^\circ$ , trailing-edge flap deflection angle of  $10^\circ$ ) Reference H configurations was successfully predicted using CFL3D, a Reynolds averaged, thin-layer Navier-Stokes flow solver for structured grids. An innovative multiblock strategy was employed at the trailing edge of the wing, which allowed one-to-one matching across the trailing-edge flap block interfaces. Three versions of the Reference H model were simulated, each possessing different components attached to the basic wing-body geometry. The three cases analyzed were the wing-body, wing-body with nacelles and horizontal tail, and wing-body with nacelles and horizontal and vertical tails. The first two configurations modeled the span to the symmetry plane, and solutions were obtained at angle of attack  $6^\circ \leq \alpha \leq 15^\circ$  and zero sideslip. The third configuration modeled the full-span geometry in order to analyze the flow physics and aerodynamic performance at different sideslip angles of  $0^\circ \leq \beta \leq 18^\circ$  at angle of attack  $8^\circ$ . All calculations were performed in free air at wind tunnel conditions of Mach number 0.24 and Reynolds number  $1.4 \times 10^5$  per in. The post-mount model support system used for the test was not computationally simulated. The applicability of the structured Navier-Stokes method is demonstrated by comparing the predicted results with the experimental surface pressures and force and moment data.

The longitudinal performance characteristics were well predicted and very good force and moment comparisons are seen. The pressure distributions show generally good comparisons and trend at the lower angles of attack; however, comparisons diverge when the computational flow on the outboard portion of the wing becomes

extensively separated, which occurs at about  $12^\circ$  angle of attack. Improvements in the solution may be obtained by limiting the Degani-Schiff search to the boundary layer in the Baldwin-Lomax turbulence model as implemented in CFL3D. Agreement may also be improved by specifying the experimentally determined transition location from laminar flow to turbulent flow. Not knowing this information would affect the computational results since transition determines the onset of separation and drag.

Postprocessing of the numerical solutions provided detailed surface and off-surface flow quantities not obtained in the wind tunnel. The plotted off-surface pressure contours of the computational vortical flow field were very useful in interpreting the wind tunnel data and provided a comprehensive three-dimensional understanding of the flow. As is evident from the plotted off-surface flow contours, a very complex multiple vortical system develops at the higher angles of attack ( $\alpha \geq 12^\circ$ ). Also, at the higher angles of attack, the flow on the inboard wing turns spanwise onto the outboard panel. This spanwise effect further complicates the highly vortical flow since it impacts the boundary layer and causes extensive separation on the outboard section of the wing.

The lateral performance characteristics showed fairly good quantitative comparisons, and the overall predicted trends in the yawing moment, rolling moment, and pitching moment were well predicted. The computational surface pressures that are extracted at constant spanwise stations reveal asymmetric pressure distributions characterized by higher suction peaks on the right wing compared to the left wing. The side force on the vertical tail at the lower yaw angles produces a stabilizing effect. However at the higher sideslip angles, an extensive area of stalled flow forms on the left side of the vertical tail

and contributes to the destabilizing characteristics of the model.

The high-lift high speed civil transport work is ongoing in support of the High Speed Research program, and future work will be extended to updated configurations in the downselect process. Because of the complexity of the multiblock gridding, as well as the total number of grid points required to adequately resolve the high-lift flow, this method would not be considered for design. However, it does well as an analysis tool and future improvements in the CFL3D code should be made to broaden its application to include more accurate simulation of multiple vortical flows and boundary layer separation.

NASA Langley Research Center  
Hampton, VA 23681-2199  
March 17, 1998

## References

1. Gentry, G., Jr.; Quinto, P.; Gatlin, G.; and Applin, Z.: *The Langley 14- by 22-Foot Subsonic Tunnel: Description, Flow Characteristics, and Guide for Users*. NASA TP-3008, 1990.
2. Thomas, J.; Krist, S.; and Anderson, W.: Navier-Stokes Computations of Vortical Flows Over Low Aspect Ratio Wings. *AIAA J.*, vol. 28, no. 2, 1990, pp. 205-212.
3. Biedron, R. T.; and Thomas, J. L.: A Generalized Patched-Grid Algorithm With Application to the F-18 Forebody With Actuated Control Strake. *Comput. Sys. Eng.*, vol. 1, nos. 2-4, 1990, pp. 563-576.
4. Abdol-Hamid, Khaled S.; Carlson, John R.; and Pao, S. Paul: Calculations of Turbulent Flows Using Mesh Sequencing and Conservative Patch Algorithms. AIAA-95-2336, July 1995.

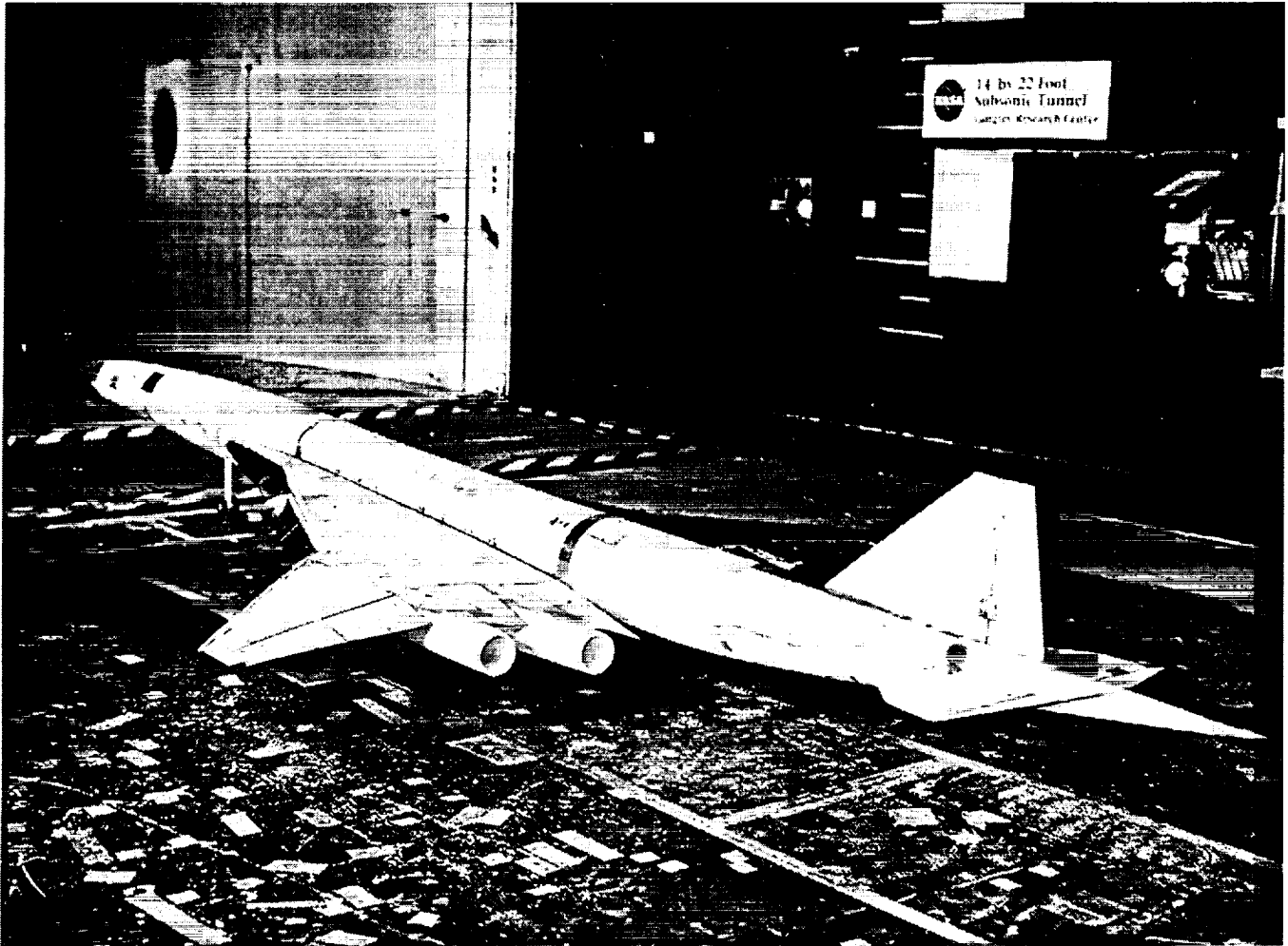


Figure 1. Boeing 0.06-scale Reference H model with deployed leading- and trailing-edge flaps in Langley 14- by 22-Foot Subsonic Tunnel.

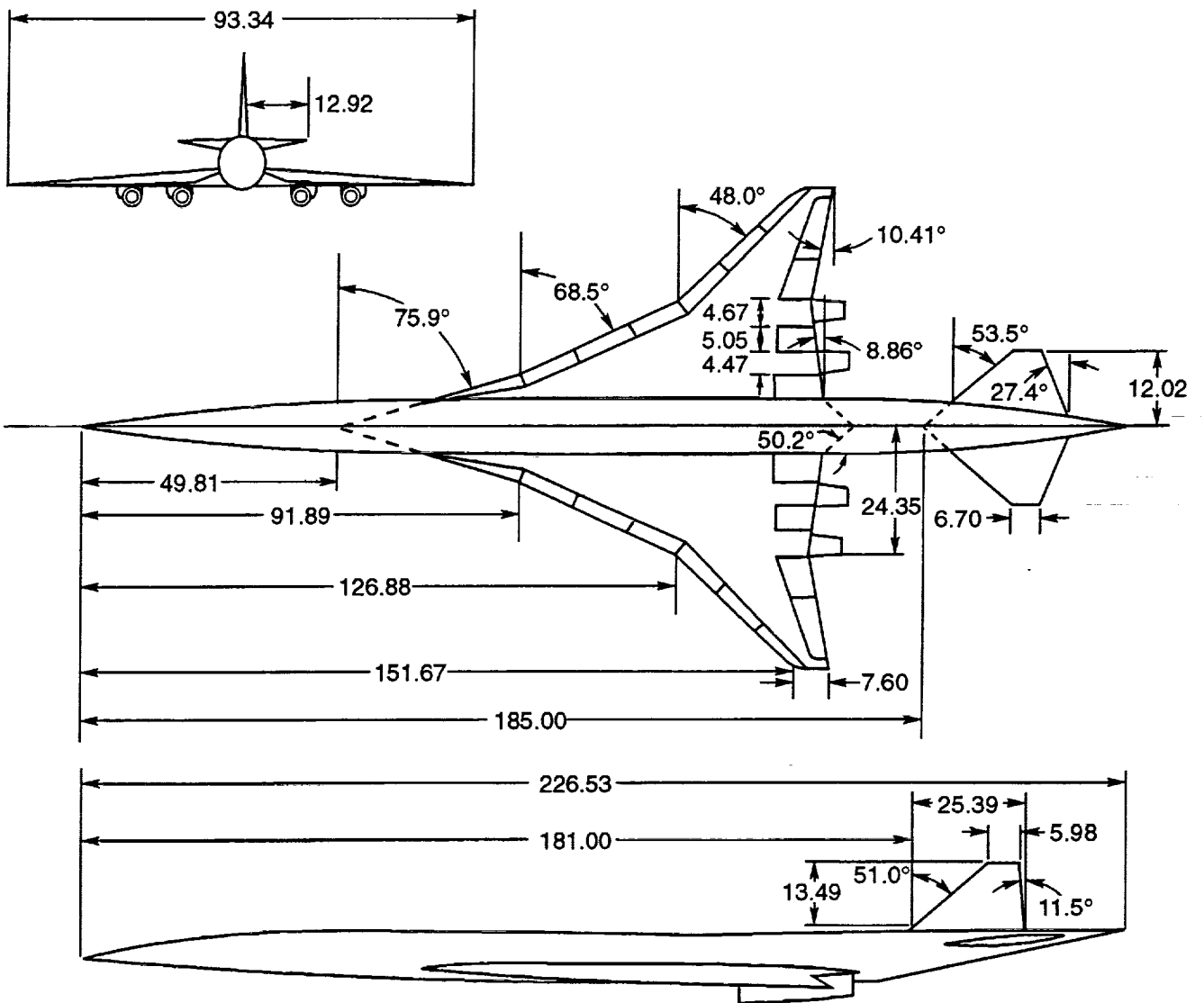


Figure 2. Three-view sketch of 0.06-scale Reference H model. Dimensions are in inches.

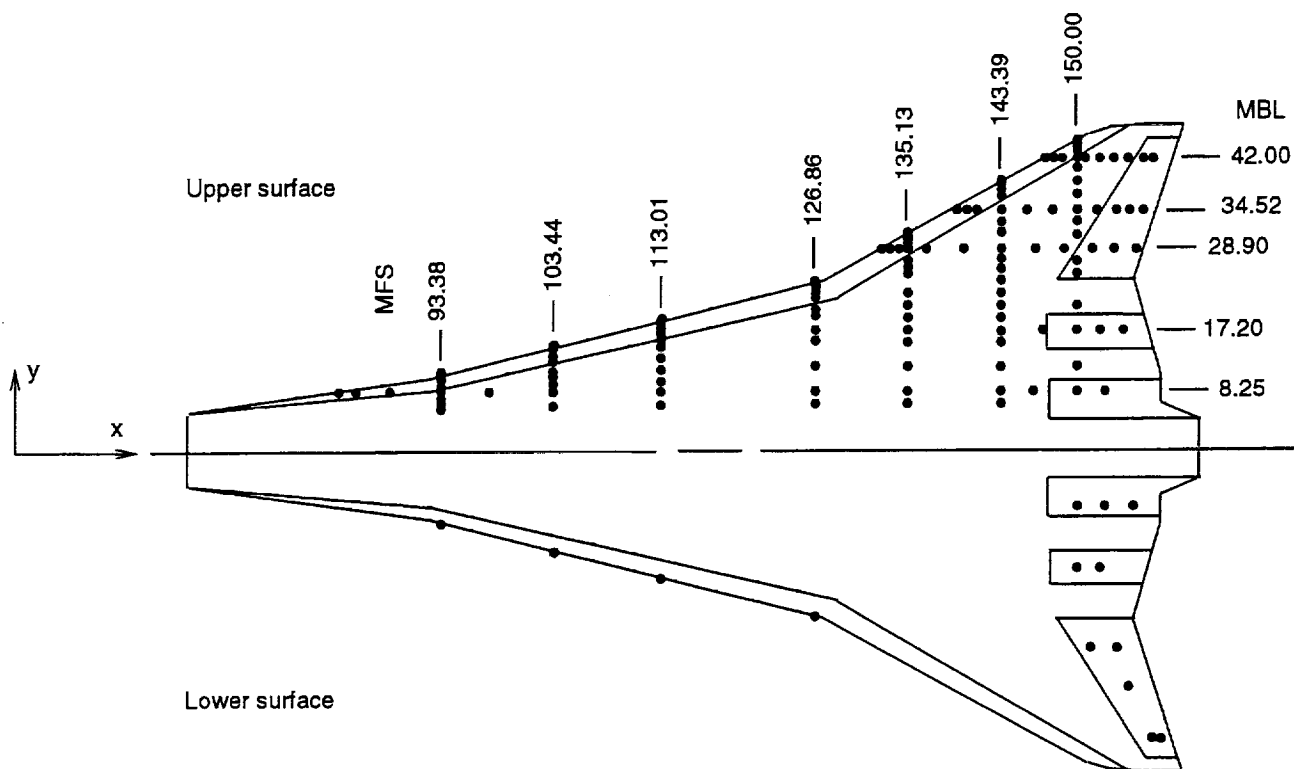


Figure 3. Schematic representation of upper and lower surface pressure port locations for 0.06-scale Reference H model. All pressure ports were located on left wing (below centerline) on model.

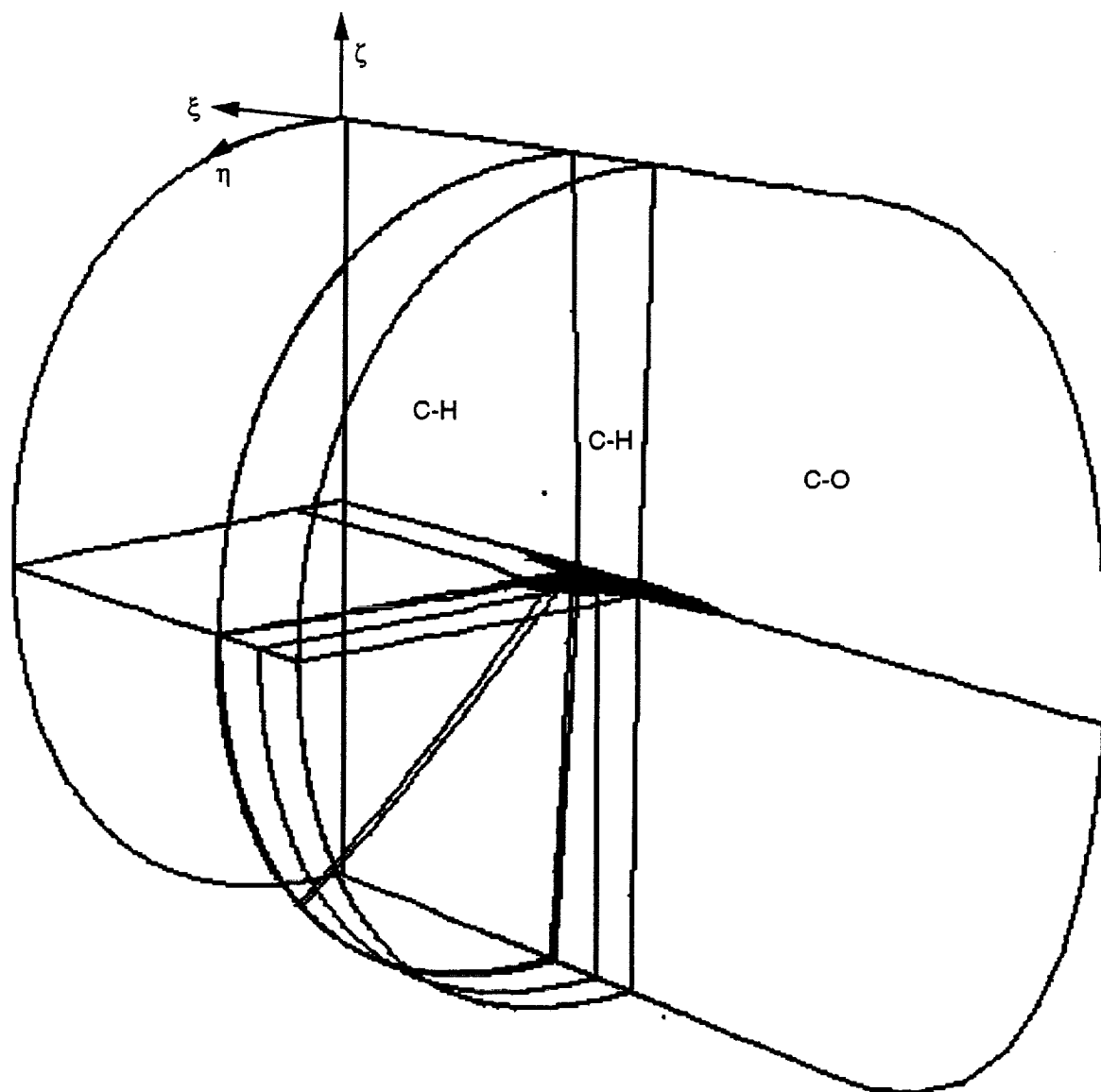


Figure 4. Far-field grid blocking arrangement for Reference H config2 geometry.



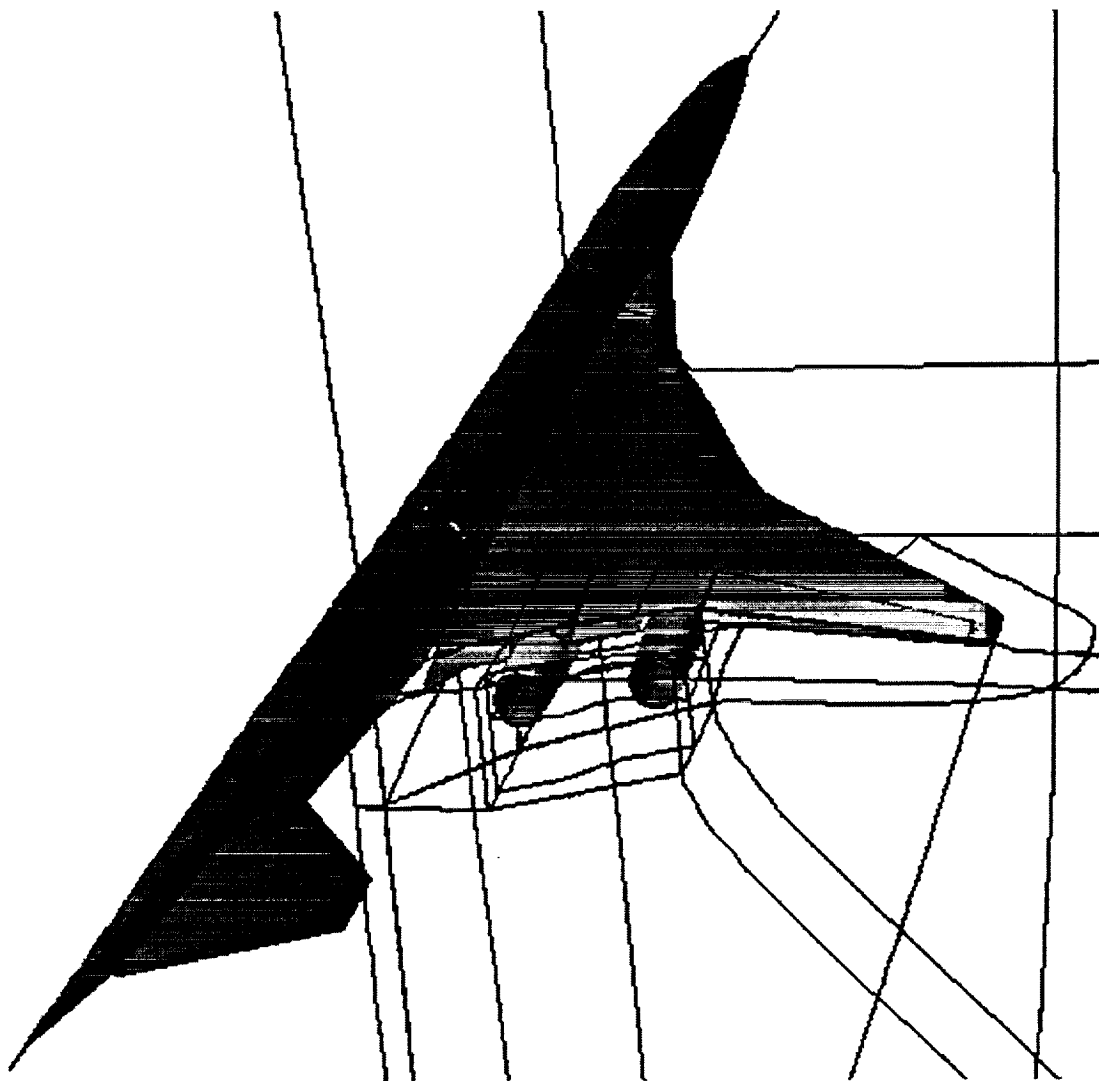


Figure 5. Near-field grid blocking structure for Reference H config2 geometry.

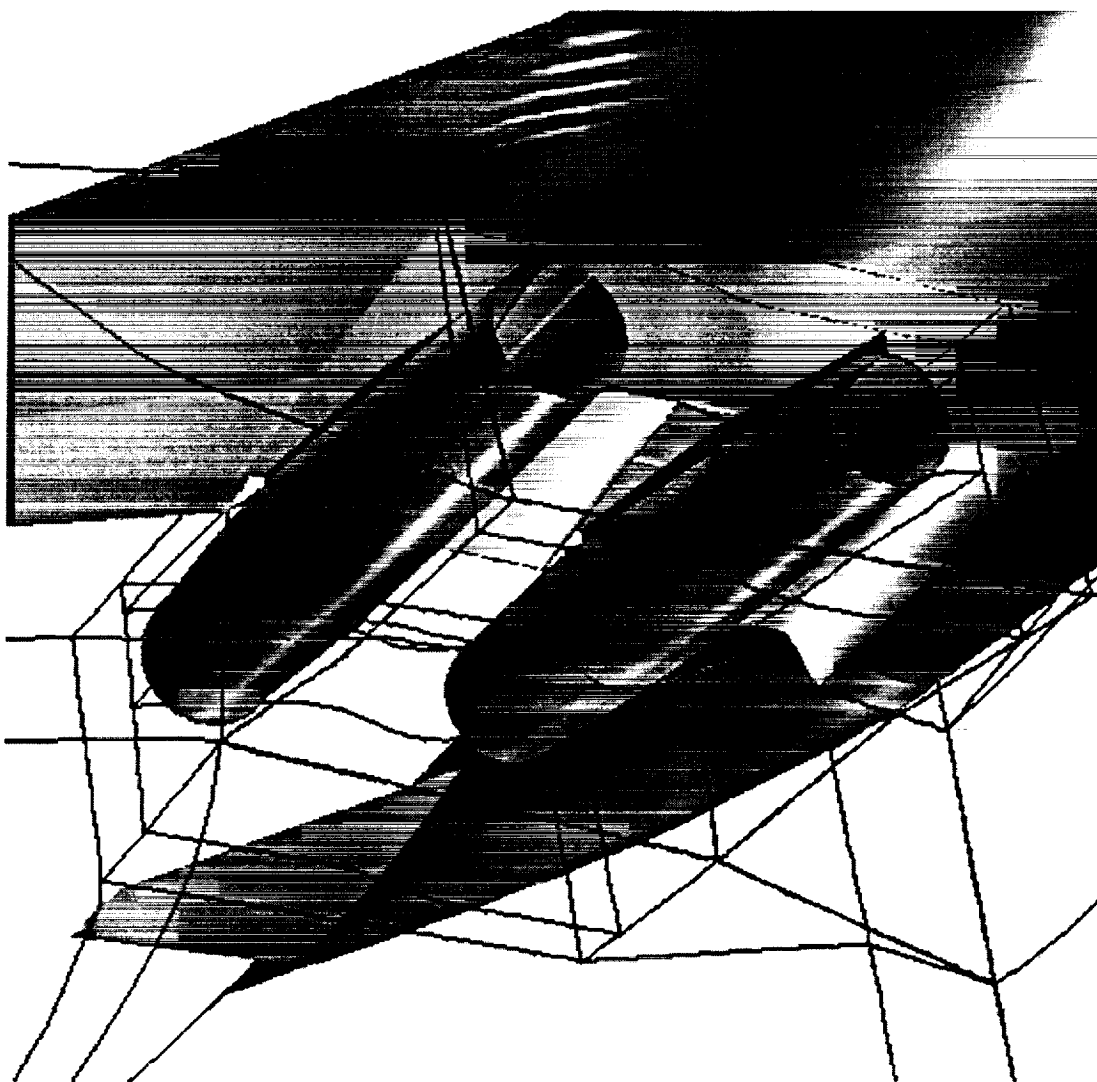


Figure 6. Close-up view of multiblock arrangement around nacelles.

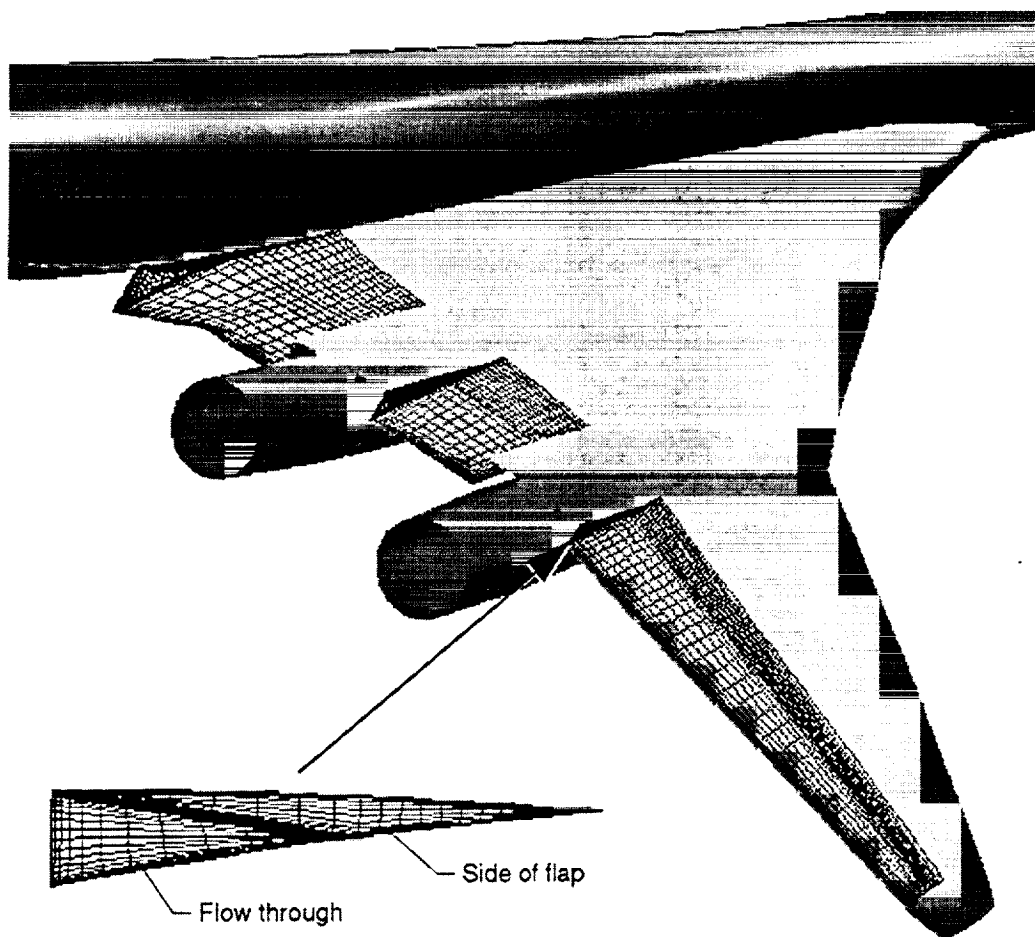


Figure 7. Trailing-edge flap grid blocking strategy for Reference H configuration.

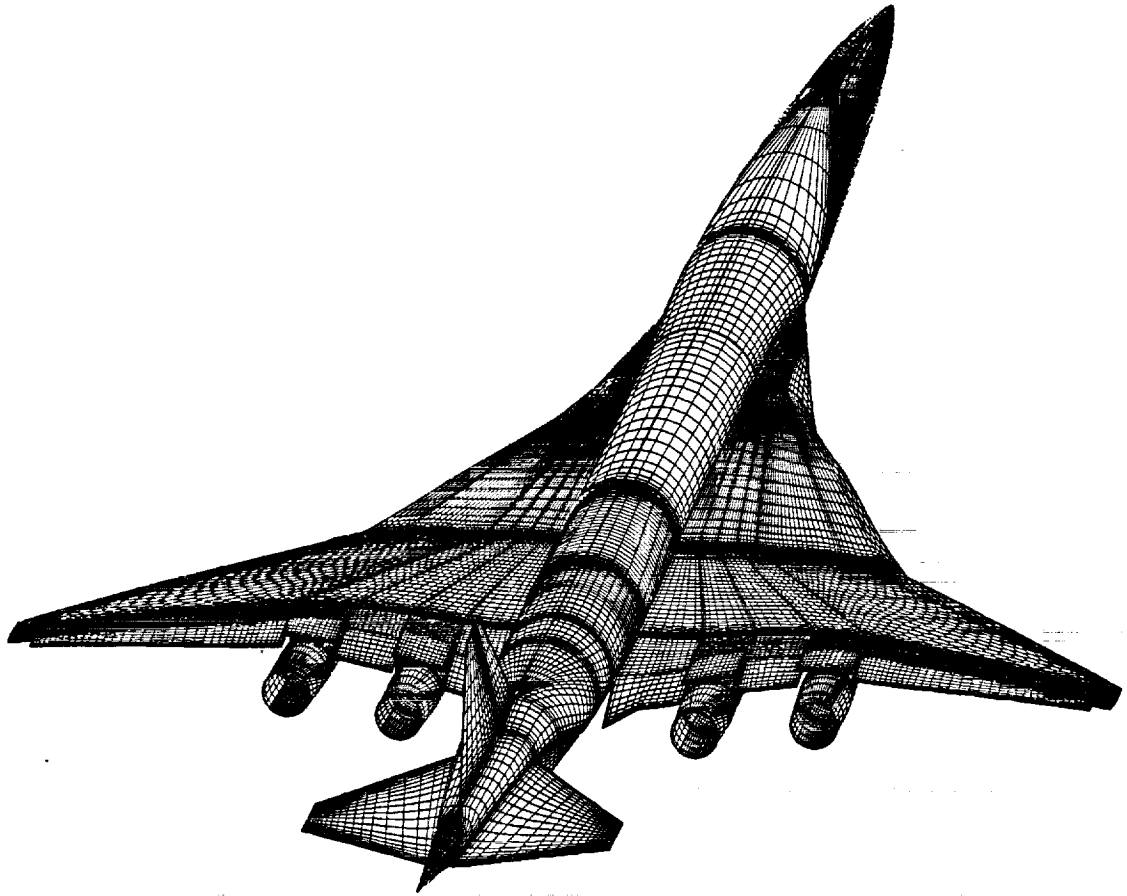


Figure 8. Surface grid for Reference H full-span configuration, config3.

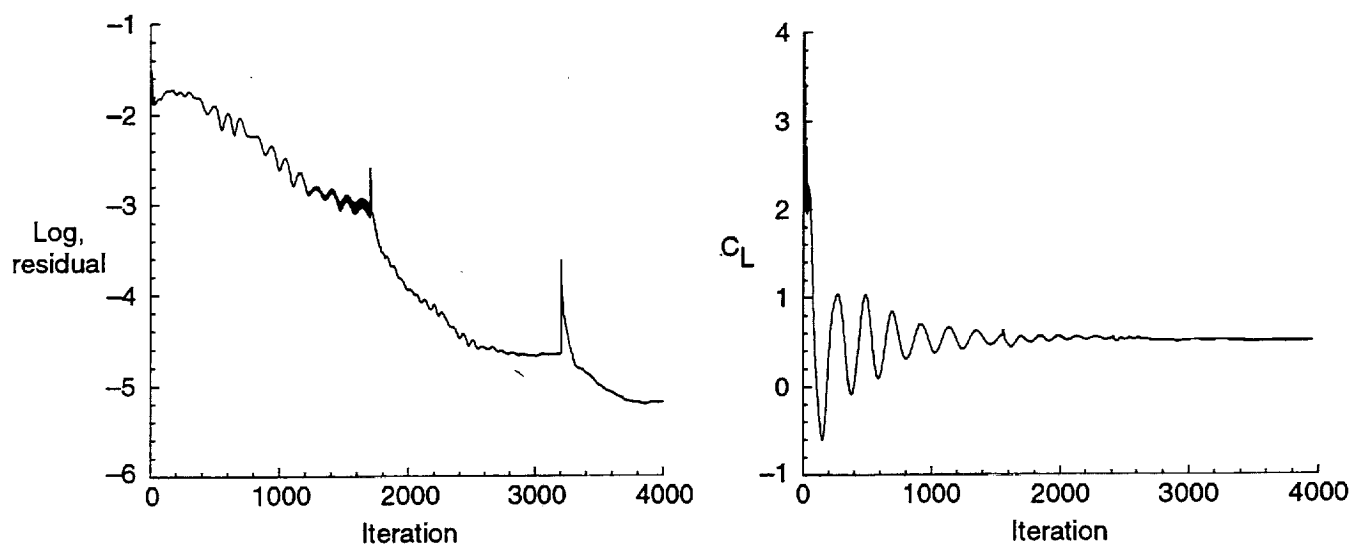


Figure 9. Convergence characteristics for Reference H config2 at  $\alpha = 10^\circ$  and  $\beta = 0^\circ$ .

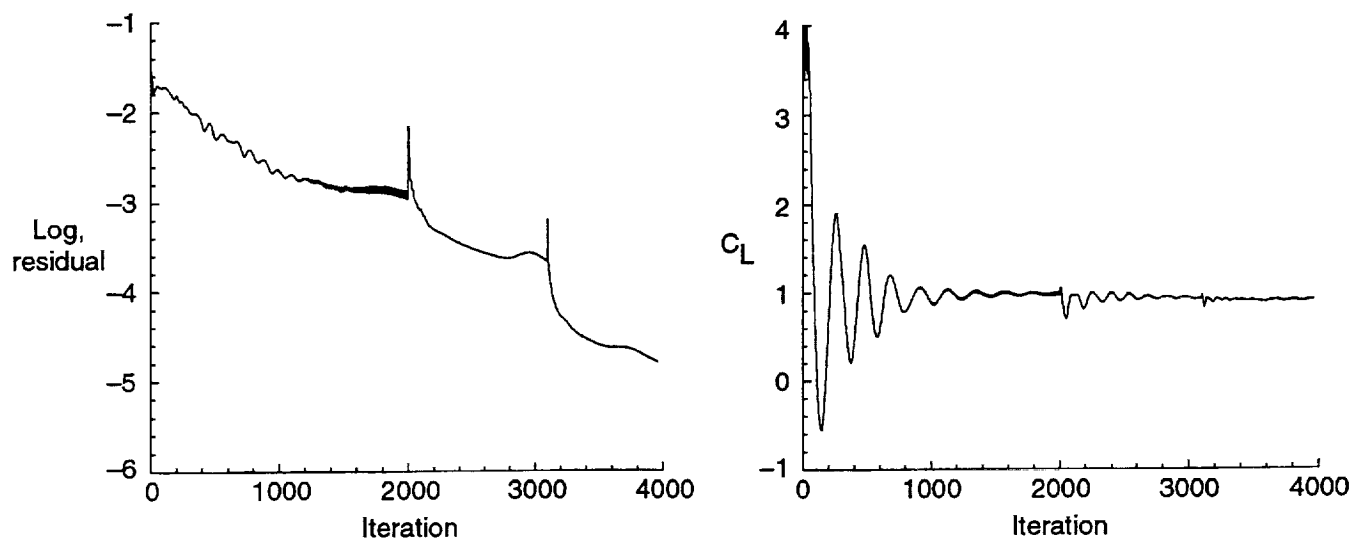


Figure 10. Convergence characteristics for Reference H config3 at  $\alpha = 8^\circ$  and  $\beta = 6^\circ$ .

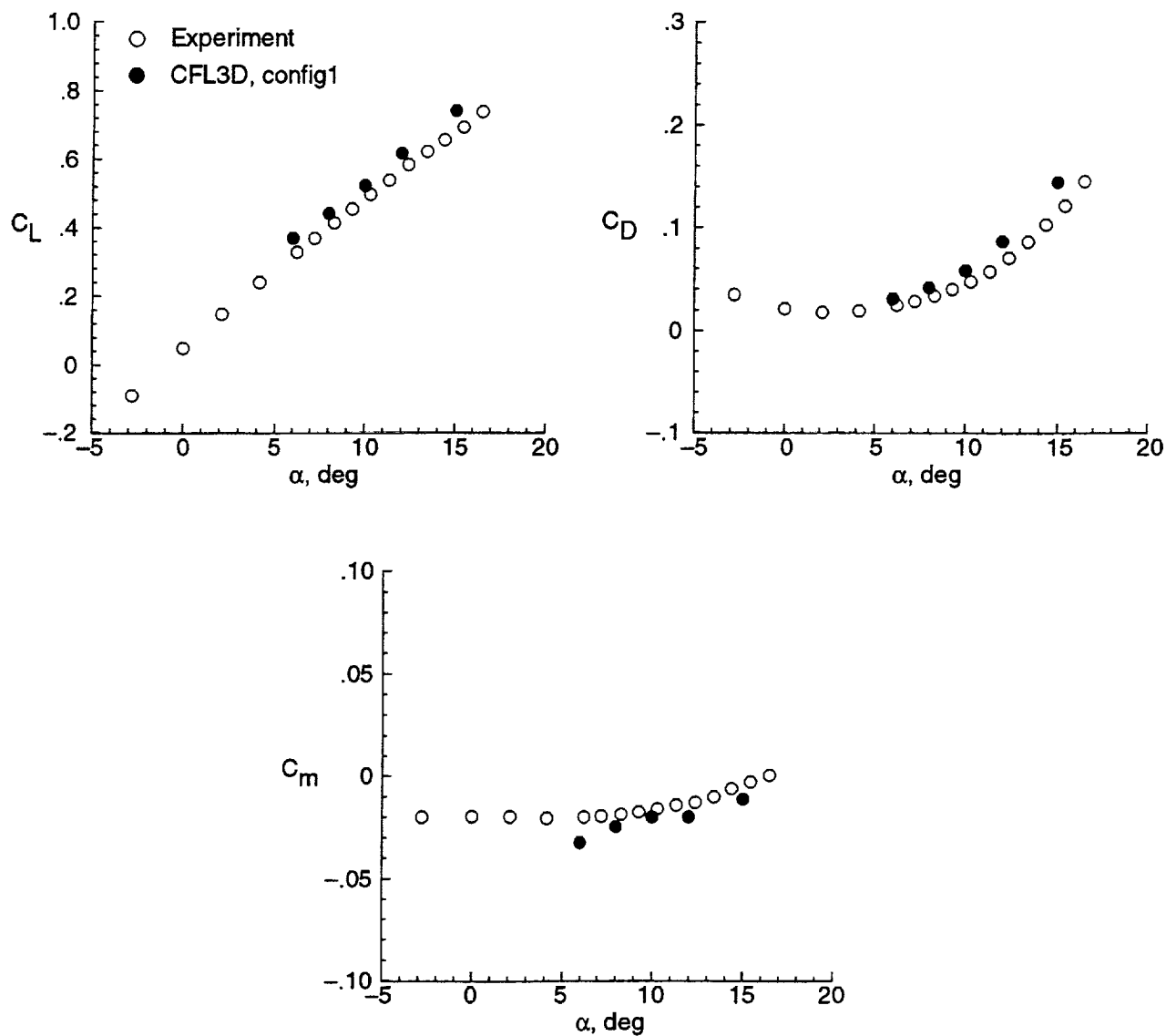


Figure 11. Force and moment comparisons for Reference H config1 at  $6^\circ \leq \alpha \leq 15^\circ$  and  $\beta = 0^\circ$ .

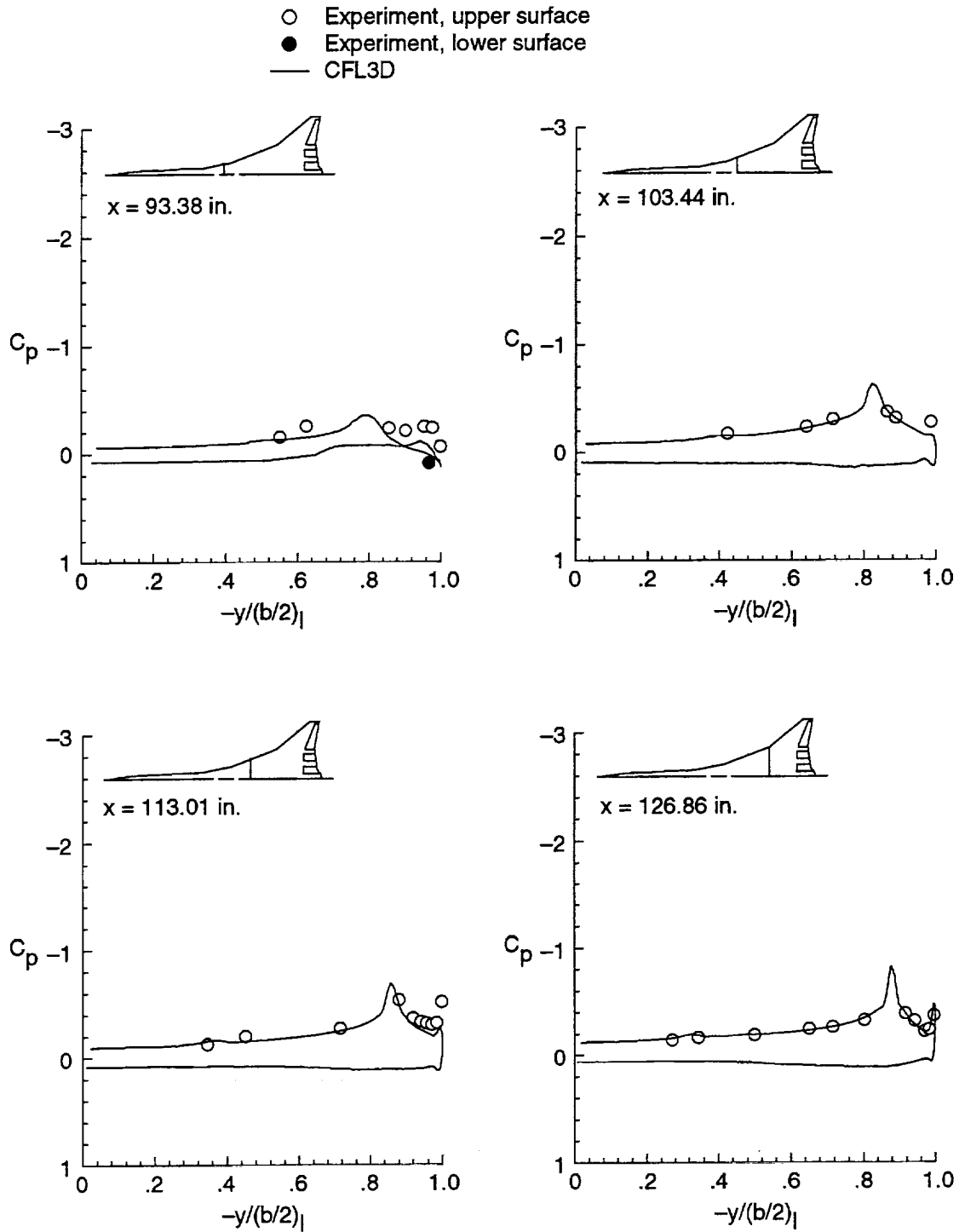


Figure 12. Spanwise distributions of experimental and computational  $C_p$  for Reference H config1 at  $M = 0.24$  and  $\alpha = 6^\circ$ .

○ Experiment, upper surface  
 — CFL3D

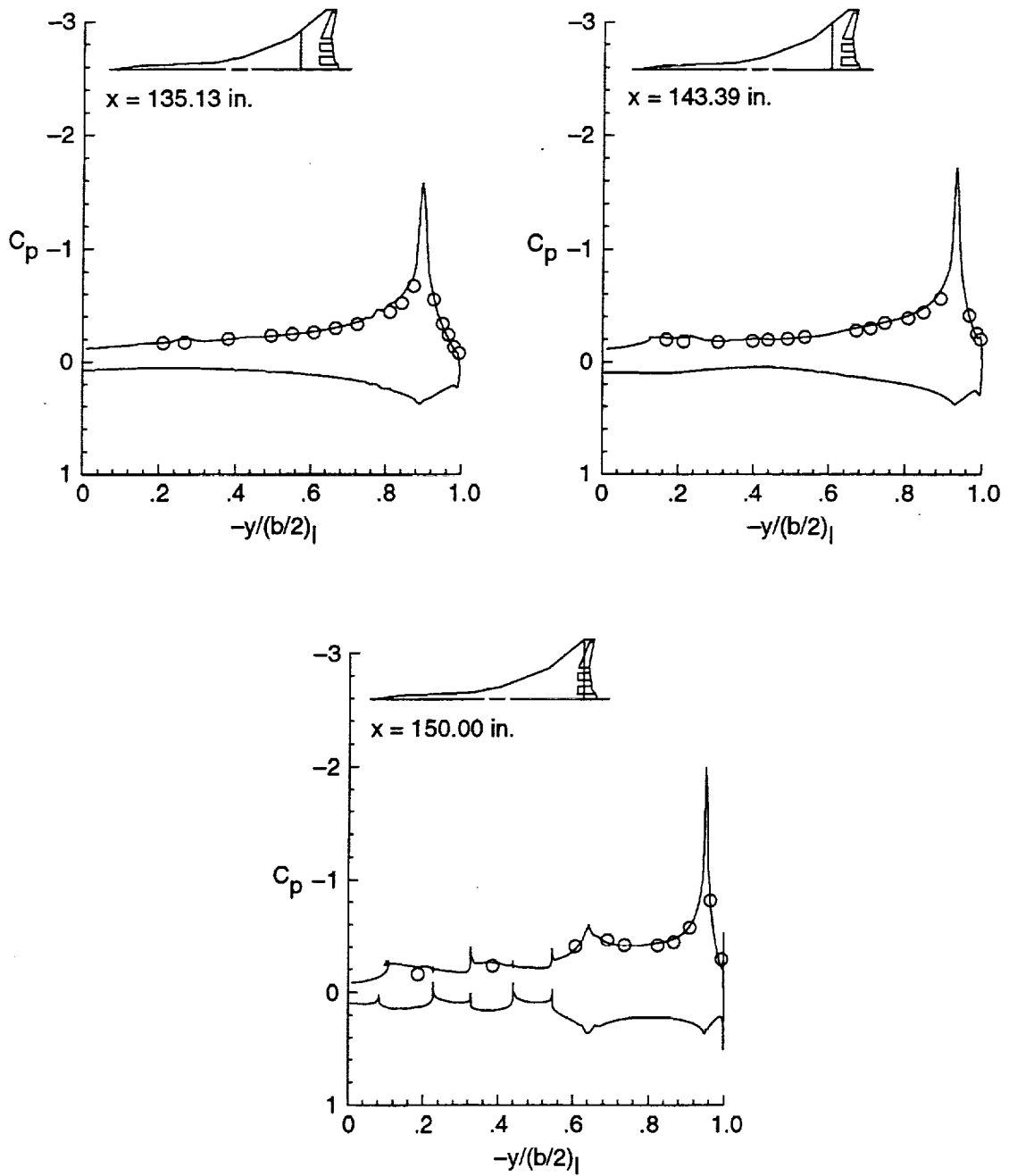


Figure 12. Concluded.



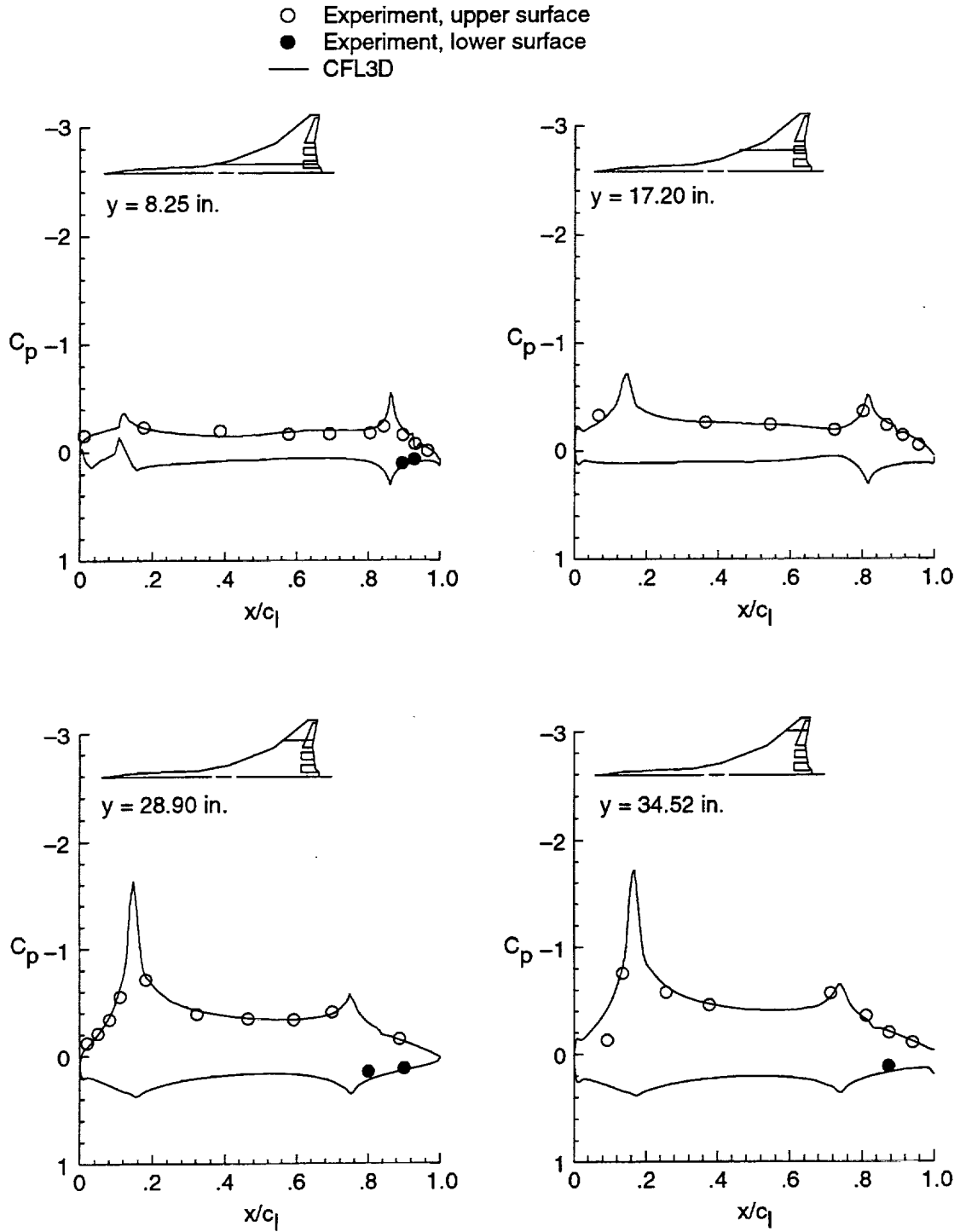


Figure 13. Streamwise distributions of experimental and computational  $C_p$  for Reference H config1 at  $M = 0.24$  and  $\alpha = 6^\circ$ .

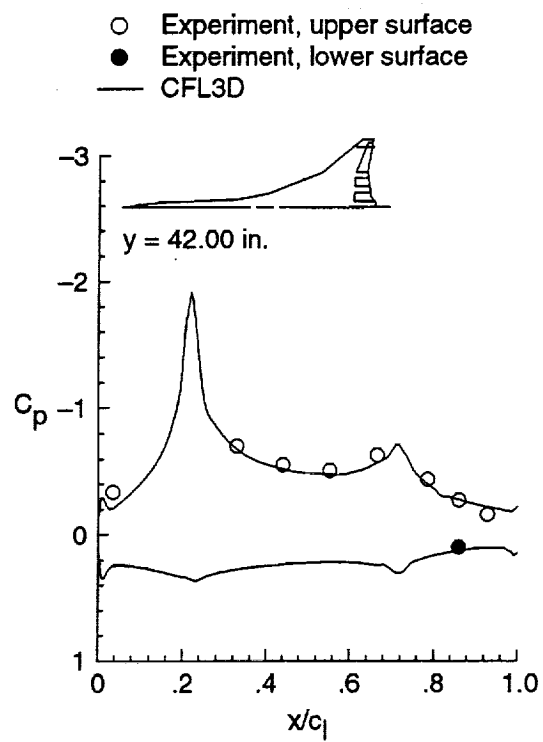


Figure 13. Concluded.

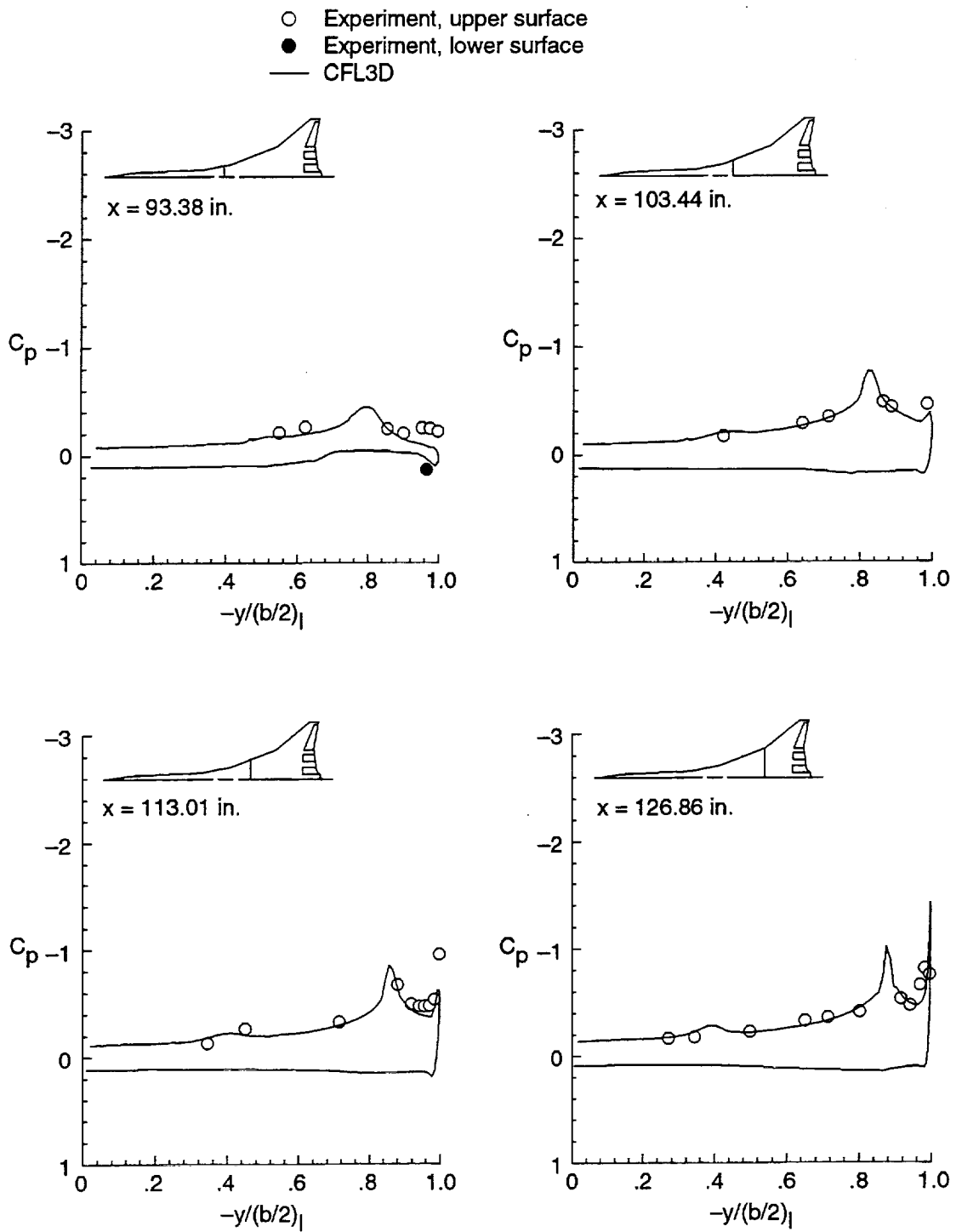


Figure 14. Spanwise distributions of experimental and computational  $C_p$  for Reference H config1 at  $M = 0.24$  and  $\alpha = 8^\circ$ .

○ Experiment, upper surface  
 — CFL3D

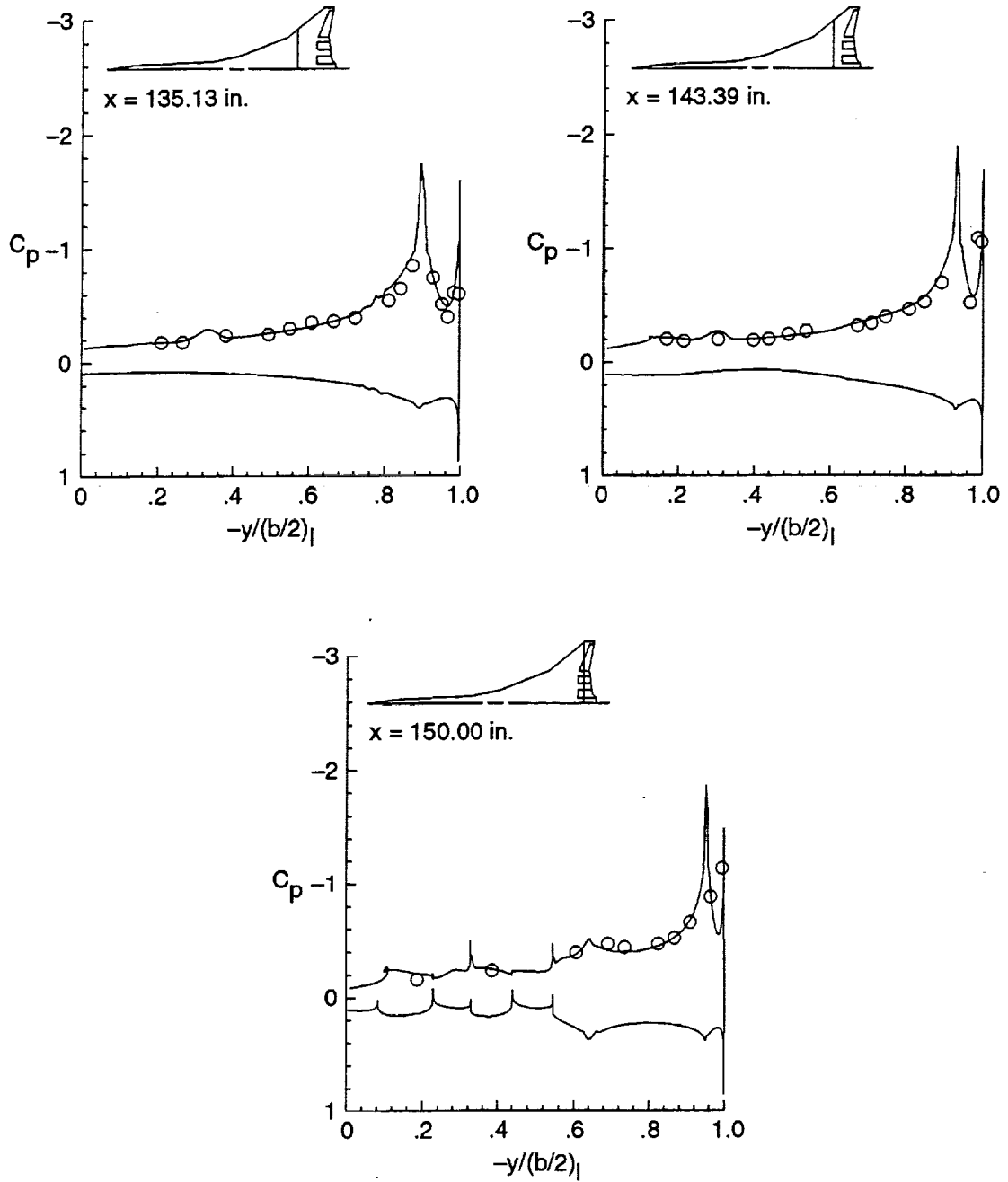


Figure 14. Concluded.

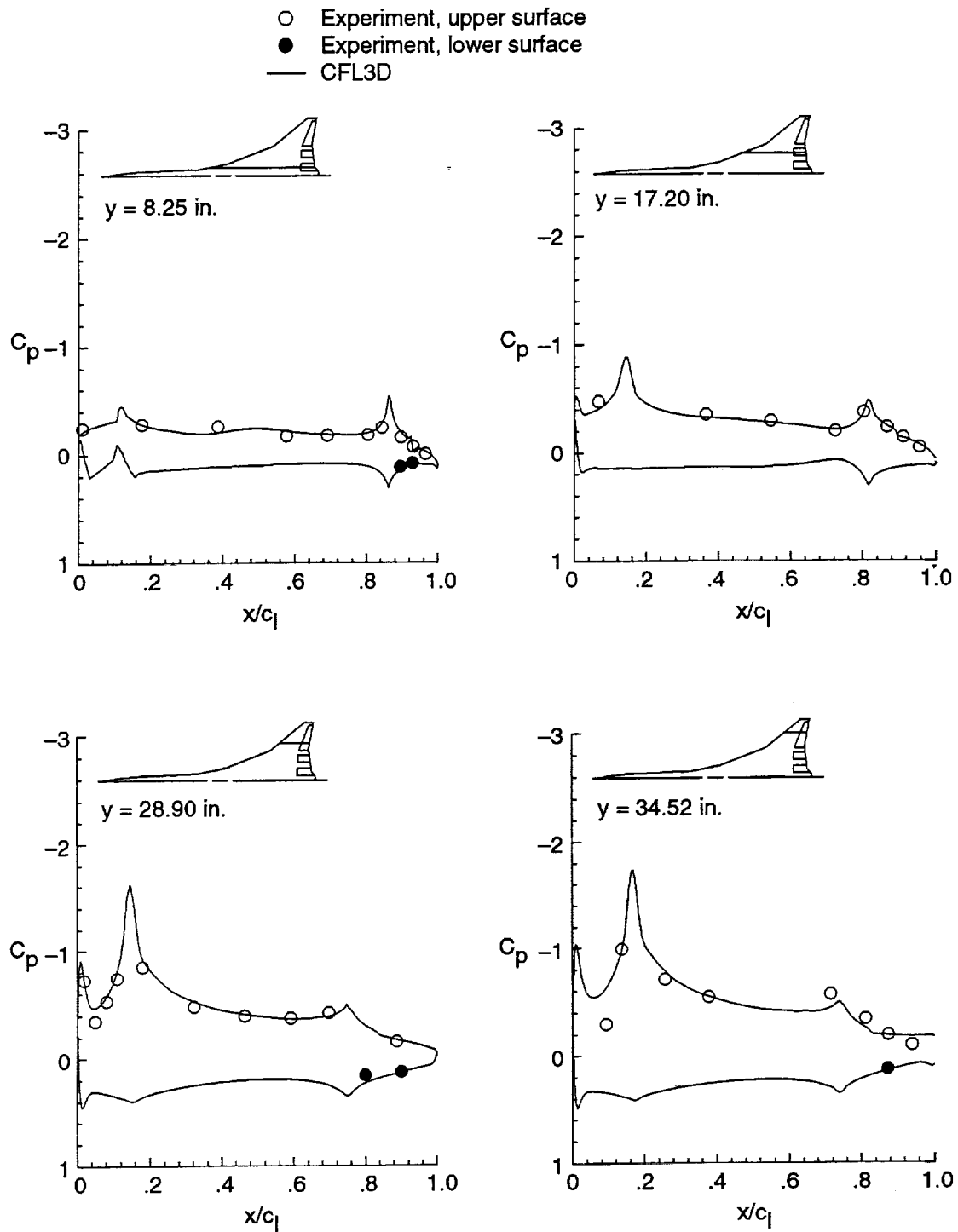


Figure 15. Streamwise distributions of experimental and computational  $C_p$  for Reference H config1 at  $M = 0.24$  and  $\alpha = 8^\circ$ .

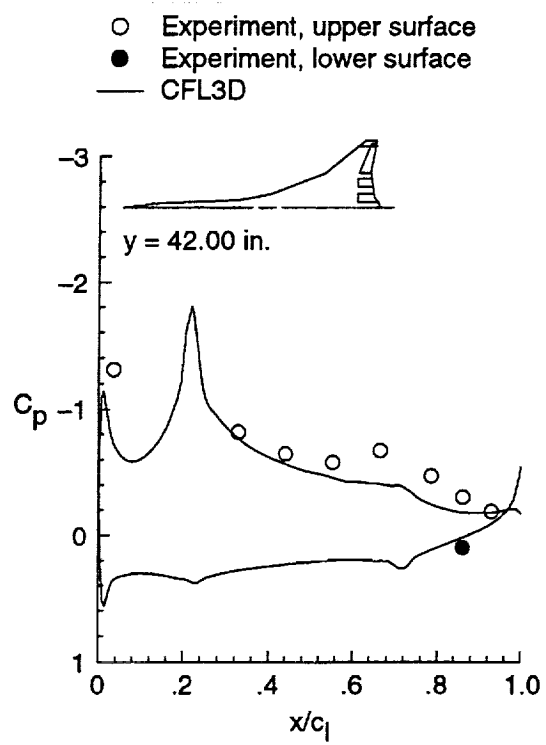


Figure 15. Concluded.

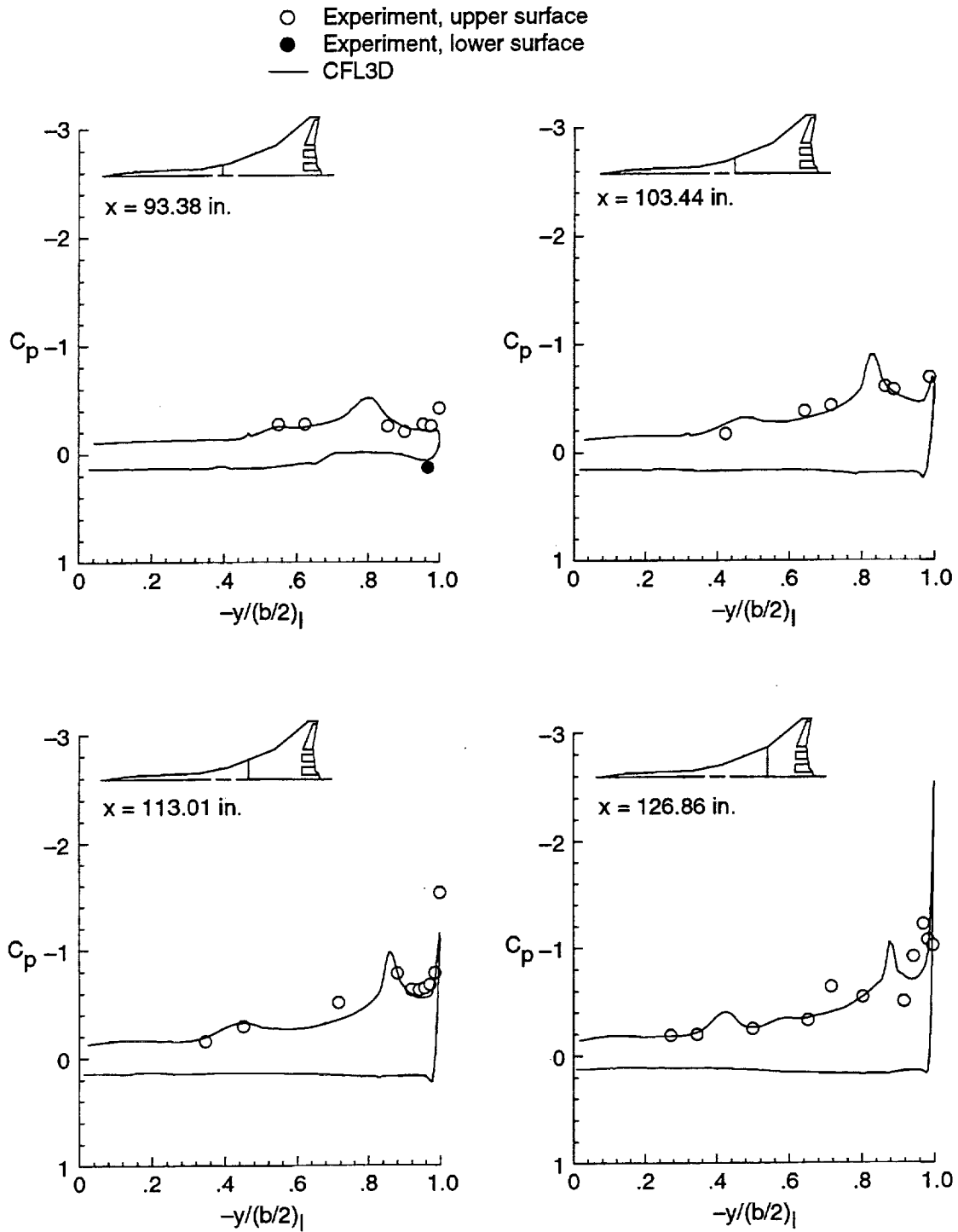


Figure 16. Spanwise distributions of experimental and computational  $C_p$  for Reference H config1 at  $M = 0.24$  and  $\alpha = 10^\circ$ .

○ Experiment, upper surface  
 — CFL3D

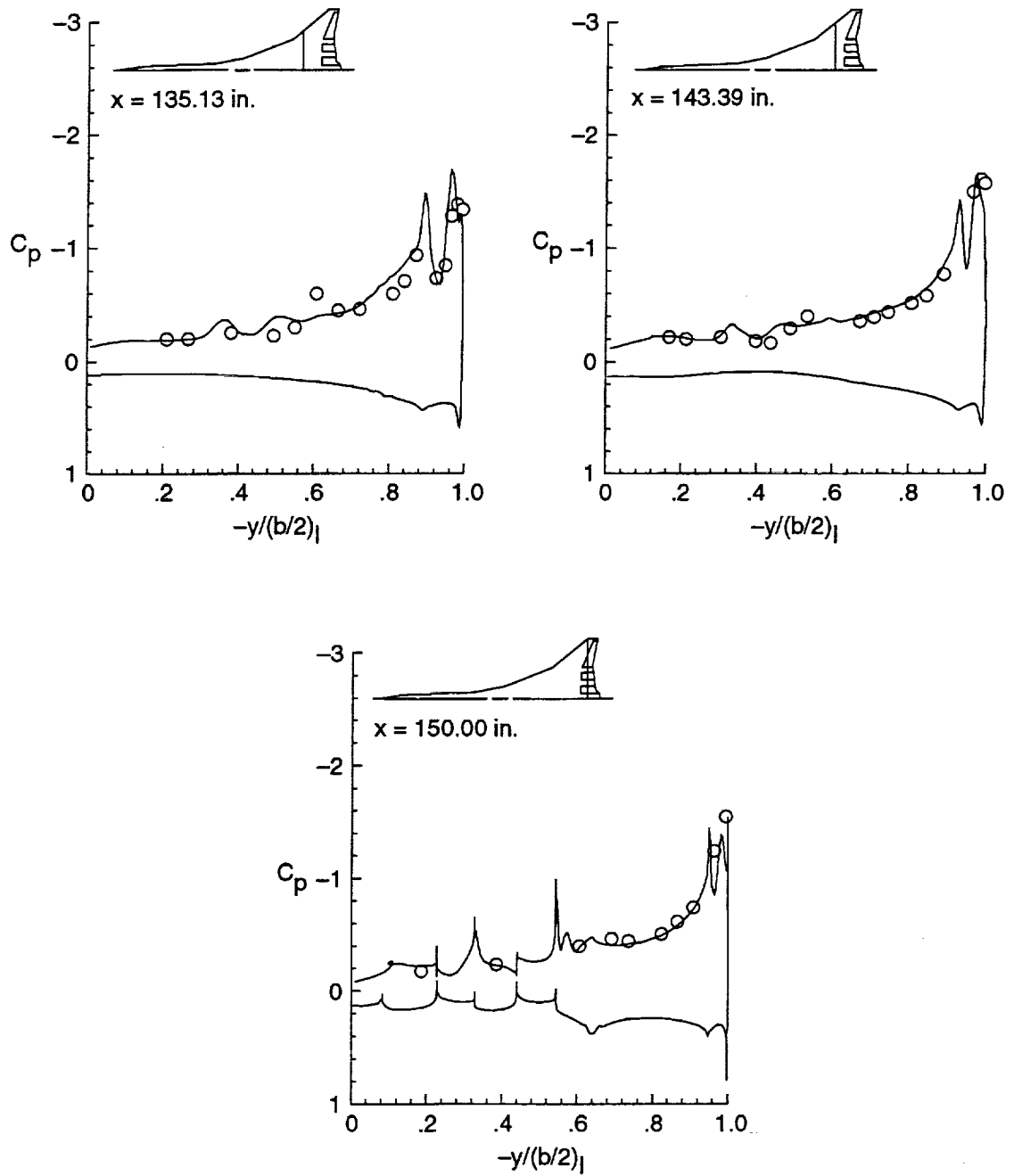


Figure 16. Concluded.



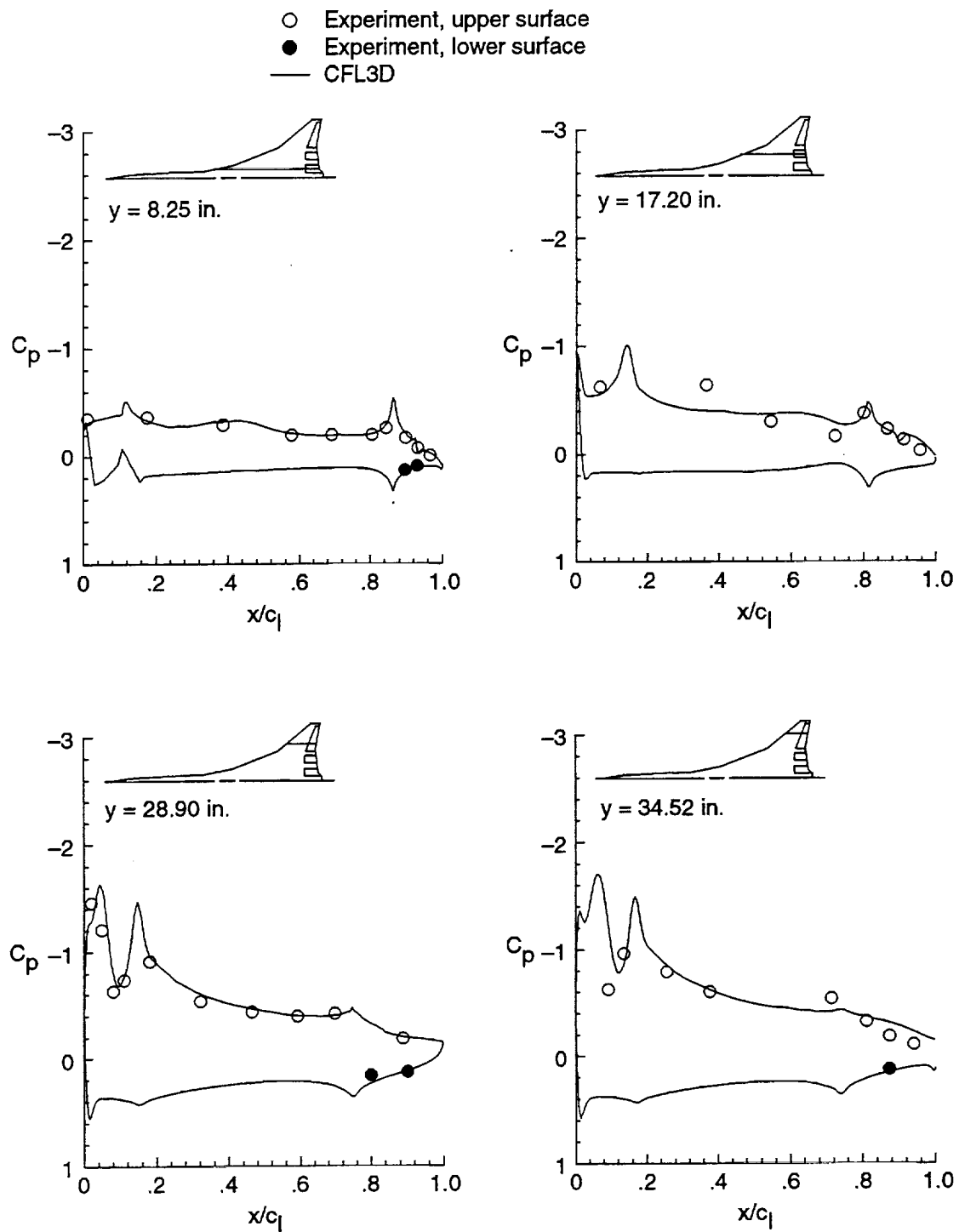


Figure 17. Streamwise distributions of experimental and computational  $C_p$  for Reference H config1 at  $M = 0.24$  and  $\alpha = 10^\circ$ .

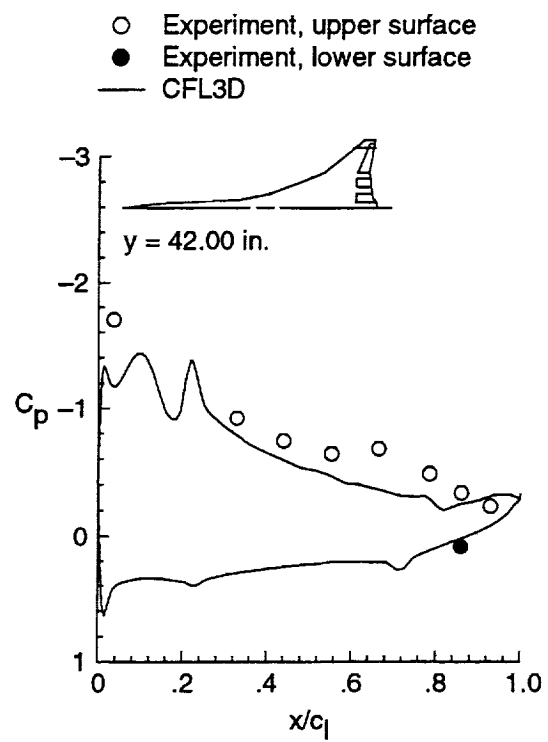


Figure 17. Concluded.

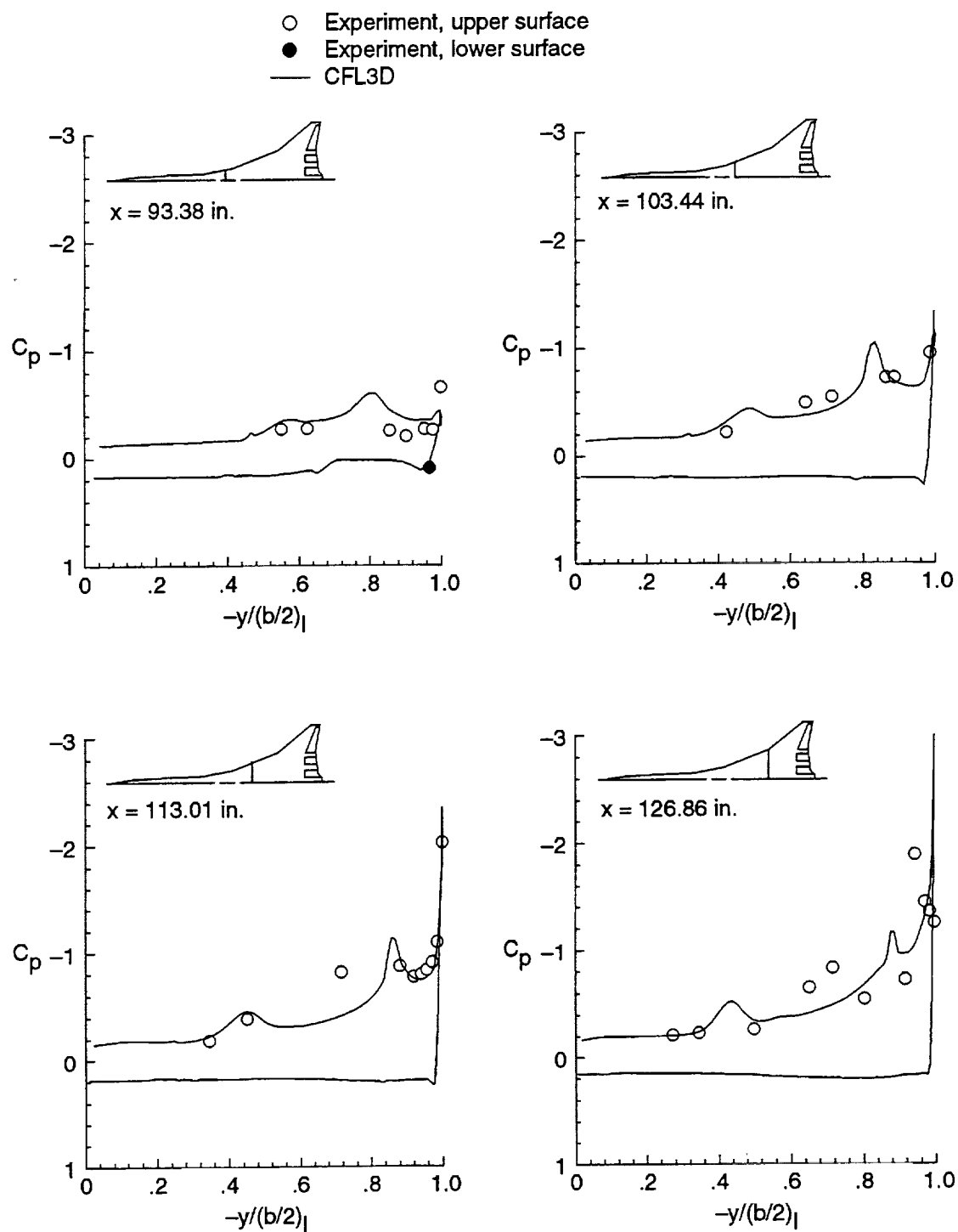


Figure 18. Spanwise distributions of experimental and computational  $C_p$  for Reference H config1 at  $M = 0.24$  and  $\alpha = 12^\circ$ .

○ Experiment, upper surface  
 — CFL3D

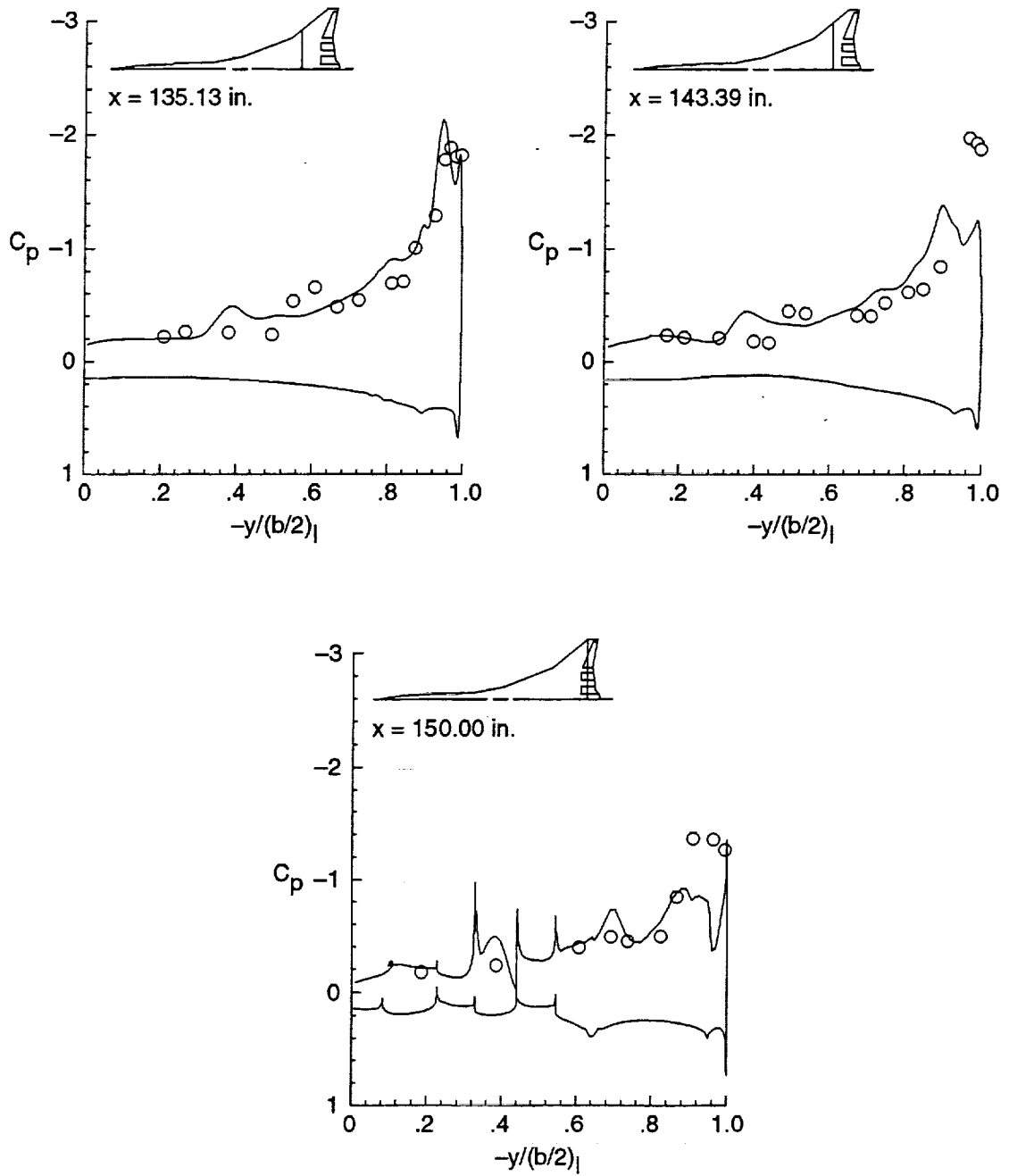


Figure 18. Concluded.

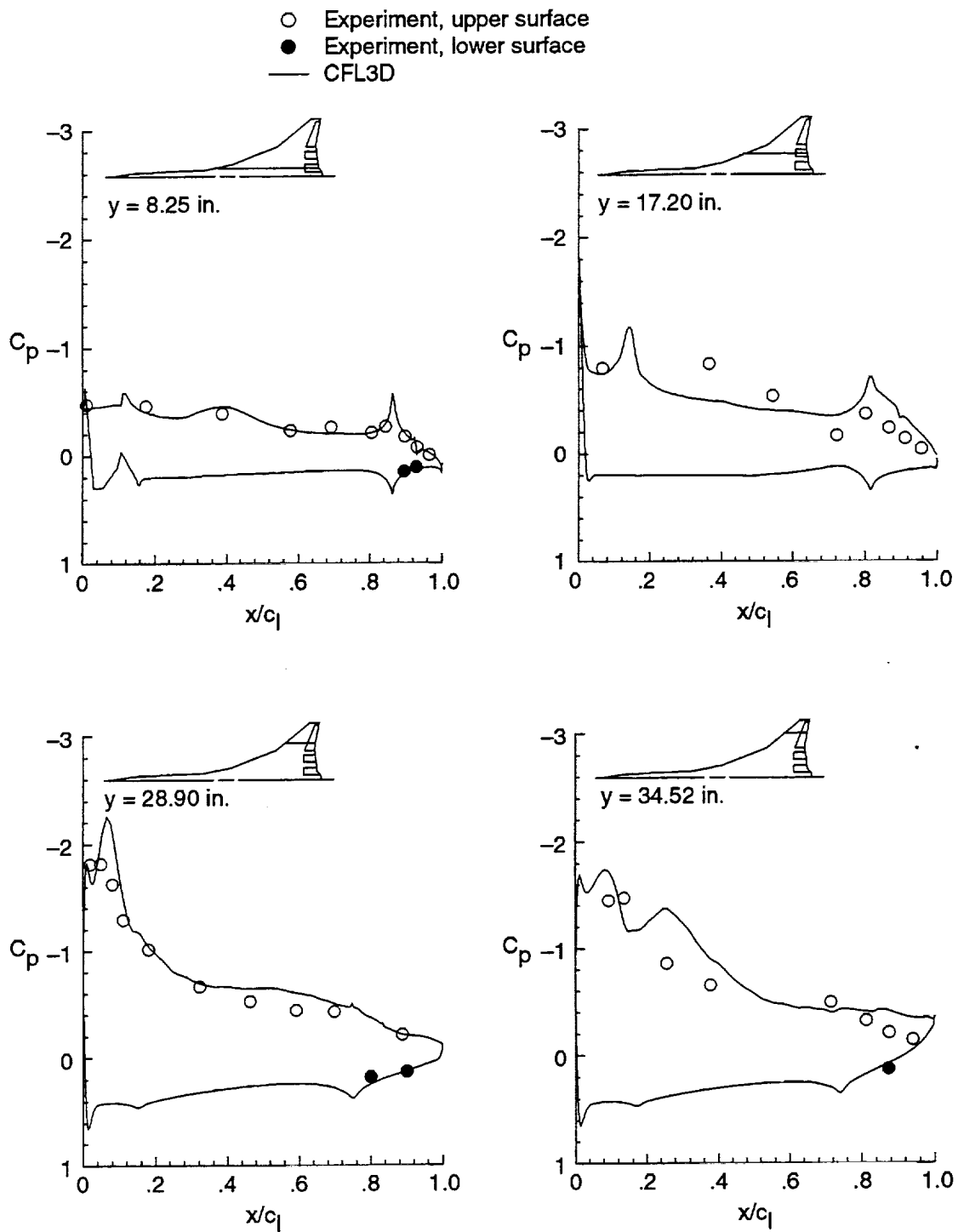


Figure 19. Streamwise distributions of experimental and computational  $C_p$  for Reference H config1 at  $M = 0.24$  and  $\alpha = 12^\circ$ .

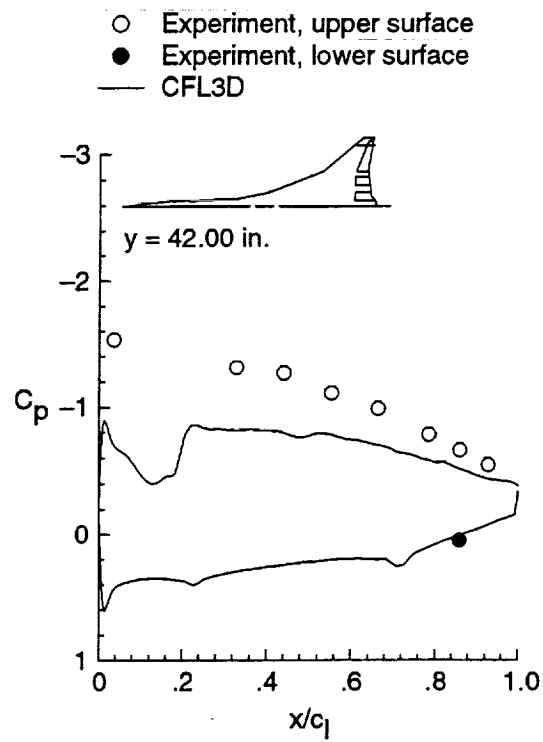


Figure 19. Concluded.

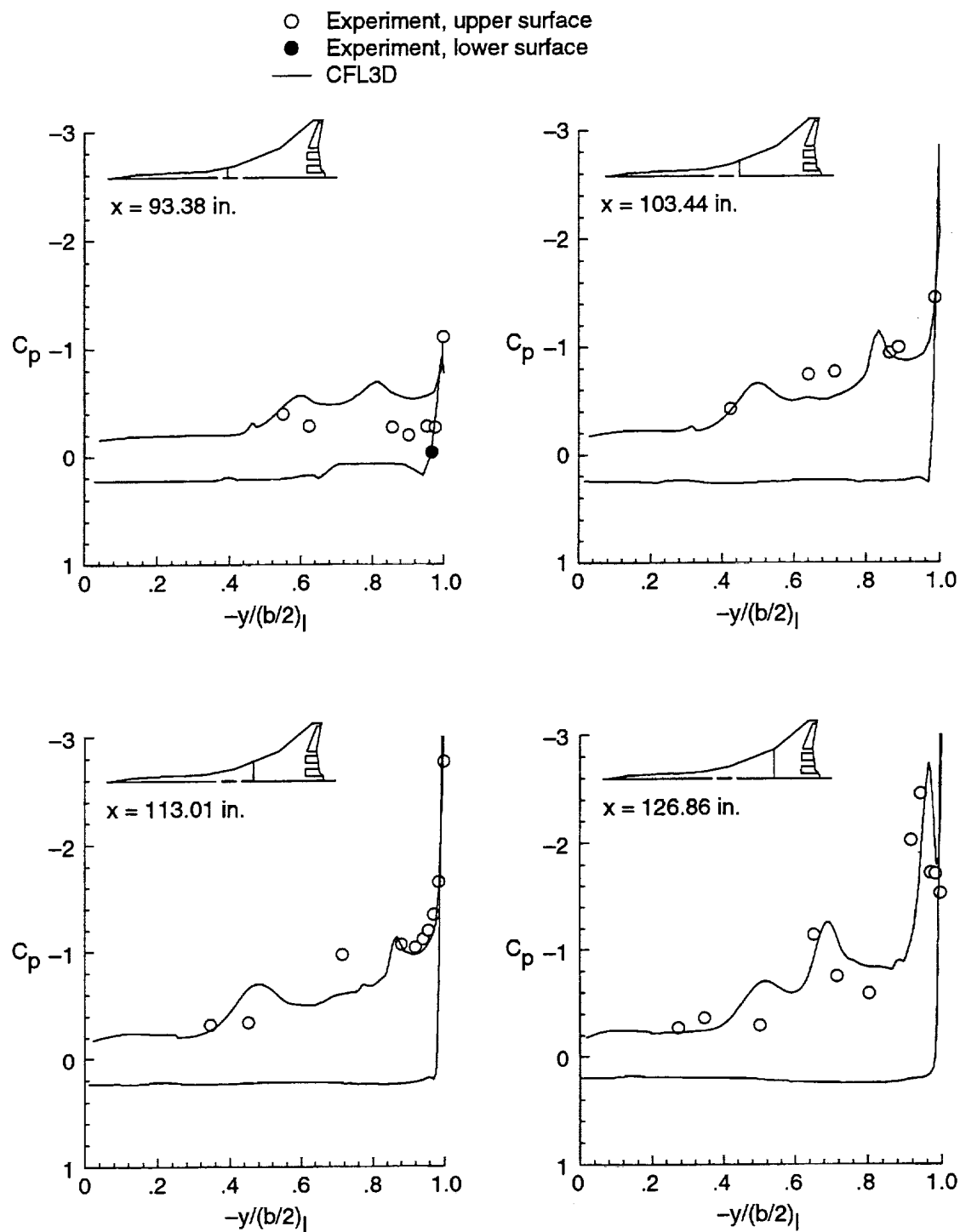


Figure 20. Spanwise distributions of experimental and computational  $C_p$  for Reference H config1 at  $M = 0.24$  and  $\alpha = 15^\circ$ .

○ Experiment, upper surface  
 — CFL3D

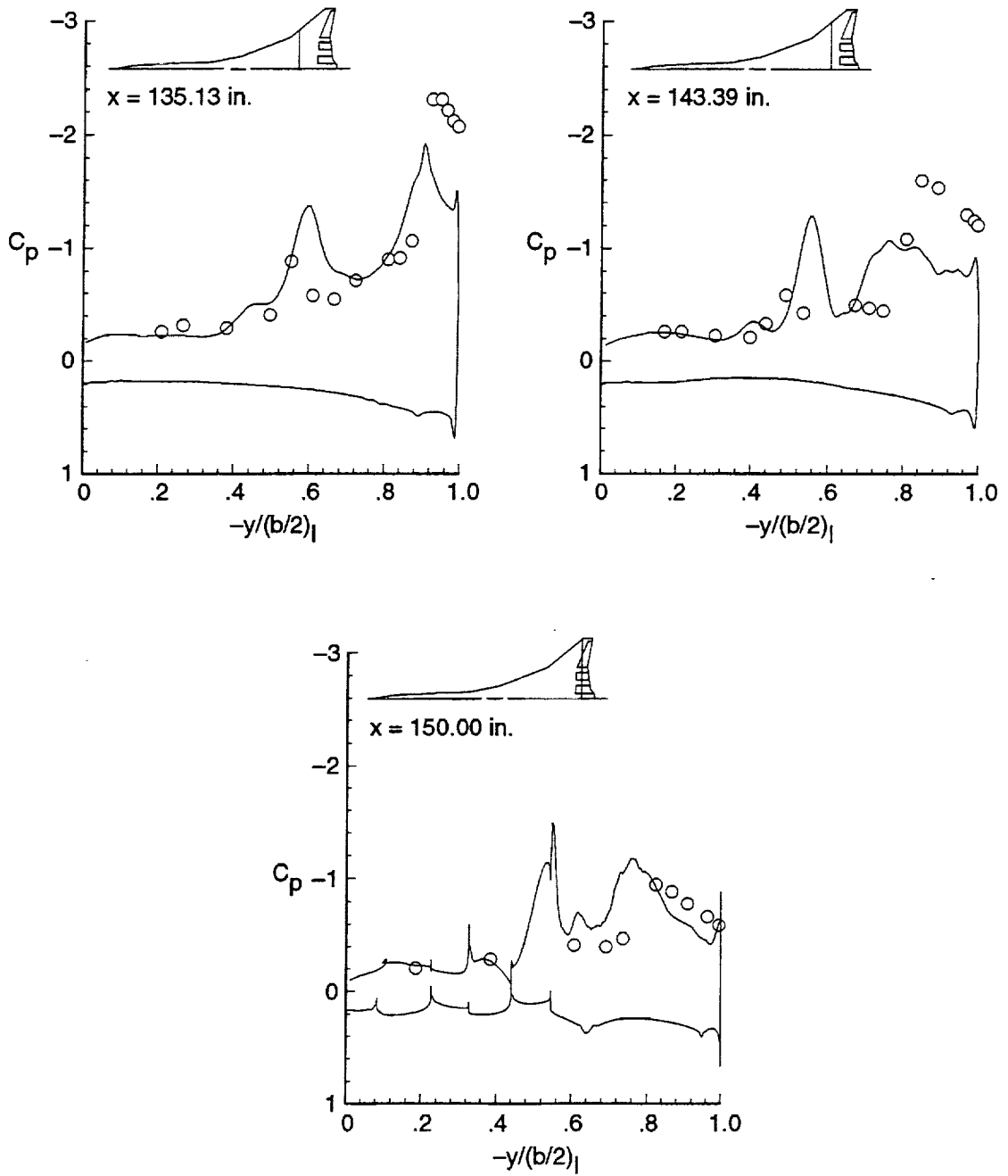


Figure 20. Concluded.



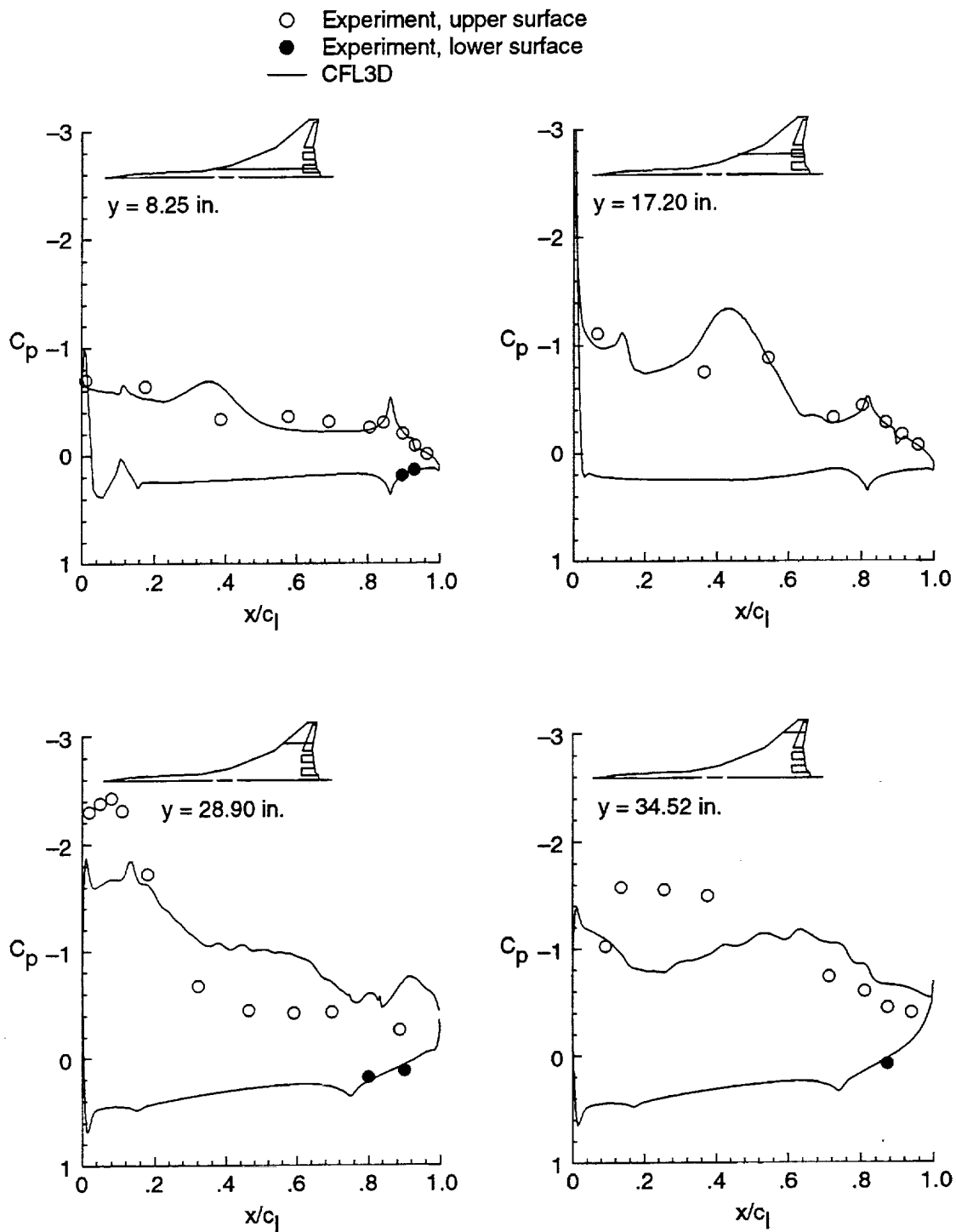


Figure 21. Streamwise distributions of experimental and computational  $C_p$  for Reference H config1 at  $M = 0.24$  and  $\alpha = 15^\circ$ .

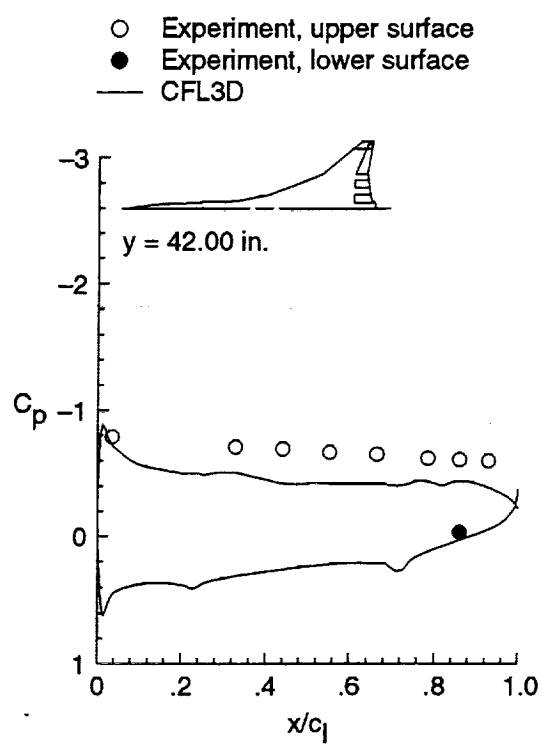


Figure 21. Concluded.

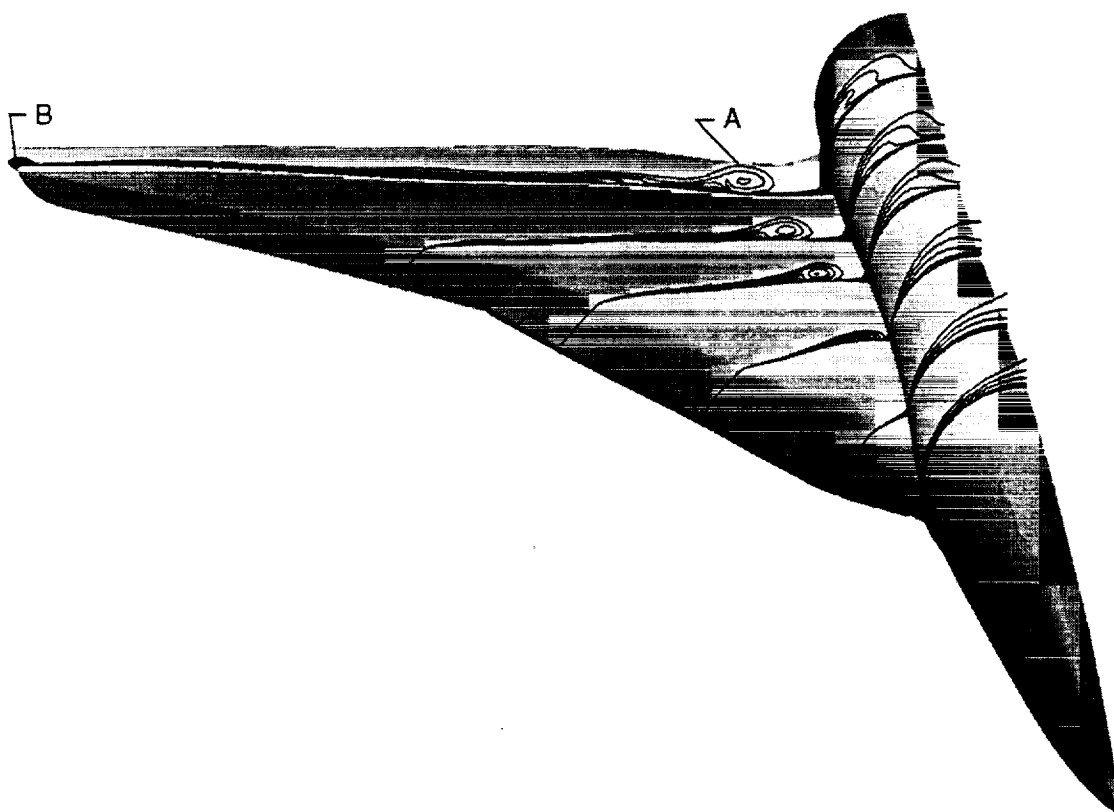


Figure 22. The  $p_t$  contours at several crossflow planes for Reference H config1 at  $M = 0.24$  and  $\alpha = 6^\circ$ .

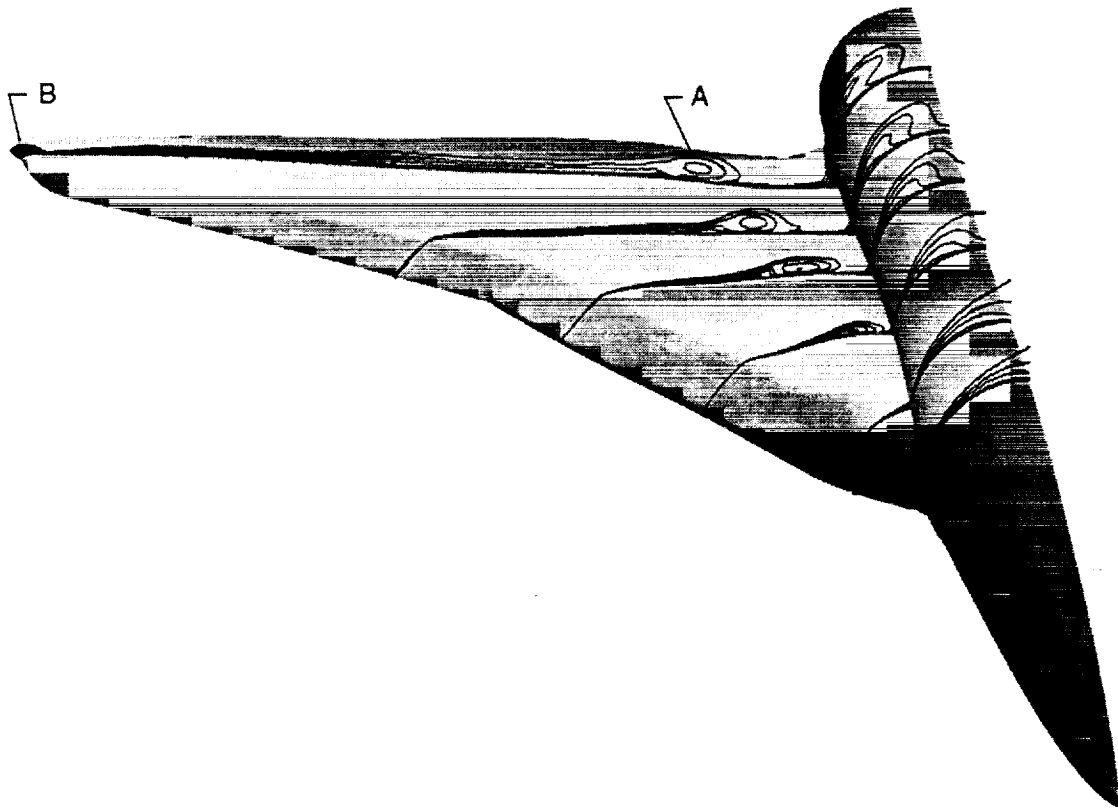


Figure 23. The  $p_t$  contours at several crossflow planes for Reference H config1 at  $M = 0.24$  and  $\alpha = 8^\circ$ .

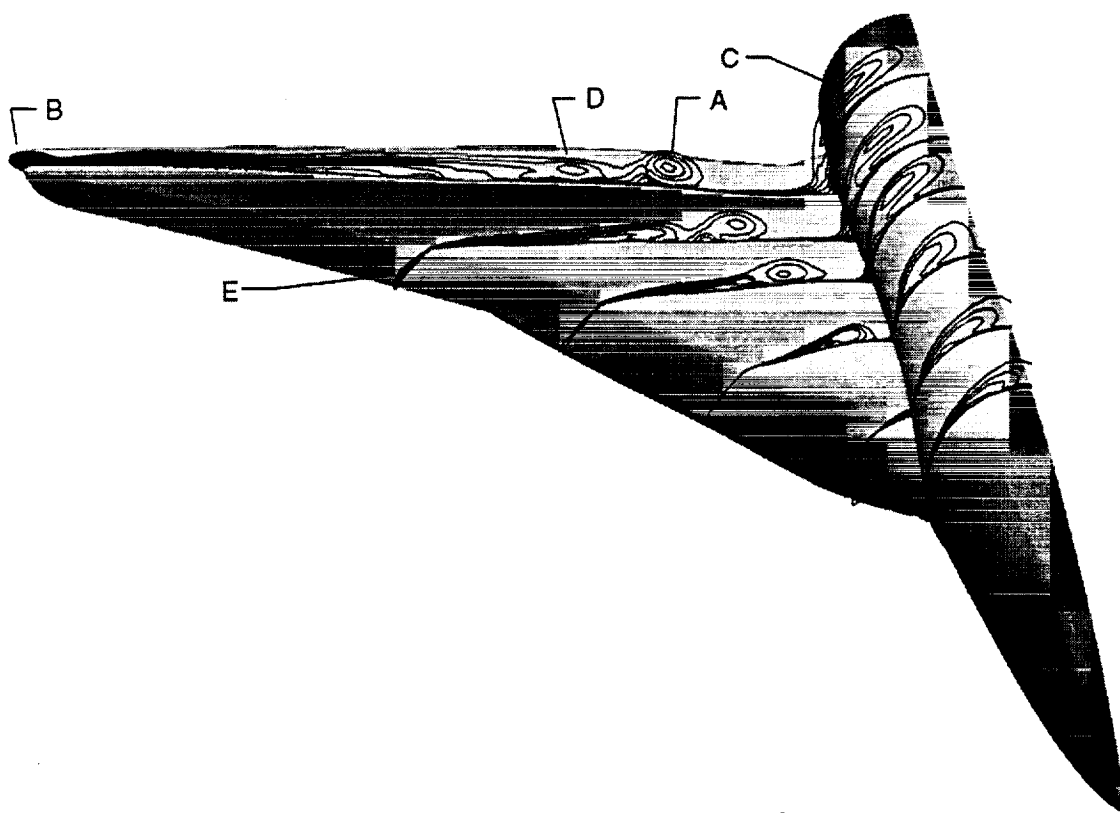


Figure 24. The  $p_t$  contours at several crossflow planes for Reference H config1 at  $M = 0.24$  and  $\alpha = 10^\circ$ .

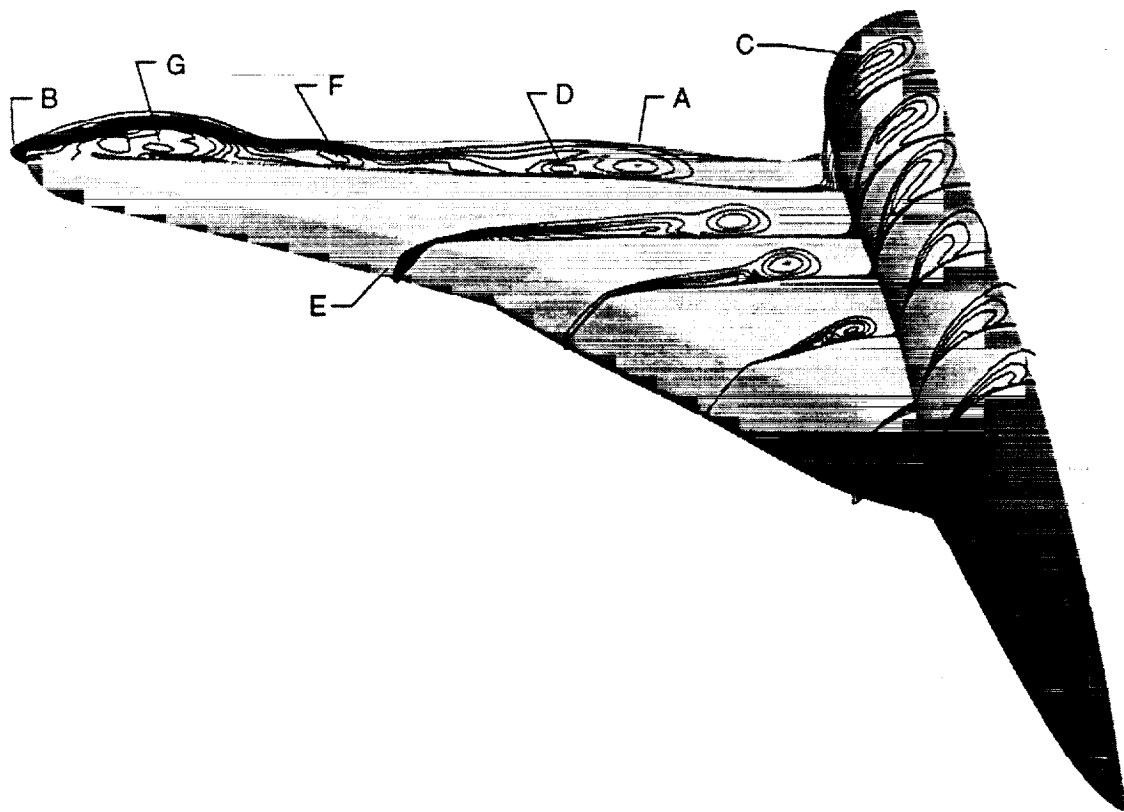


Figure 25. The  $p_t$  contours at several crossflow planes for Reference H config1 at  $M = 0.24$  and  $\alpha = 12^\circ$ .

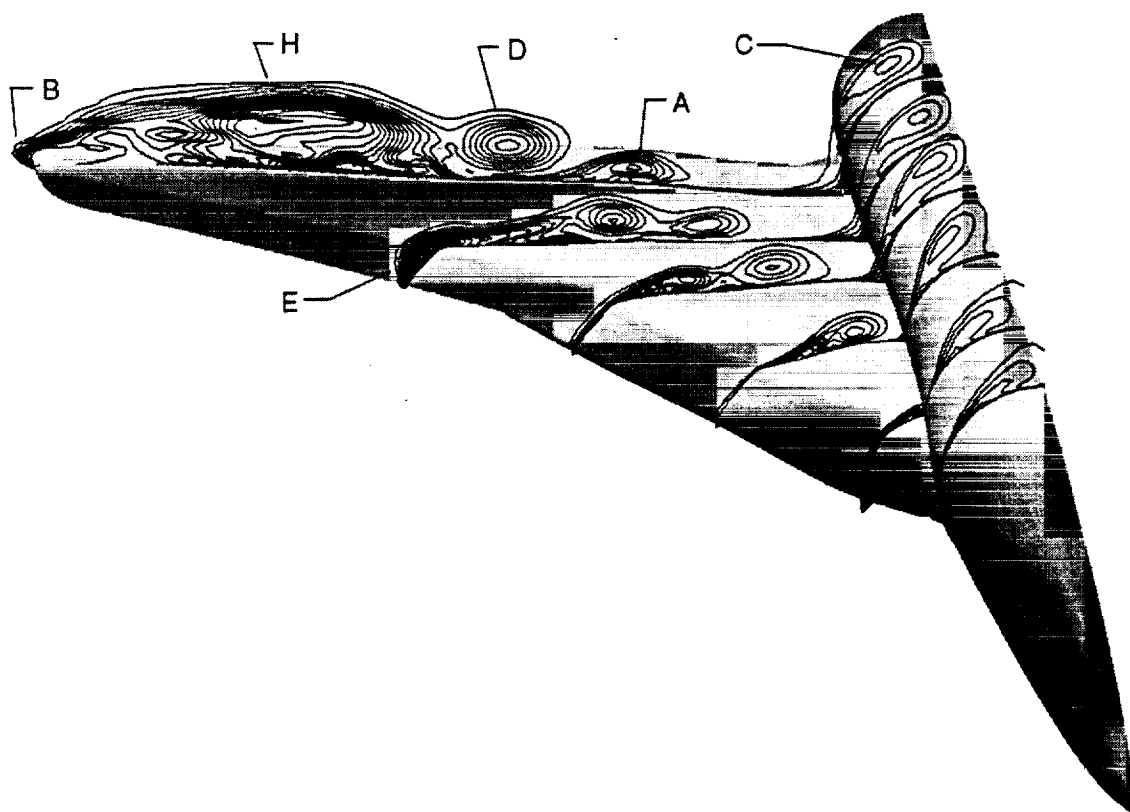


Figure 26. The  $p_t$  contours at several crossflow planes for Reference H config1 at  $M = 0.24$  and  $\alpha = 15^\circ$ .

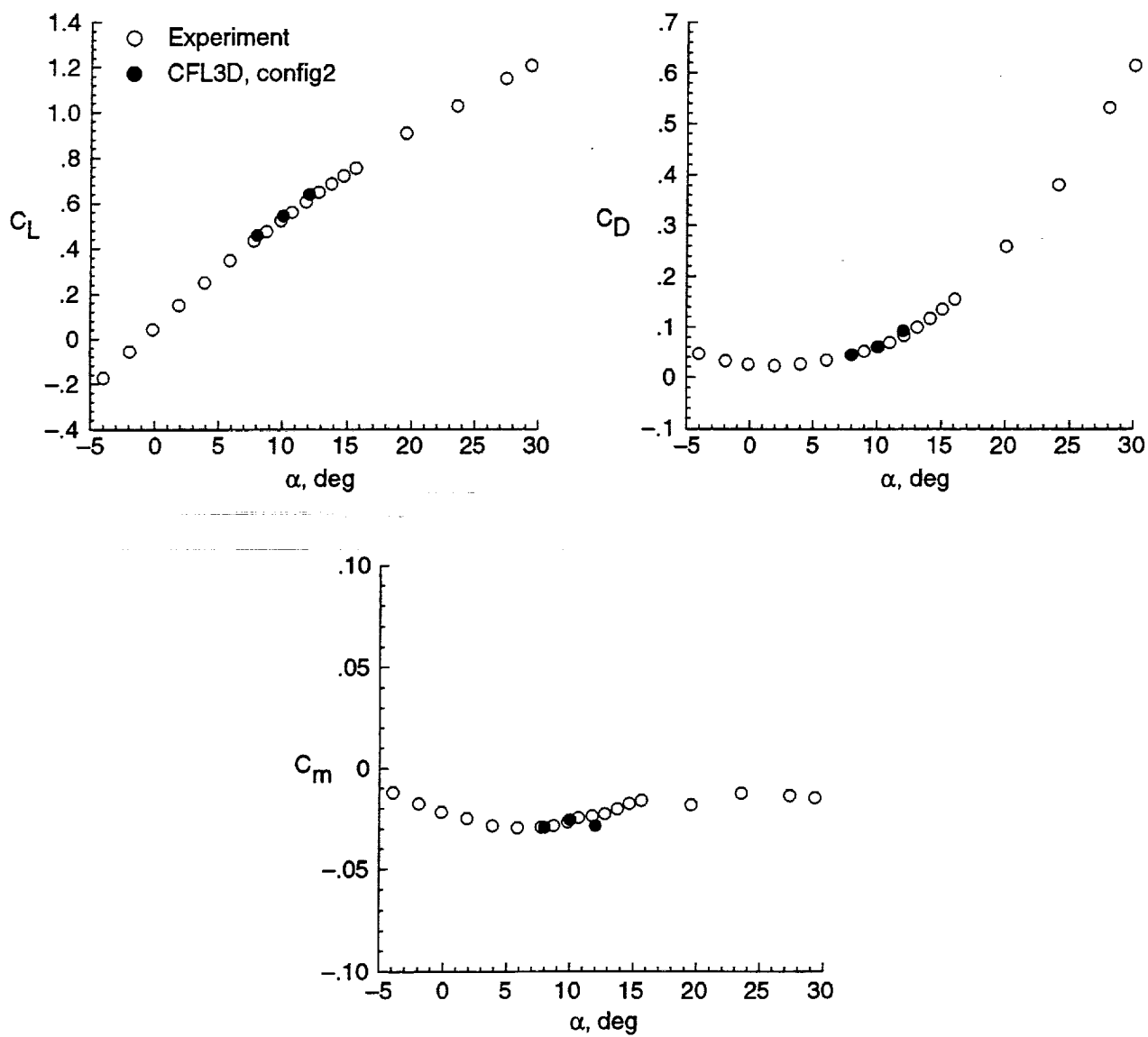


Figure 27. Force and moment comparisons for Reference H config2 at  $\beta = 0^\circ$ .



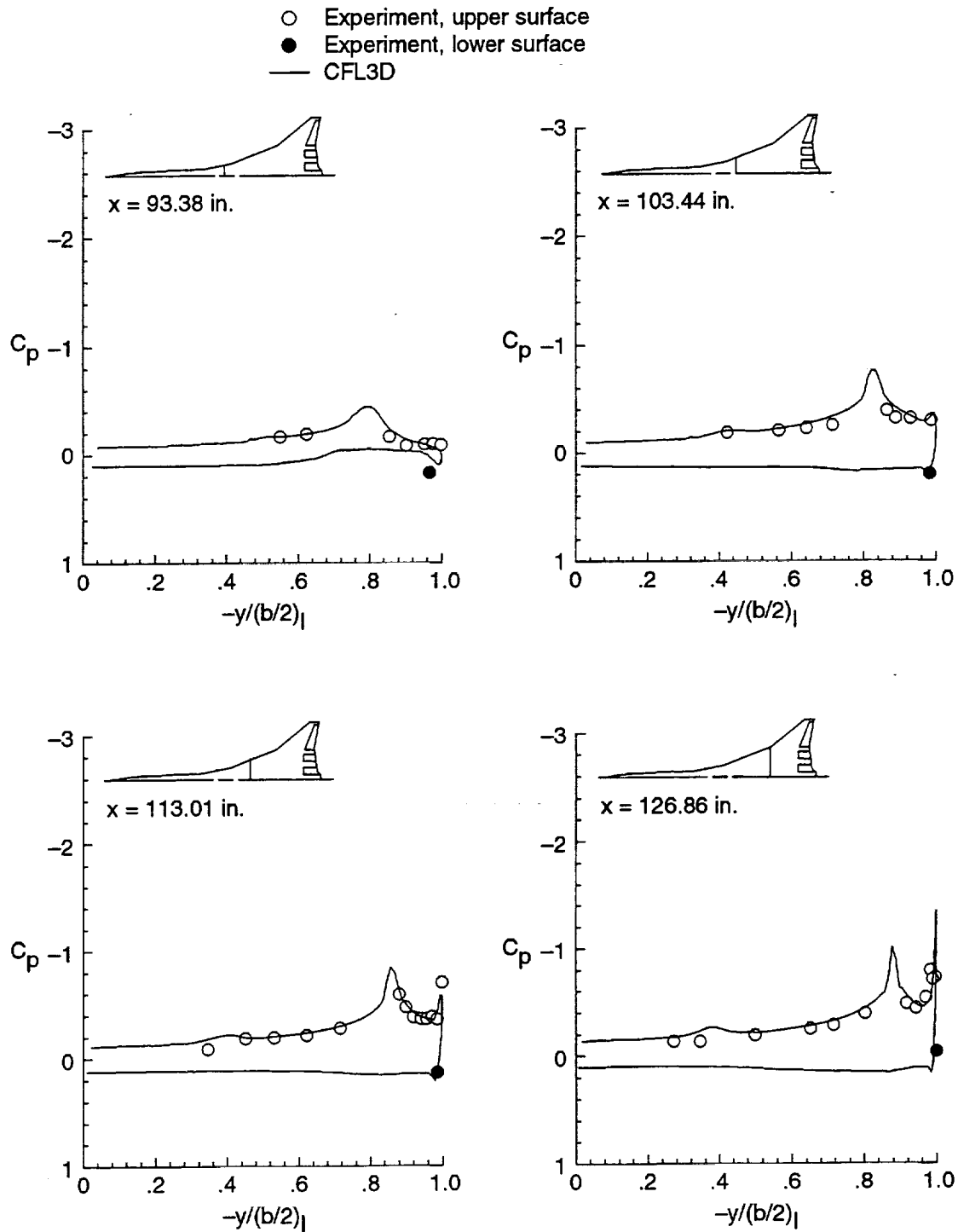


Figure 28. Spanwise distributions of experimental and computational  $C_p$  for Reference H config2 at  $M = 0.24$  and  $\alpha = 8^\circ$ .

○ Experiment, upper surface  
 — CFL3D

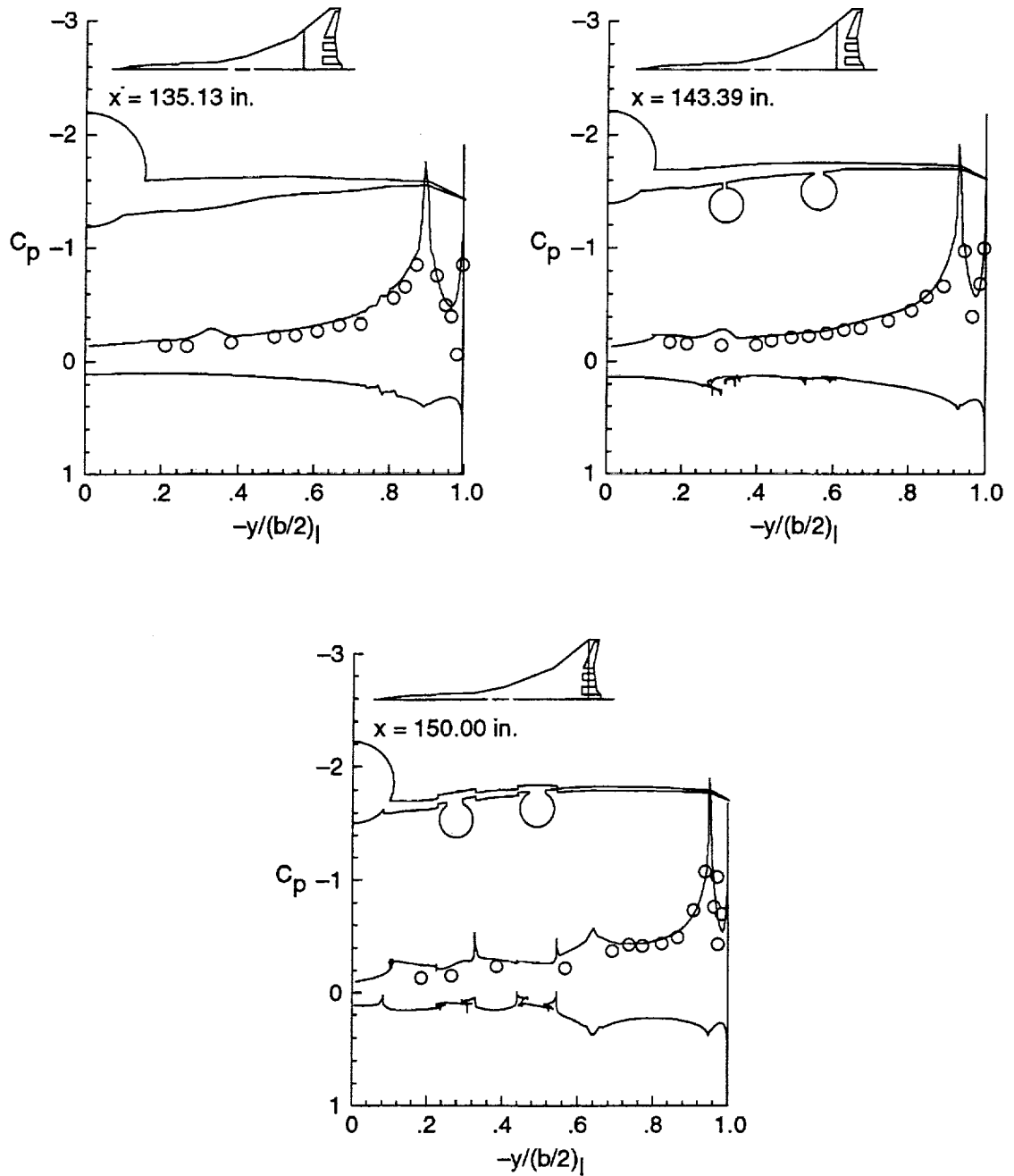


Figure 28. Concluded.

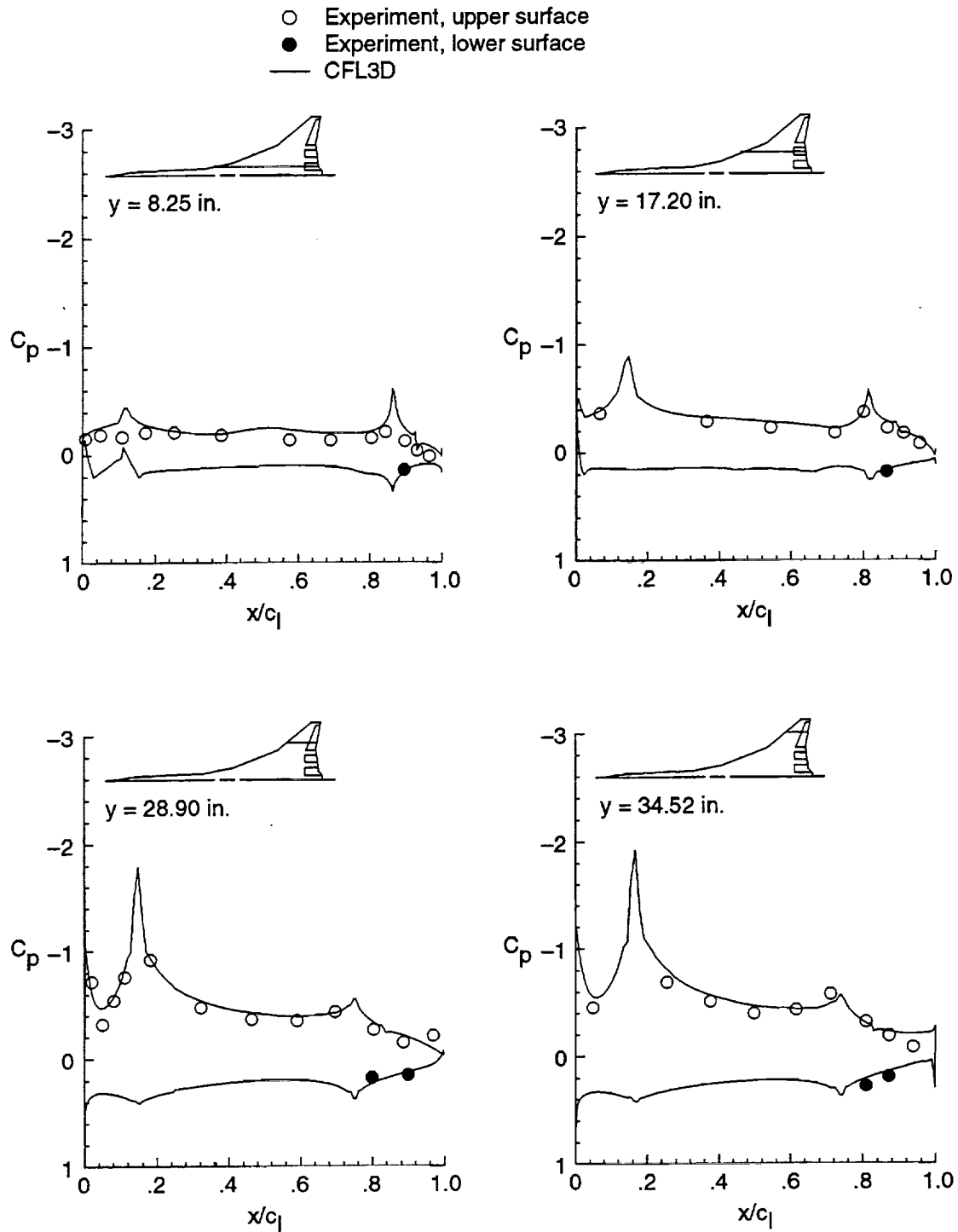


Figure 29. Streamwise distributions of experimental and computational  $C_p$  for Reference H config2 at  $M = 0.24$  and  $\alpha = 8^\circ$ .

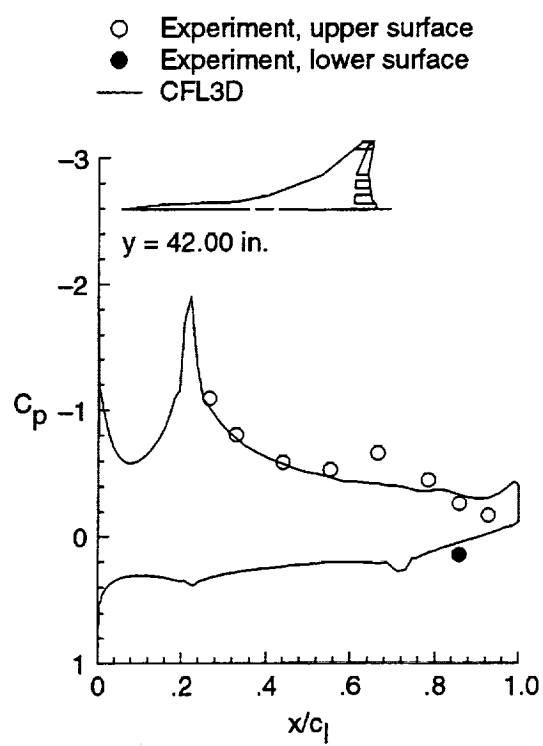


Figure 29. Concluded.

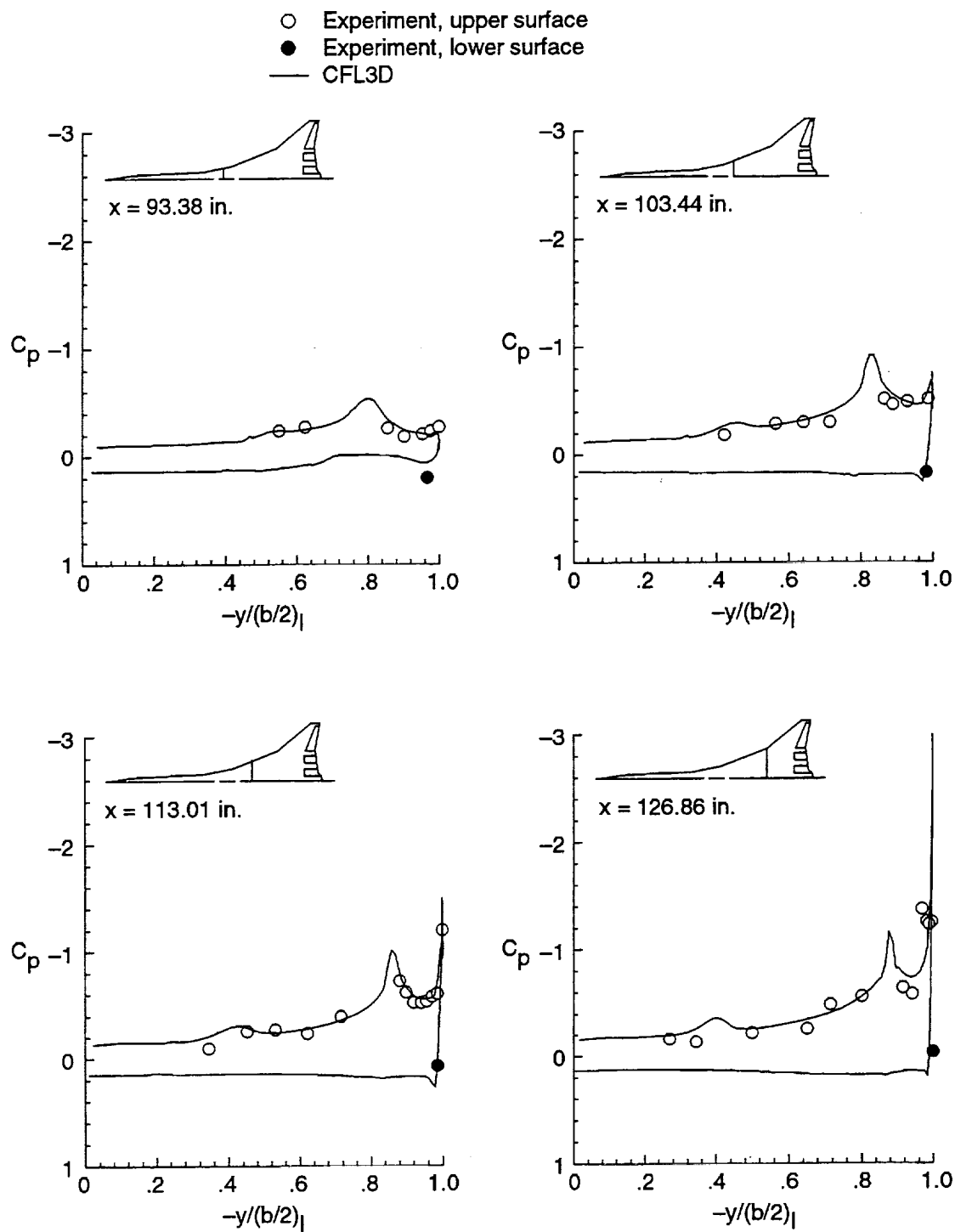


Figure 30. Spanwise distributions of experimental and computational  $C_p$  for Reference H config2 at  $M = 0.24$  and  $\alpha = 10^\circ$ .

○ Experiment, upper surface  
 — CFL3D

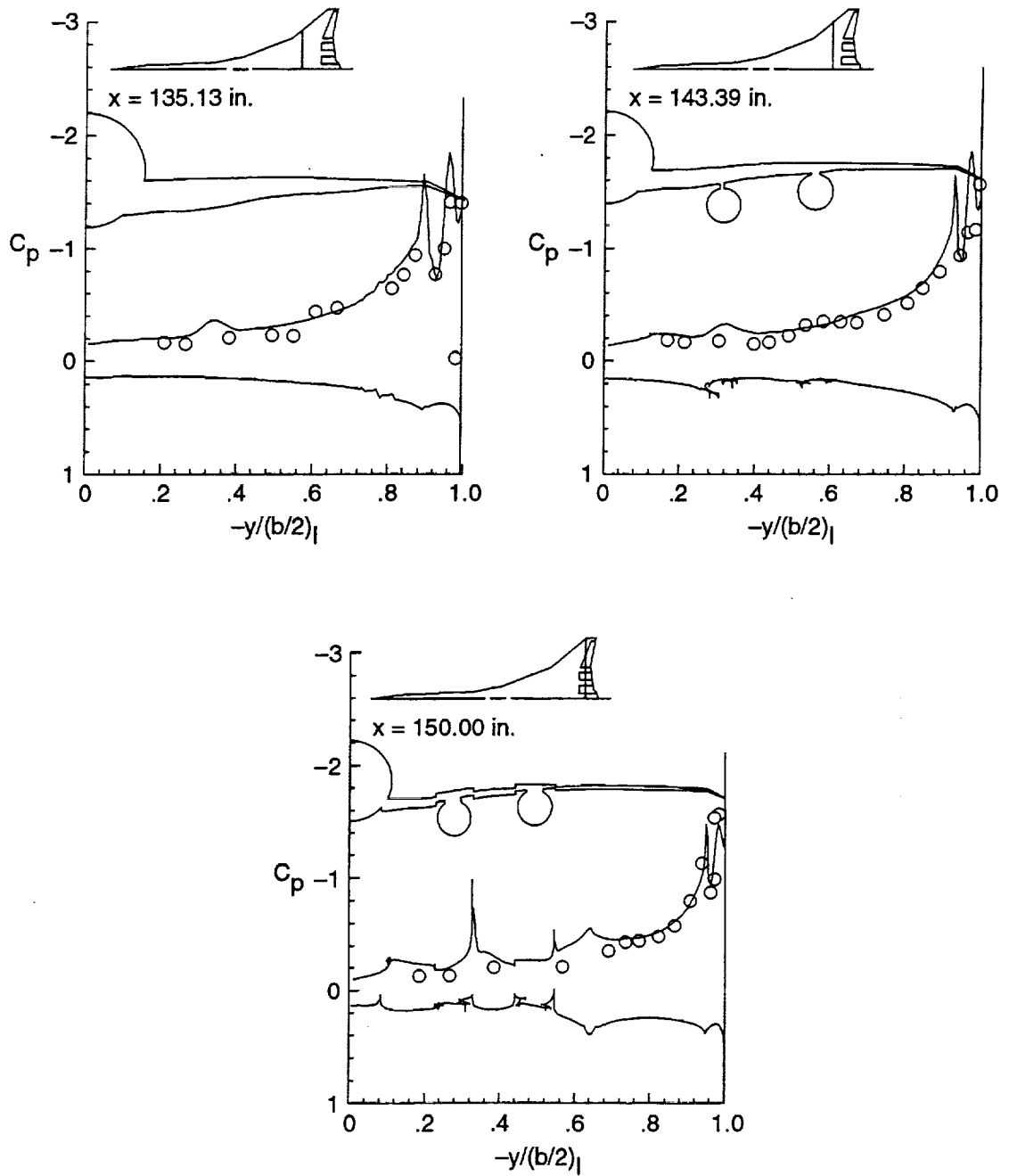


Figure 30. Concluded.

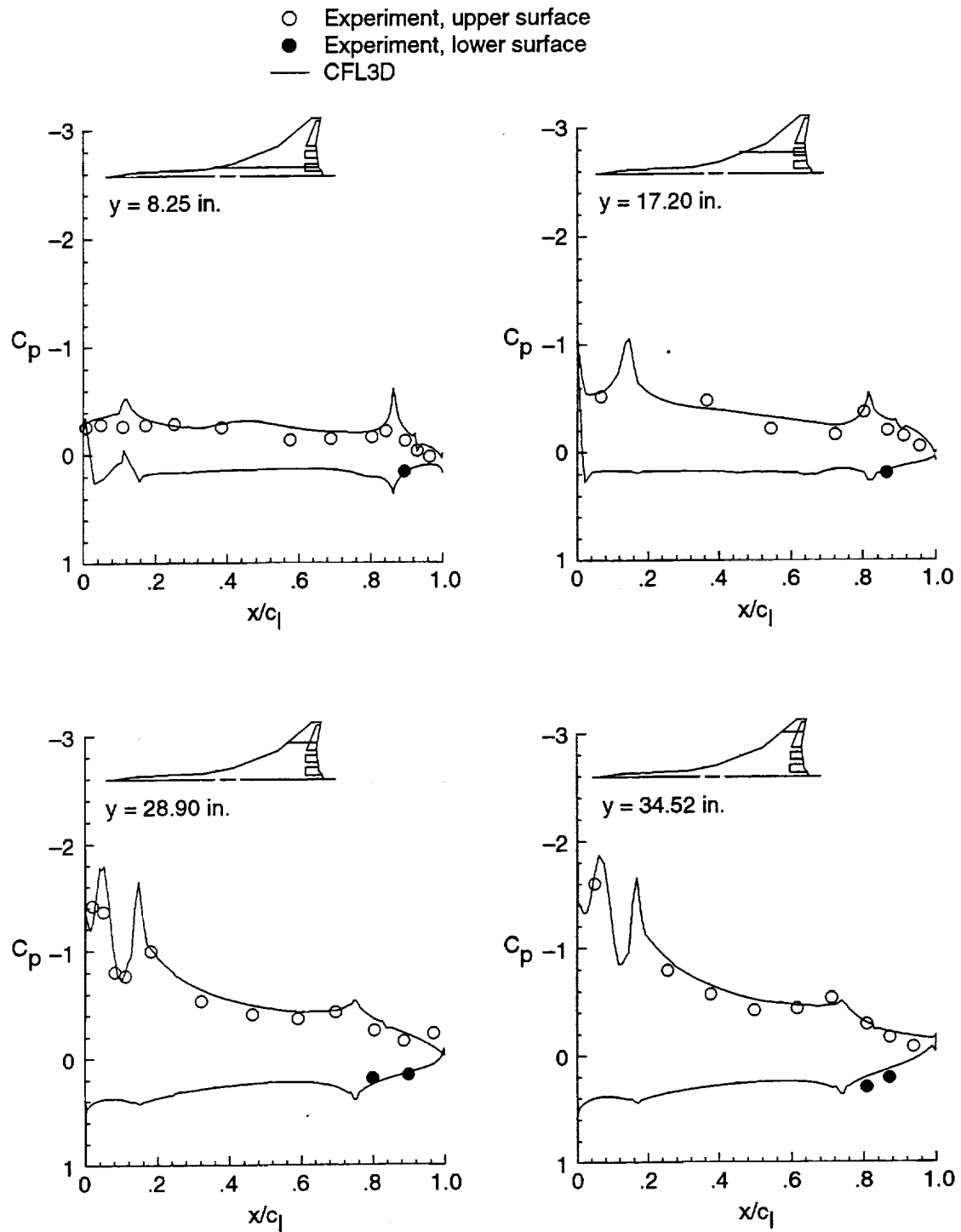


Figure 31. Streamwise distributions of experimental and computational  $C_p$  for Reference H config2 at  $M = 0.24$  and  $\alpha = 10^\circ$ .

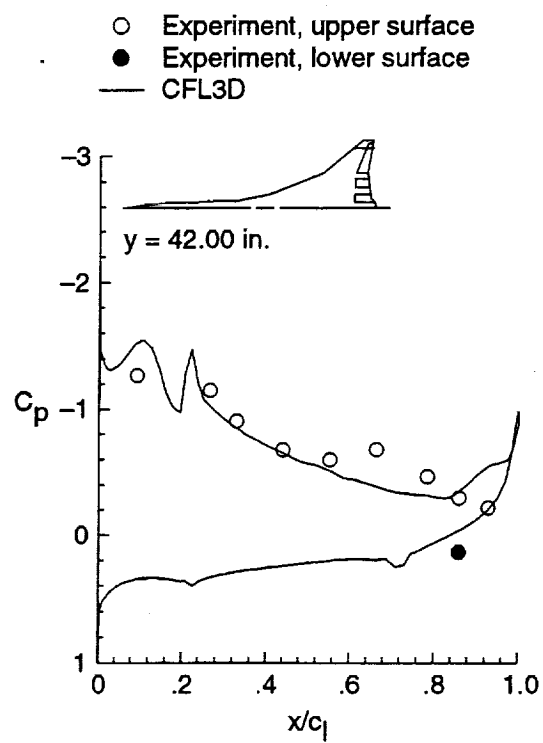


Figure 31. Concluded.



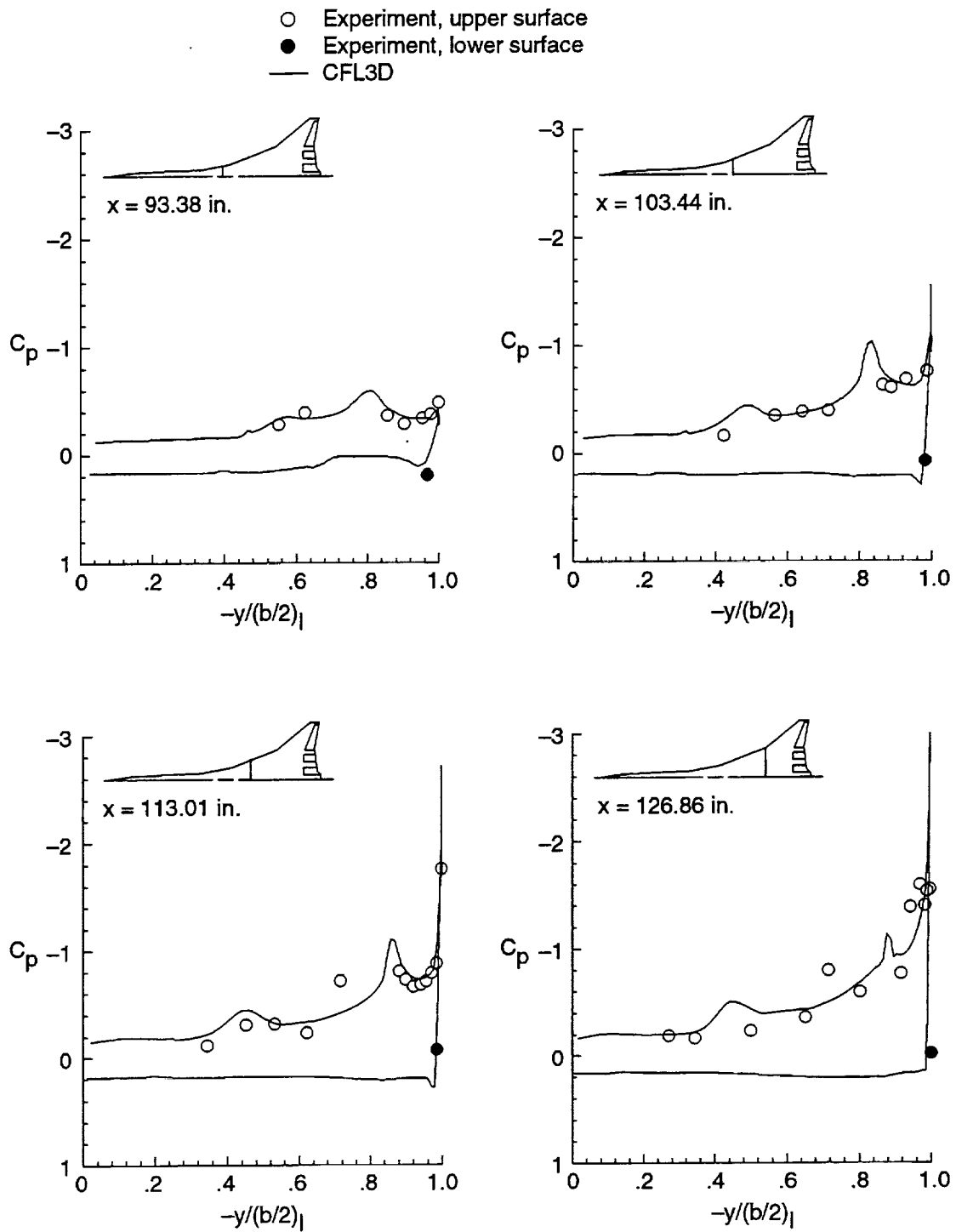


Figure 32. Spanwise distributions of experimental and computational  $C_p$  for Reference H config2 at  $M = 0.24$  and  $\alpha = 12^\circ$ .

○ Experiment, upper surface  
 — CFL3D

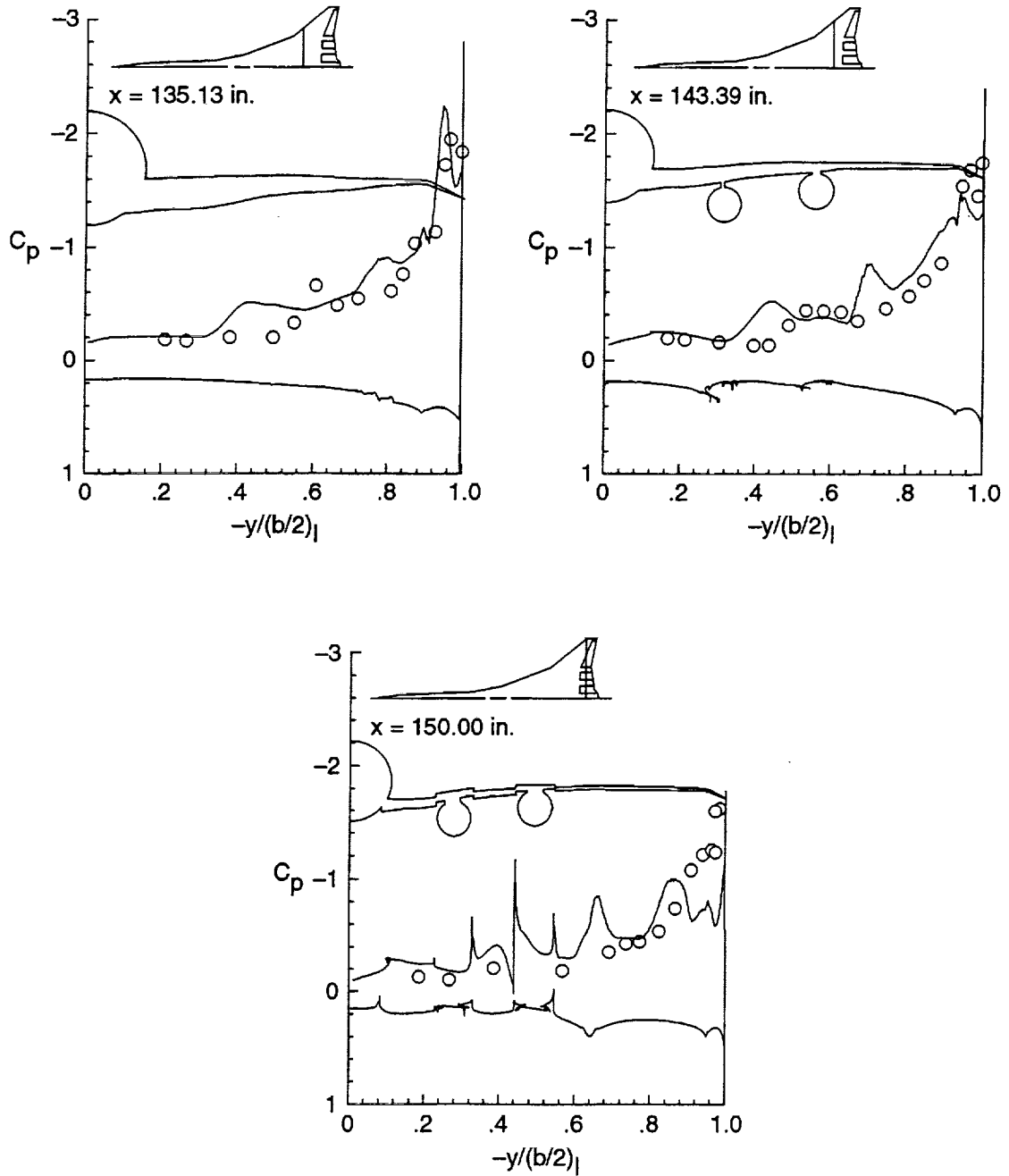


Figure 32. Concluded.

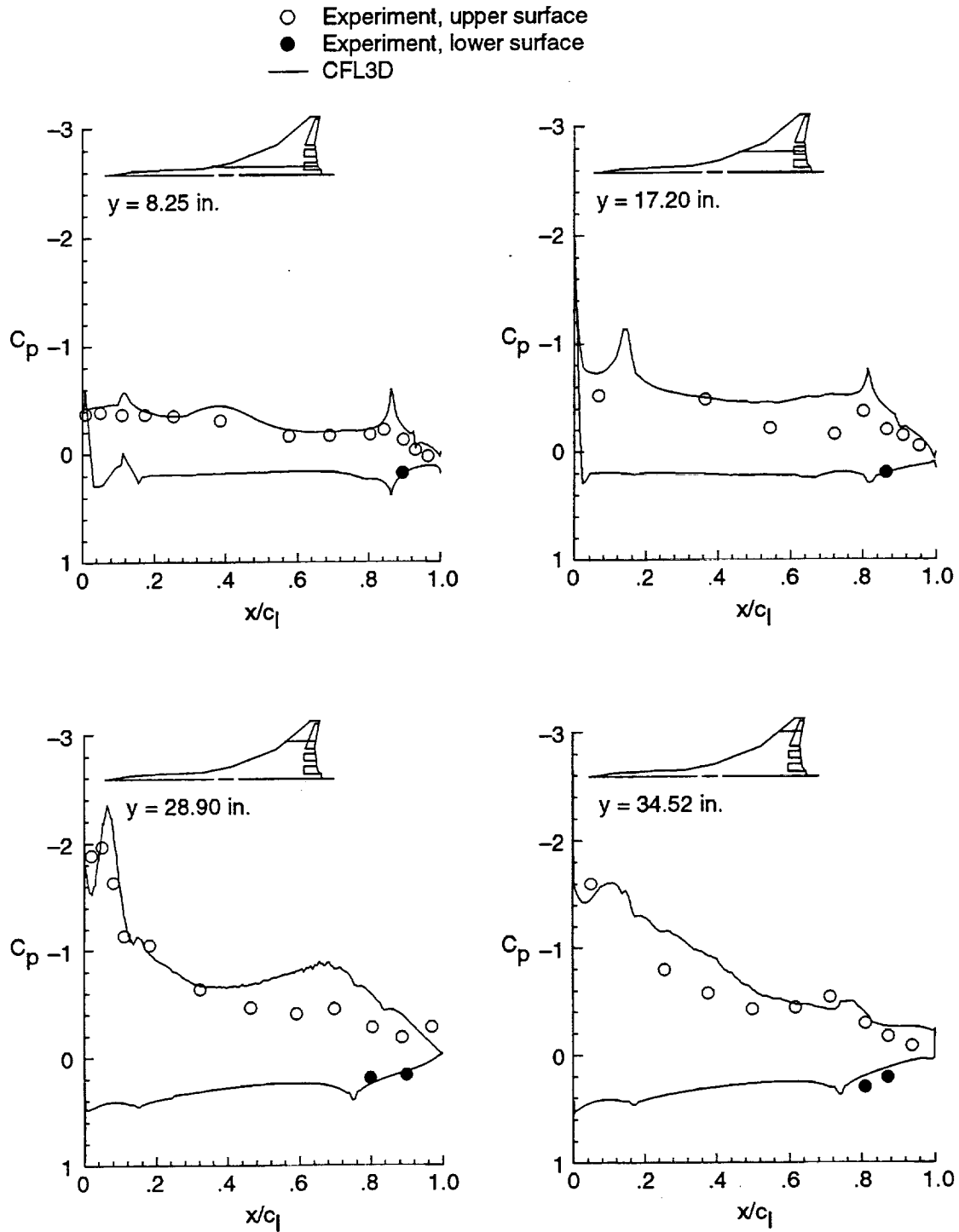


Figure 33. Streamwise distributions of experimental and computational  $C_p$  for Reference H config2 at  $M = 0.24$  and  $\alpha = 12^\circ$ .

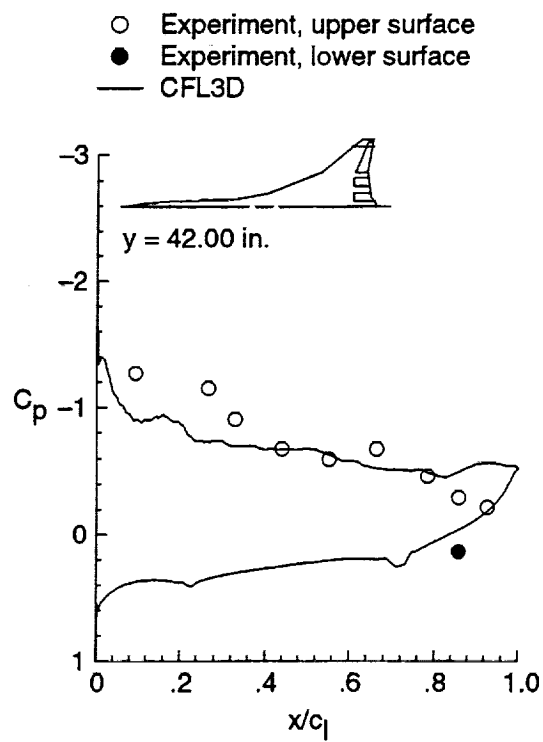
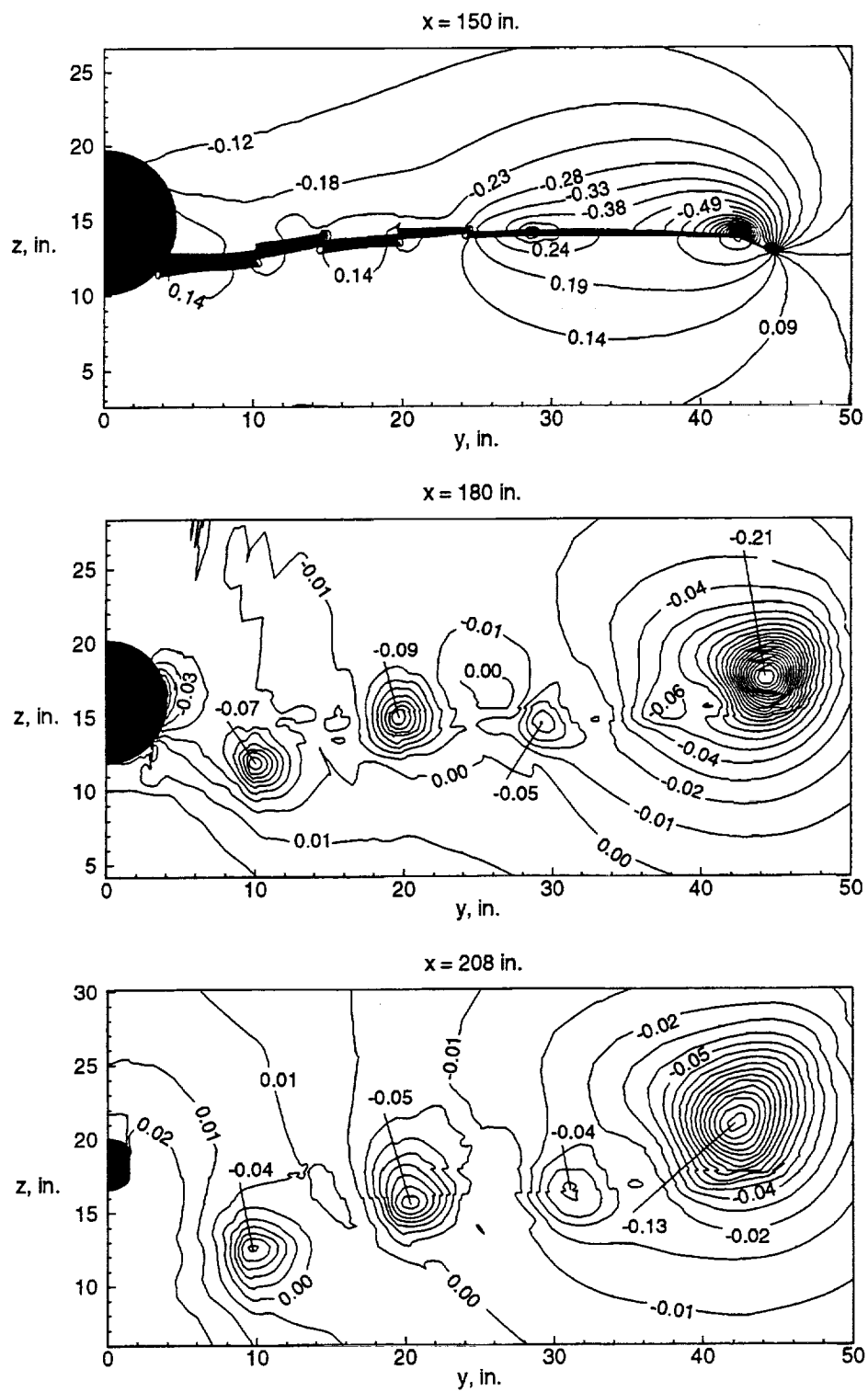


Figure 33. Concluded.

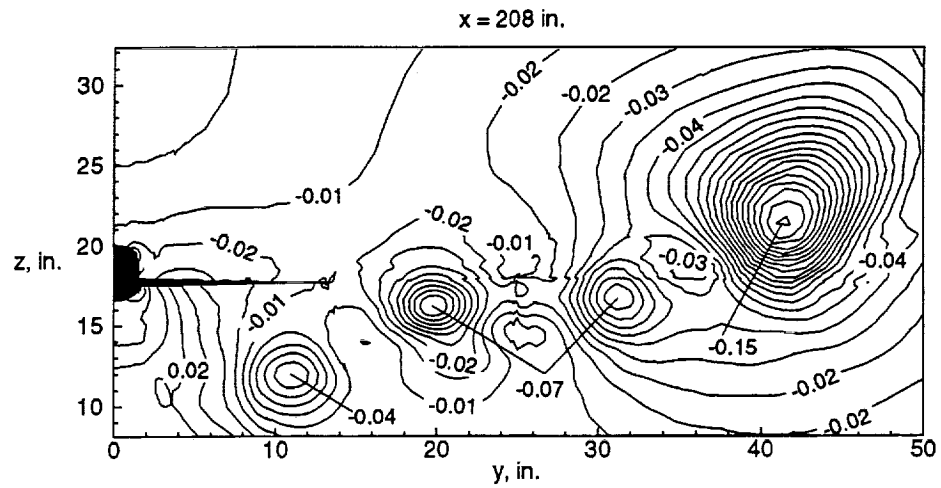
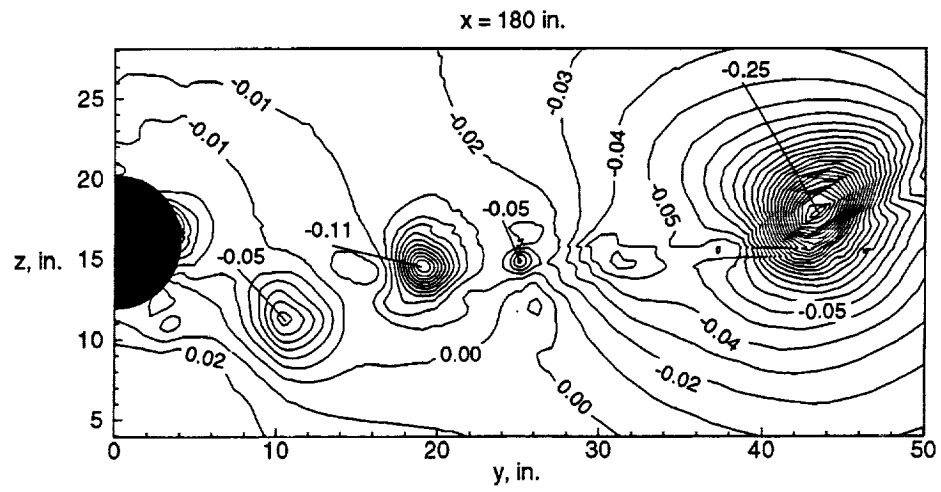
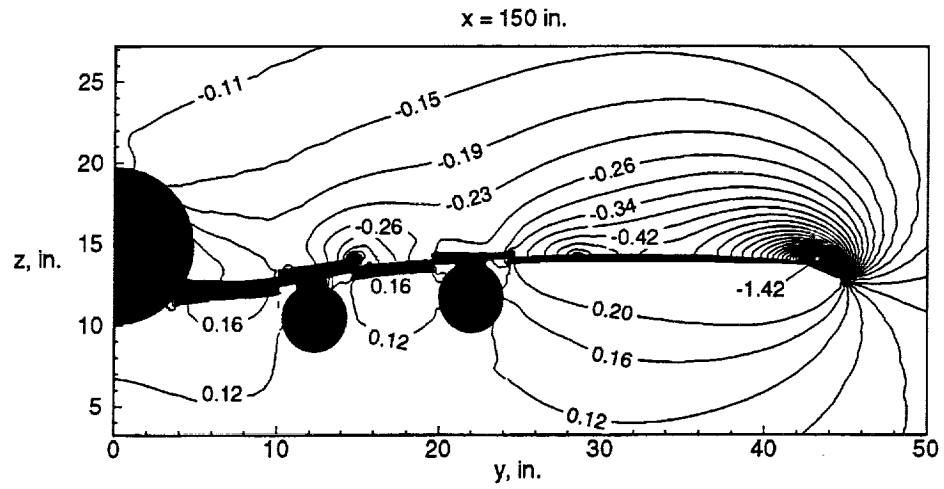


(a) Config1,  $\alpha = 8^\circ$ .

Figure 34. The  $C_p$  contours at several constant fuselage stations for Reference H.



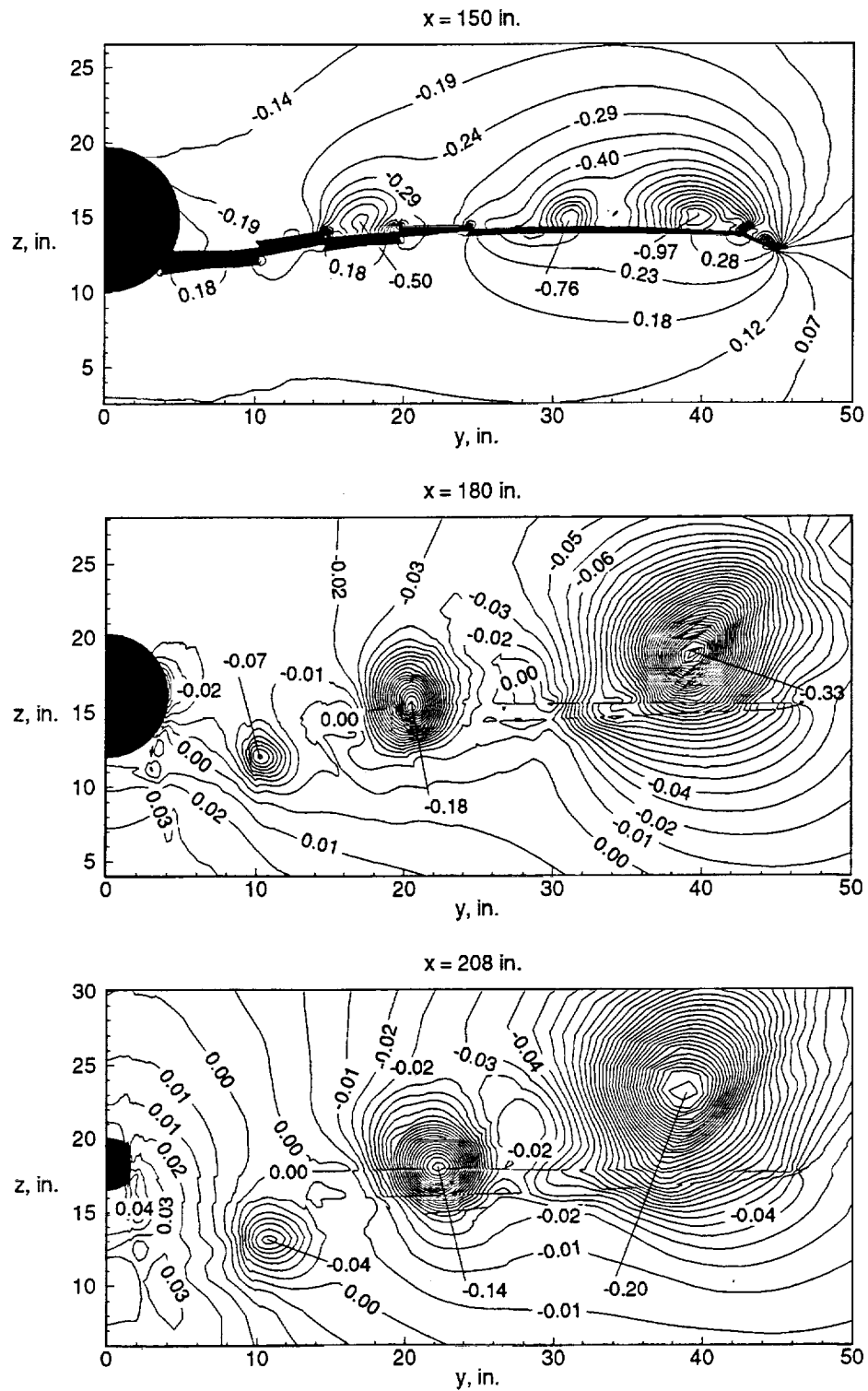




(b) Config2,  $\alpha = 10^\circ$ .

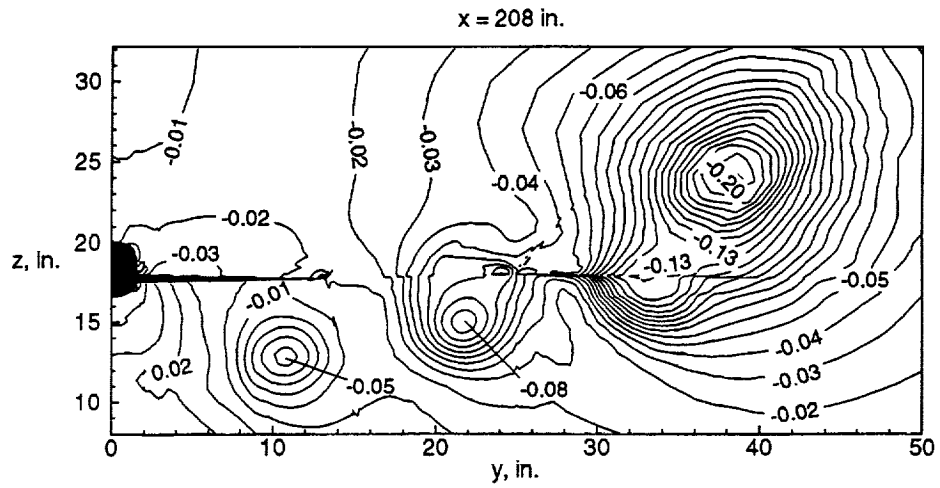
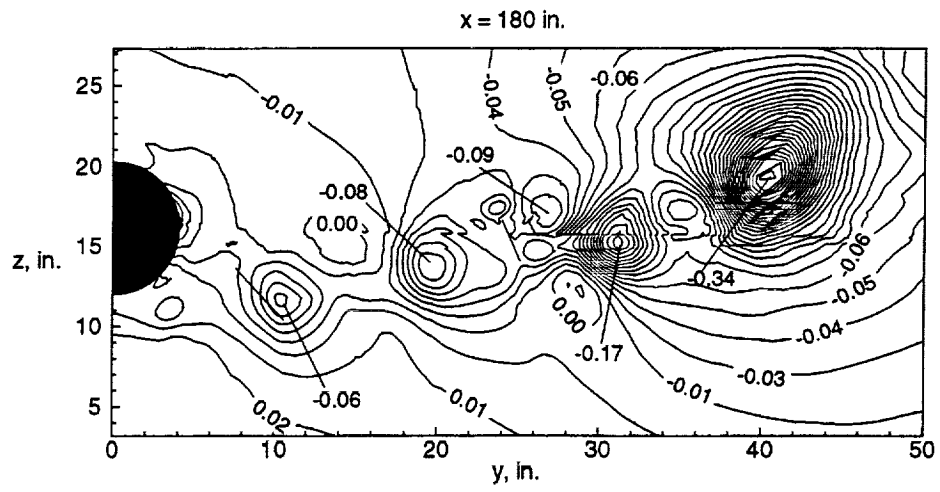
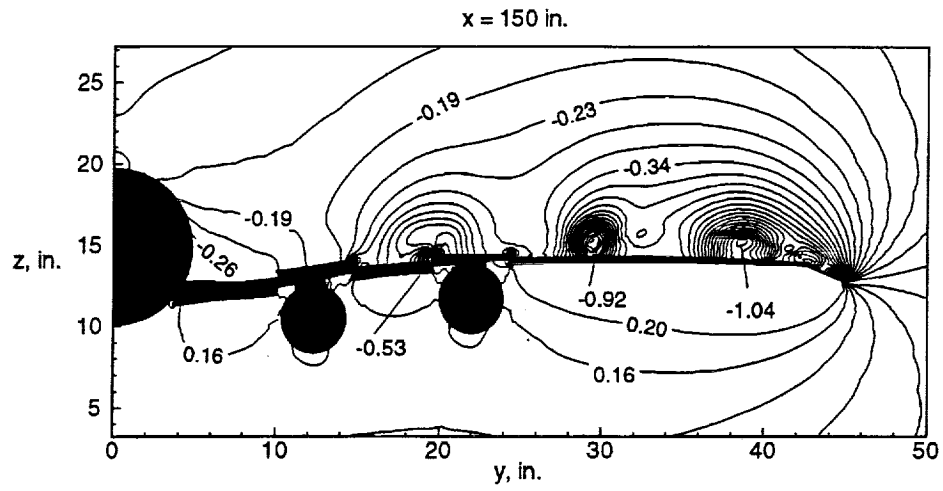
Figure 35. Concluded.





(a) Config1,  $\alpha = 12^\circ$ .

Figure 36. The  $C_p$  contours at several constant fuselage stations for Reference H.



(b) Config2,  $\alpha = 12^\circ$ .

Figure 36. Concluded.

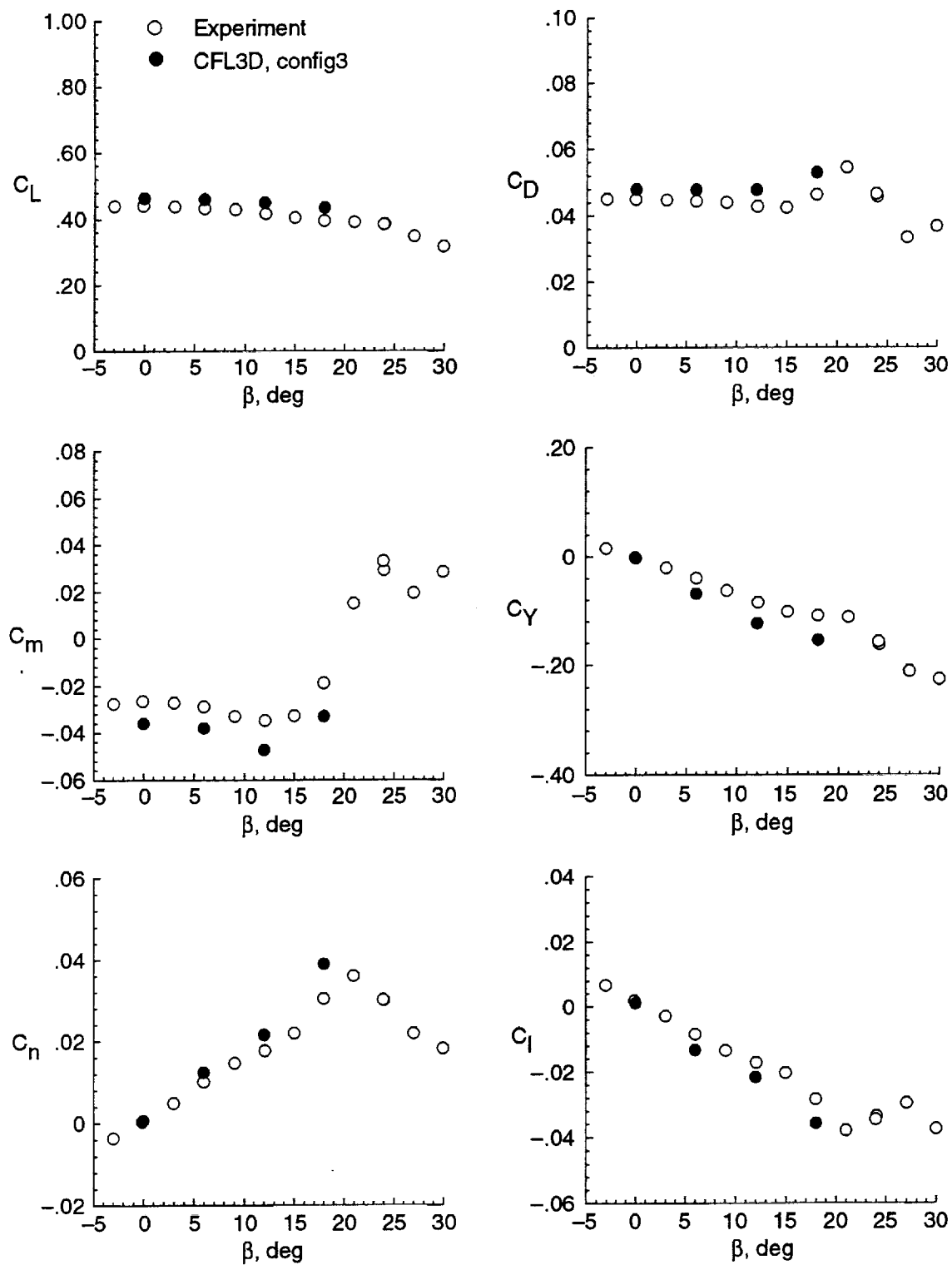


Figure 37. Force and moment comparisons for Reference H config3 at  $\alpha = 8^\circ$ .

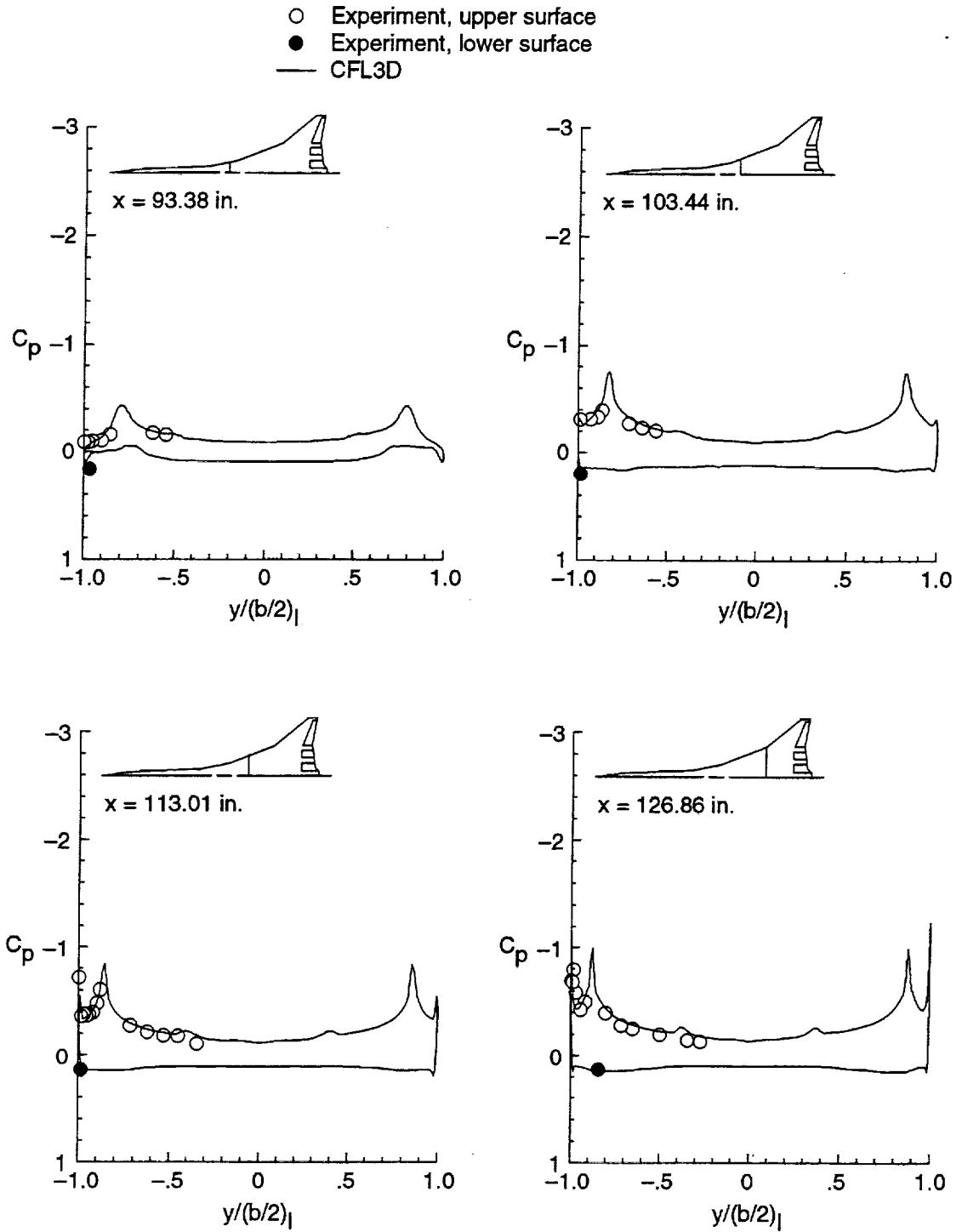


Figure 38. Spanwise distributions of experimental and computational  $C_p$  for Reference H config3 at  $M = 0.24$ ,  $\alpha = 8^\circ$ , and  $\beta = 0^\circ$ .

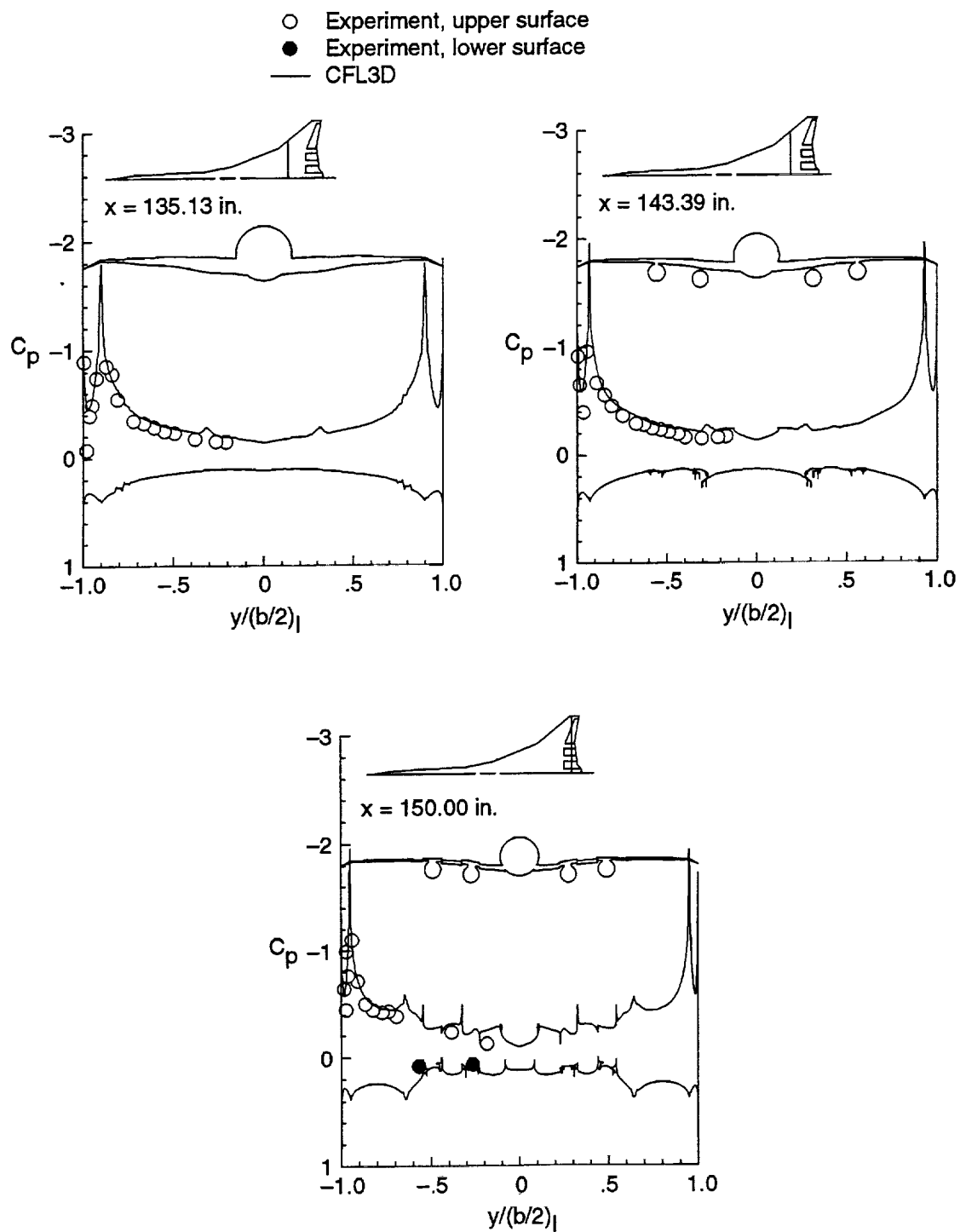


Figure 38. Concluded.

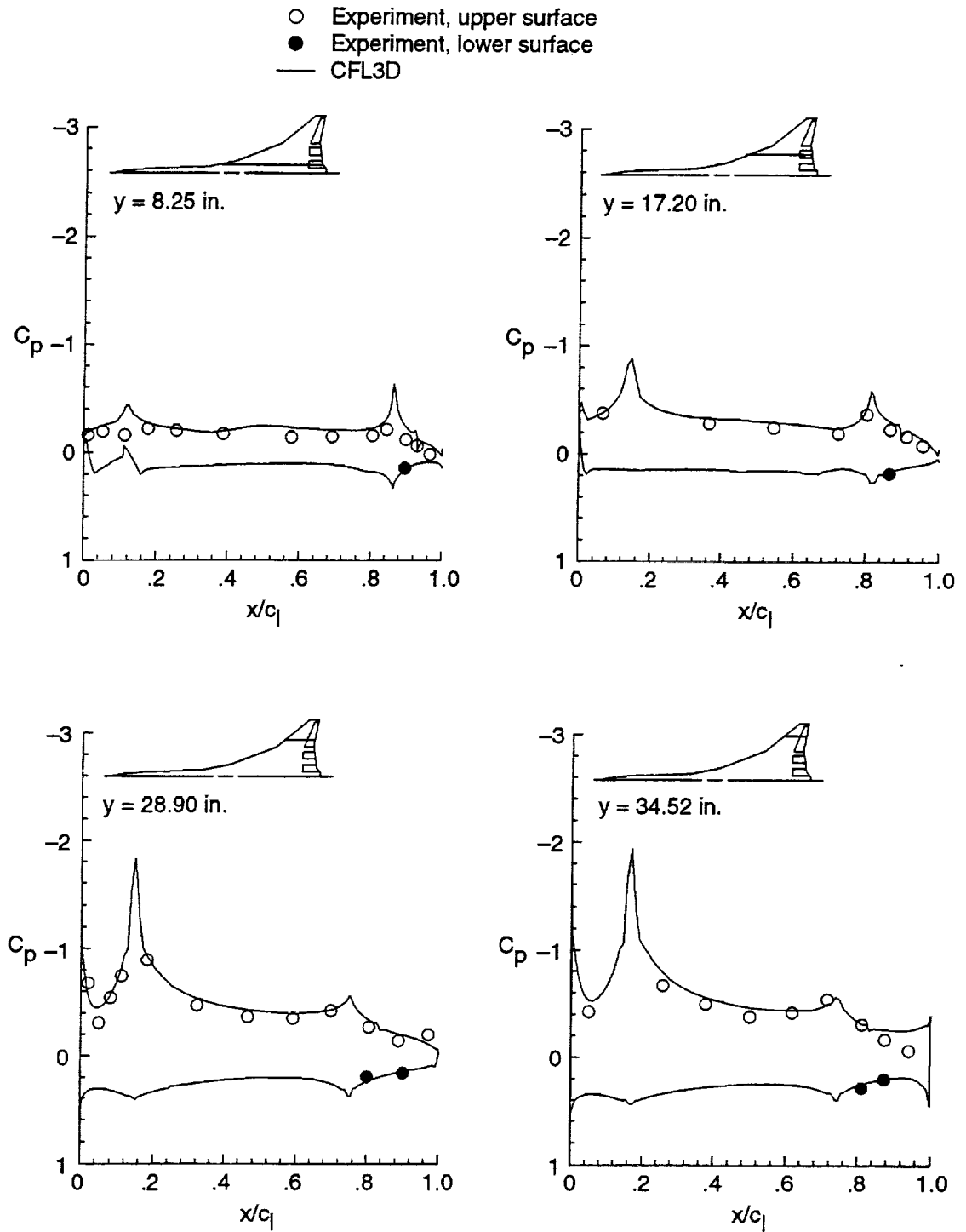


Figure 39. Streamwise distributions of experimental and computational  $C_p$  for Reference H config3 at  $M = 0.24$ ,  $\alpha = 8^\circ$ , and  $\beta = 0^\circ$ .

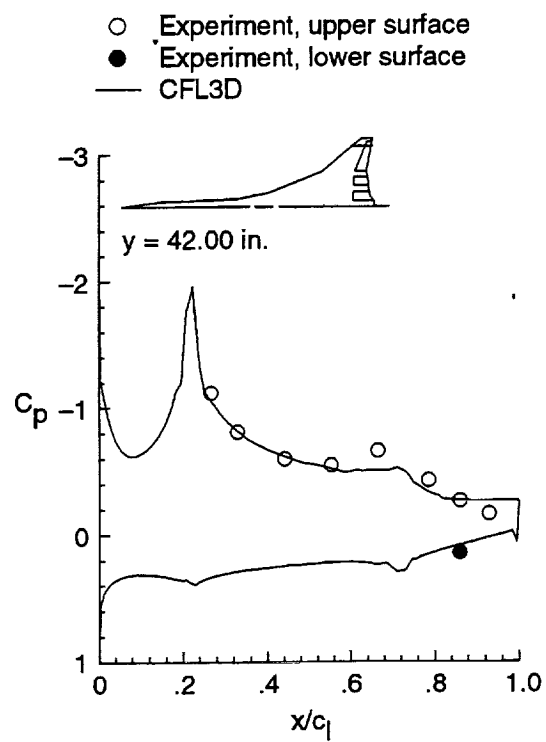


Figure 39. Concluded.

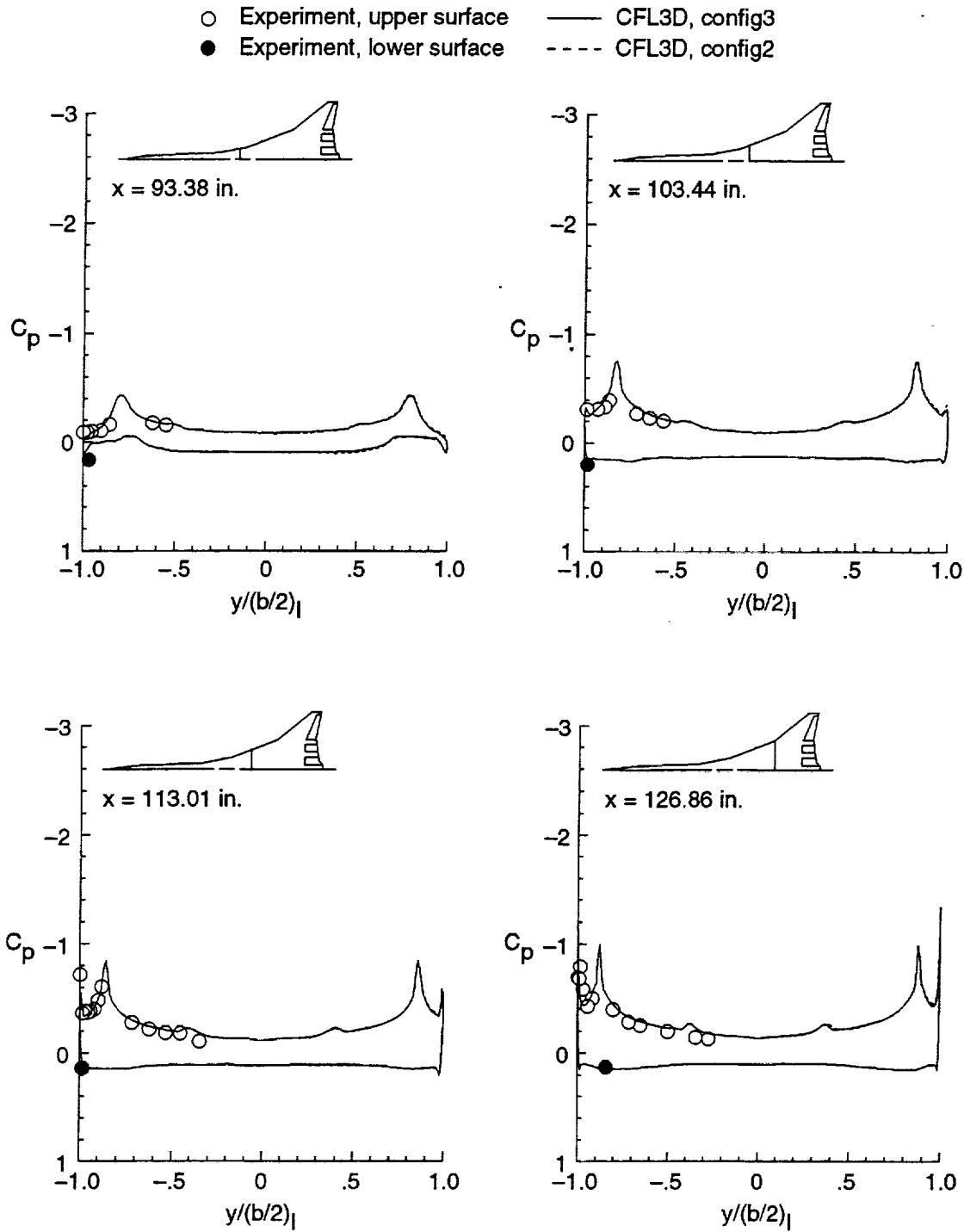


Figure 40. Comparison of spanwise distributions of experimental and computational  $C_p$  for Reference H config2 and config3 at  $M = 0.24$ ,  $\alpha = 8^\circ$ , and  $\beta = 0^\circ$ .



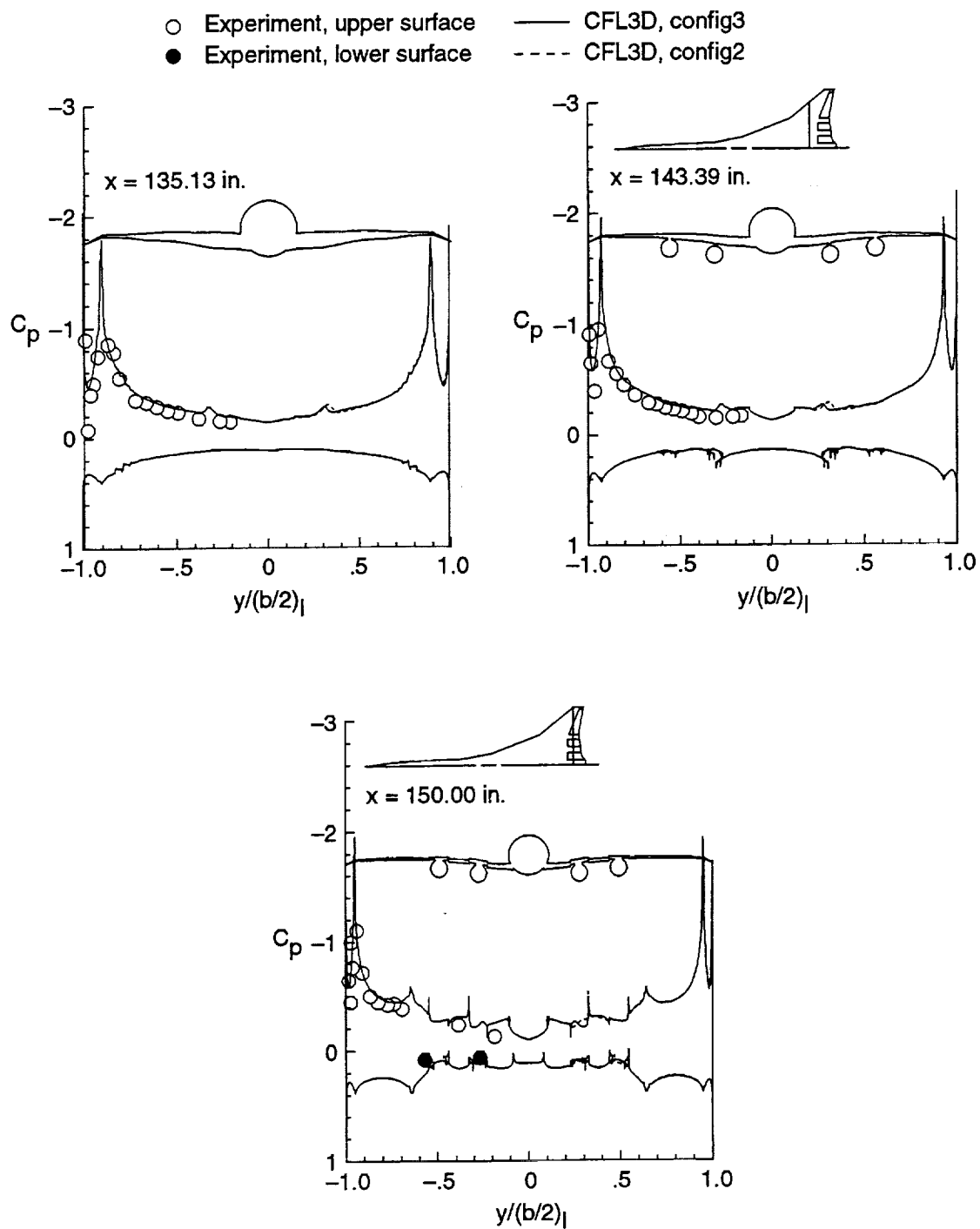


Figure 40. Concluded.

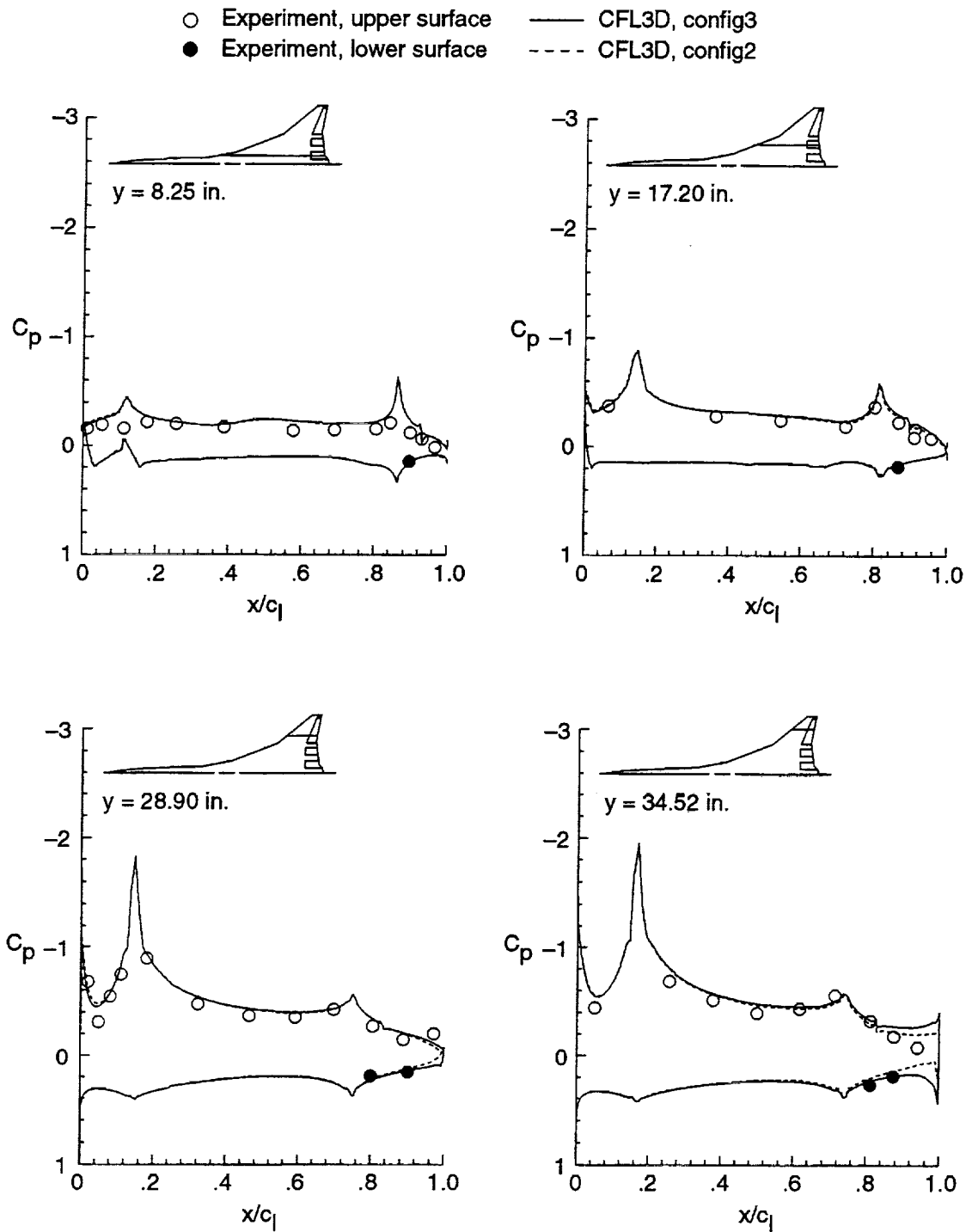


Figure 41. Comparison of spanwise distributions of experimental and computational  $C_p$  for Reference H config2 and config3 at  $M = 0.24$ ,  $\alpha = 8^\circ$ , and  $\beta = 0^\circ$ .

- Experiment, upper surface      — CFL3D, config3
- Experiment, lower surface      - - - CFL3D, config2

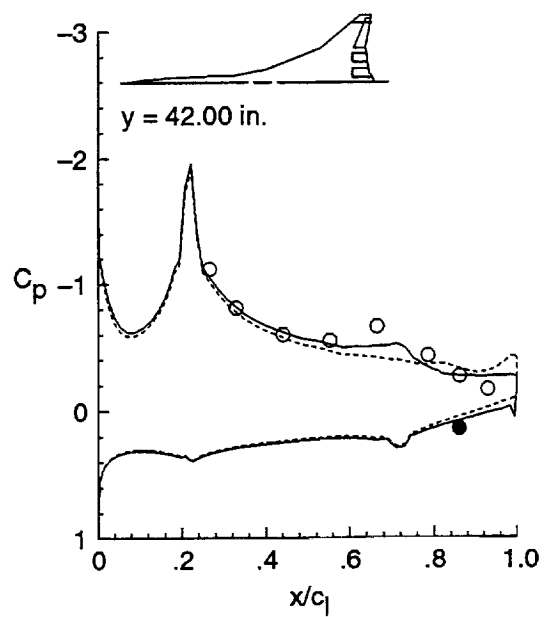


Figure 41. Concluded.

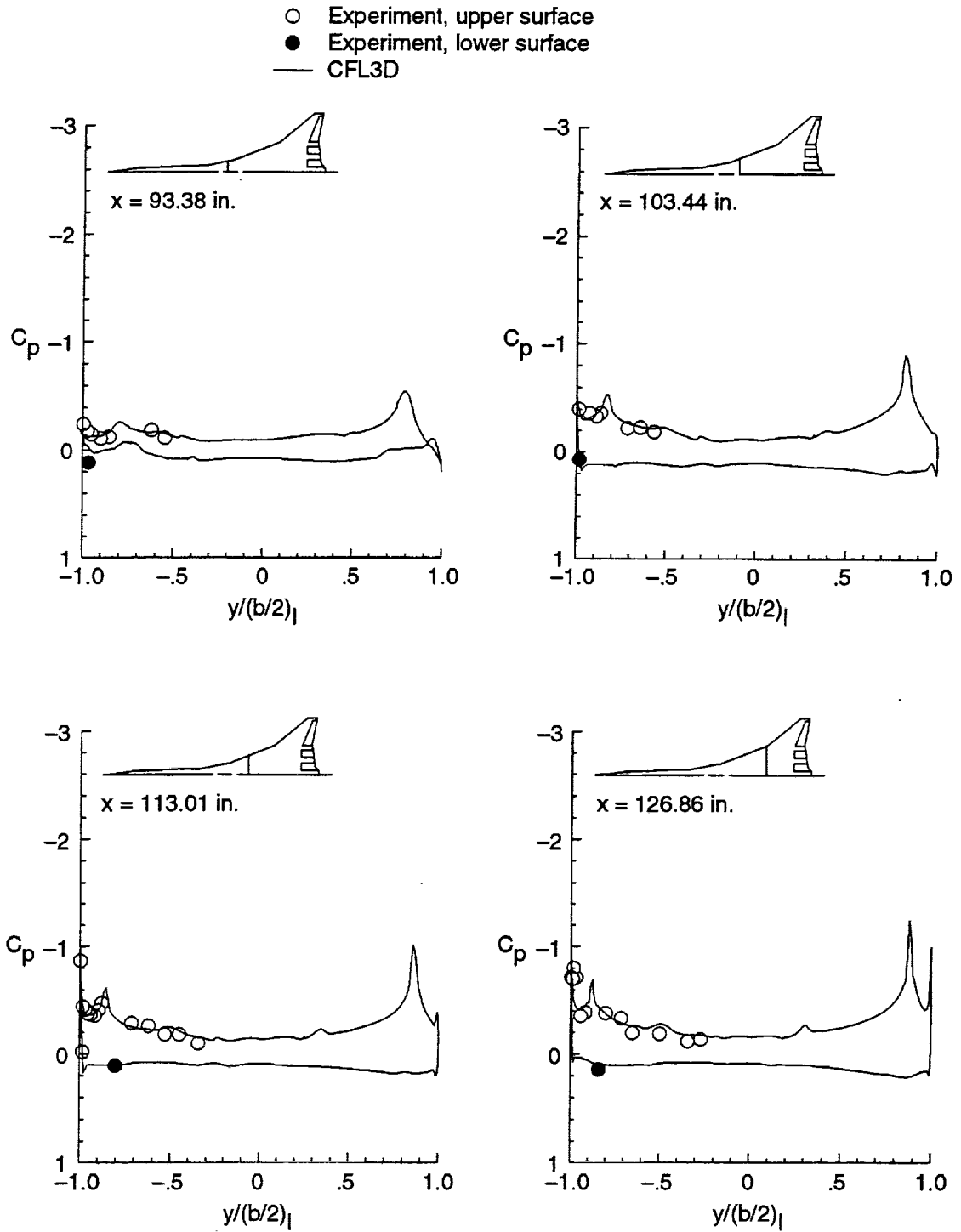


Figure 42. Spanwise distributions of experimental and computational  $C_p$  for Reference H config3 at  $M = 0.24$ ,  $\alpha = 8^\circ$ , and  $\beta = 6^\circ$ .

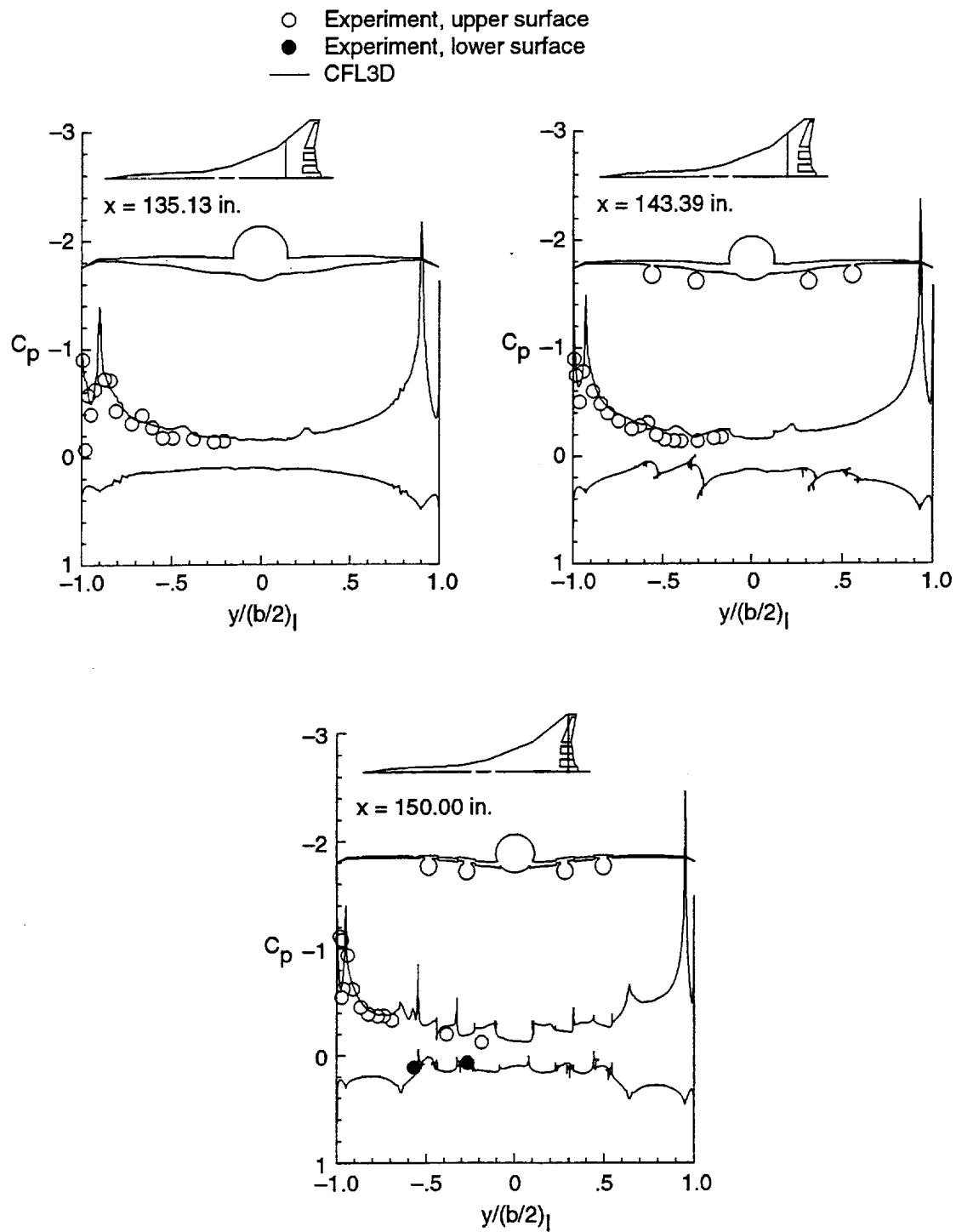


Figure 42. Concluded.

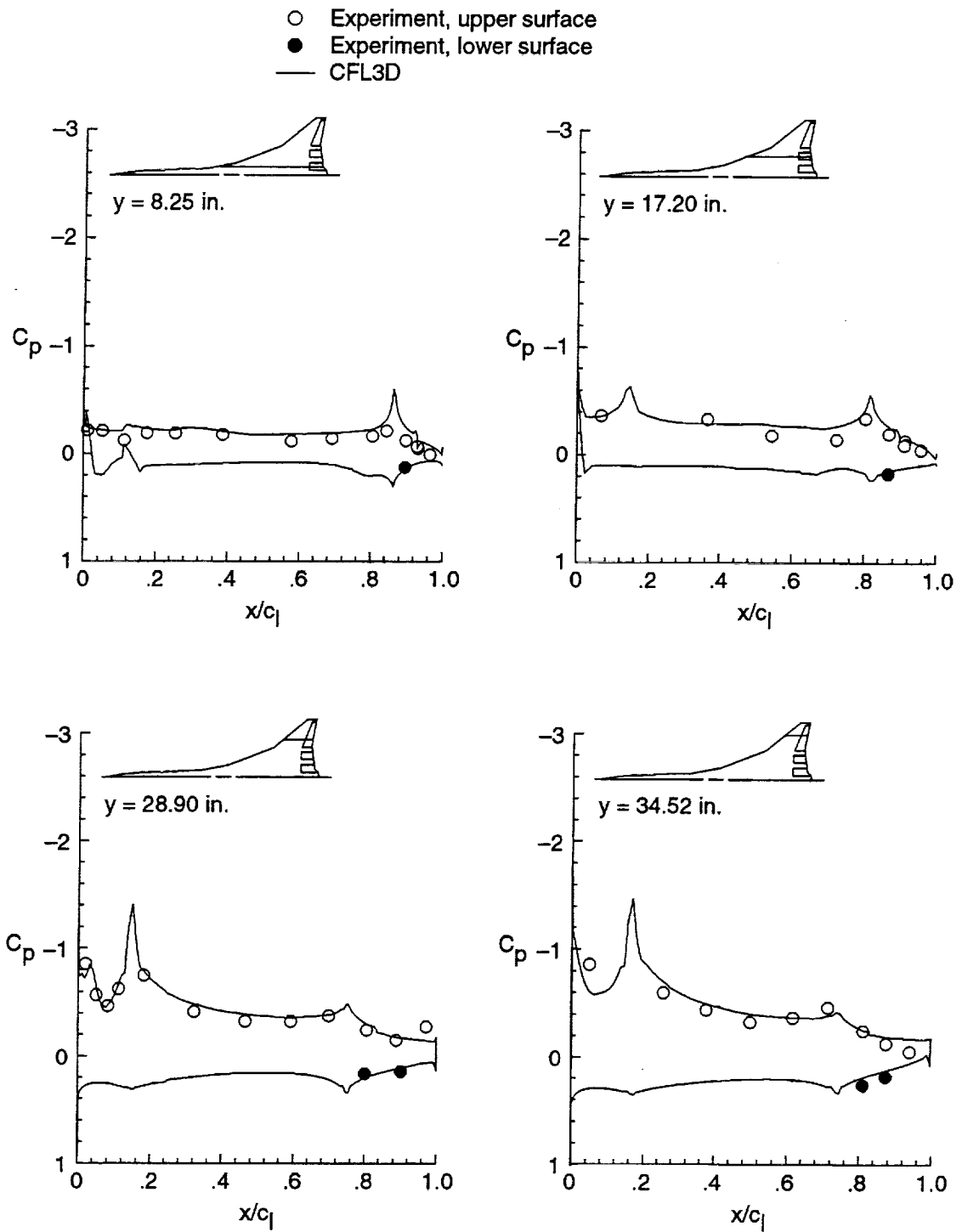


Figure 43. Streamwise distributions of experimental and computational  $C_p$  for Reference H config3 at  $M = 0.24$ ,  $\alpha = 8^\circ$ , and  $\beta = 6^\circ$ .

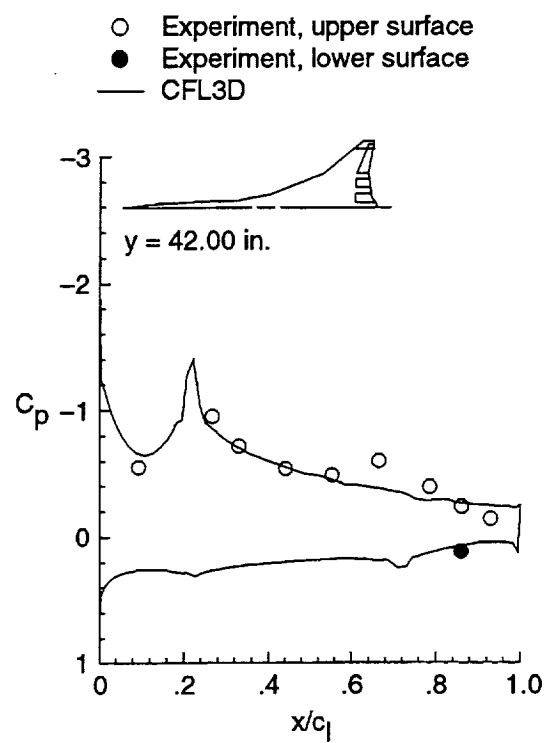


Figure 43. Concluded.

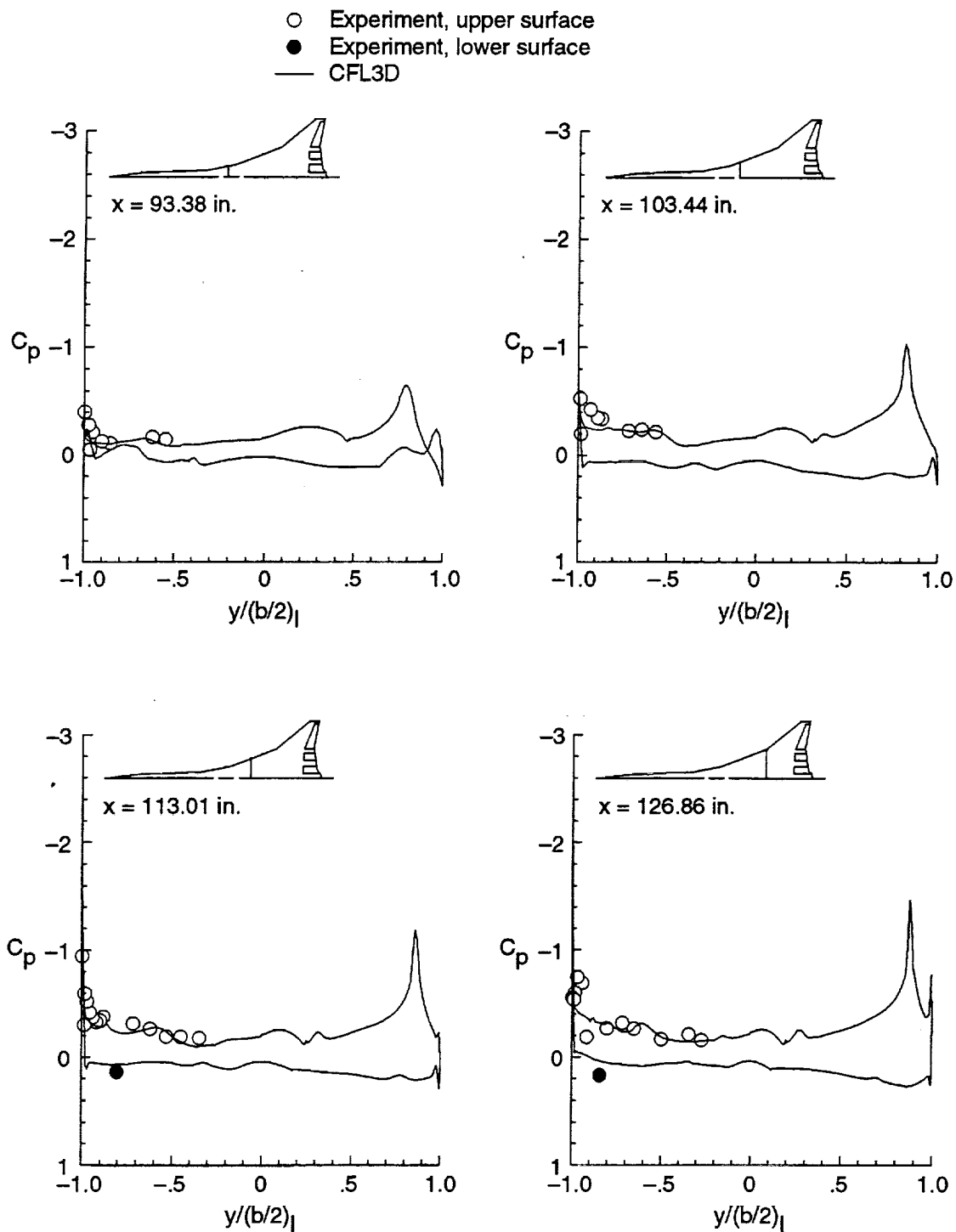


Figure 44. Spanwise distributions of experimental and computational  $C_p$  for Reference H config3 at  $M = 0.24$ ,  $\alpha = 8^\circ$ , and  $\beta = 12^\circ$ .



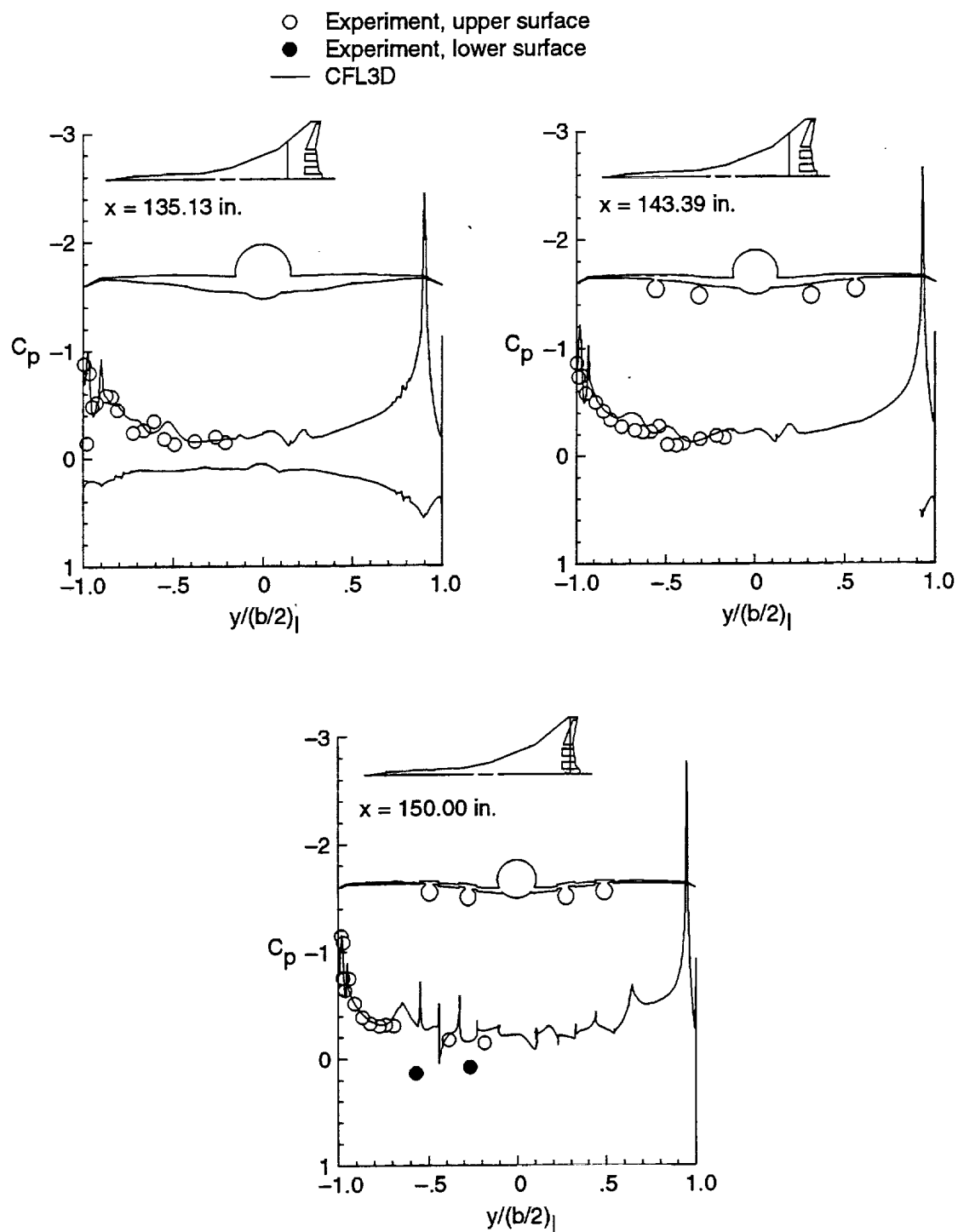


Figure 44. Concluded.

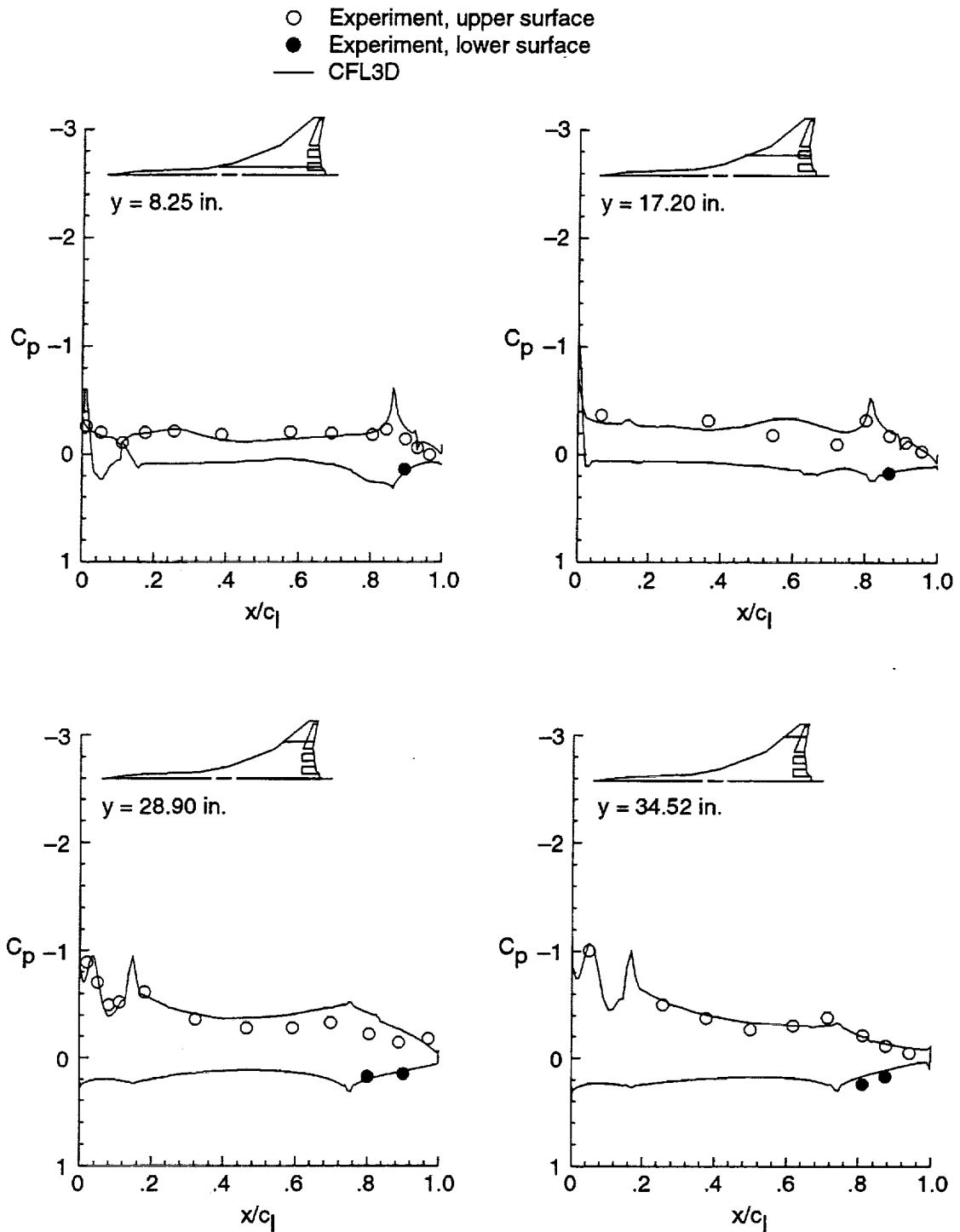


Figure 45. Streamwise distributions of experimental and computational  $C_p$  for Reference H config3 at  $M = 0.24$ ,  $\alpha = 8^\circ$ , and  $\beta = 12^\circ$ .

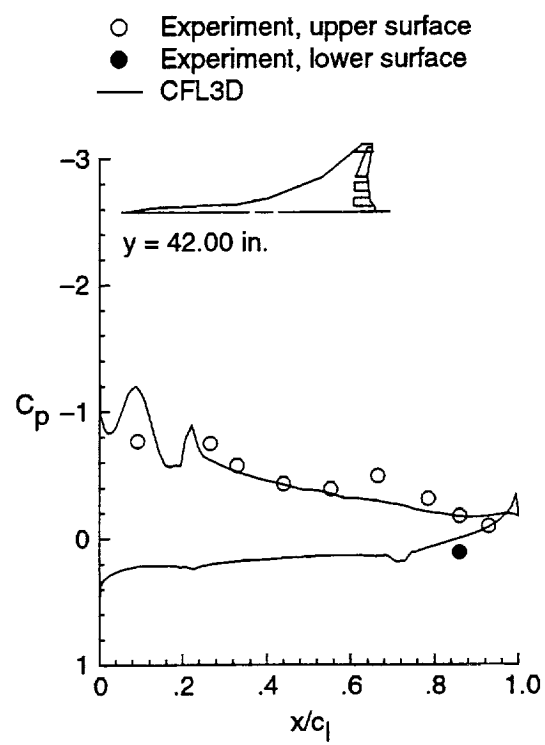


Figure 45. Concluded.

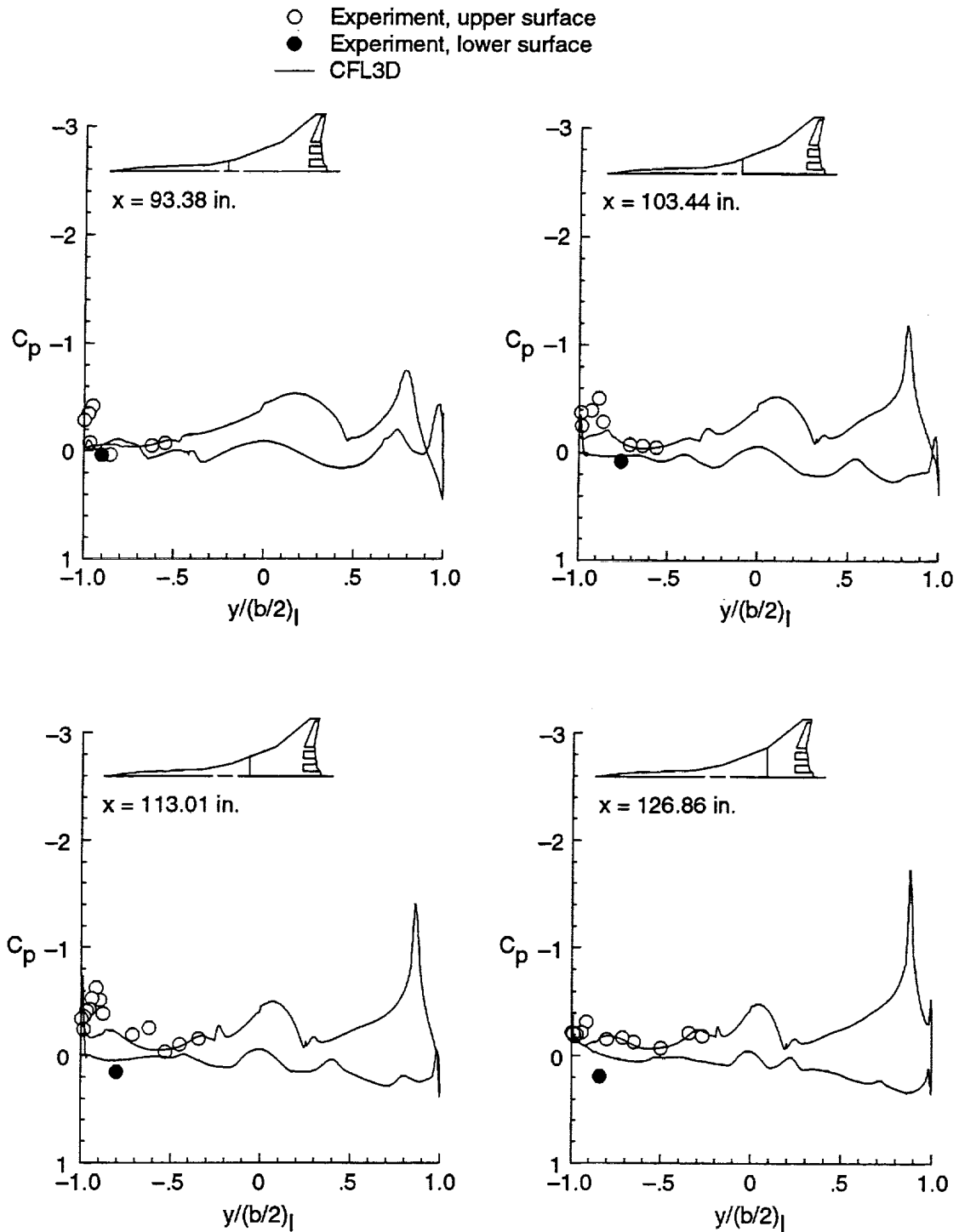


Figure 46. Spanwise distributions of experimental and computational  $C_p$  for Reference H config3 at  $M = 0.24$ ,  $\alpha = 8^\circ$ , and  $\beta = 18^\circ$ .

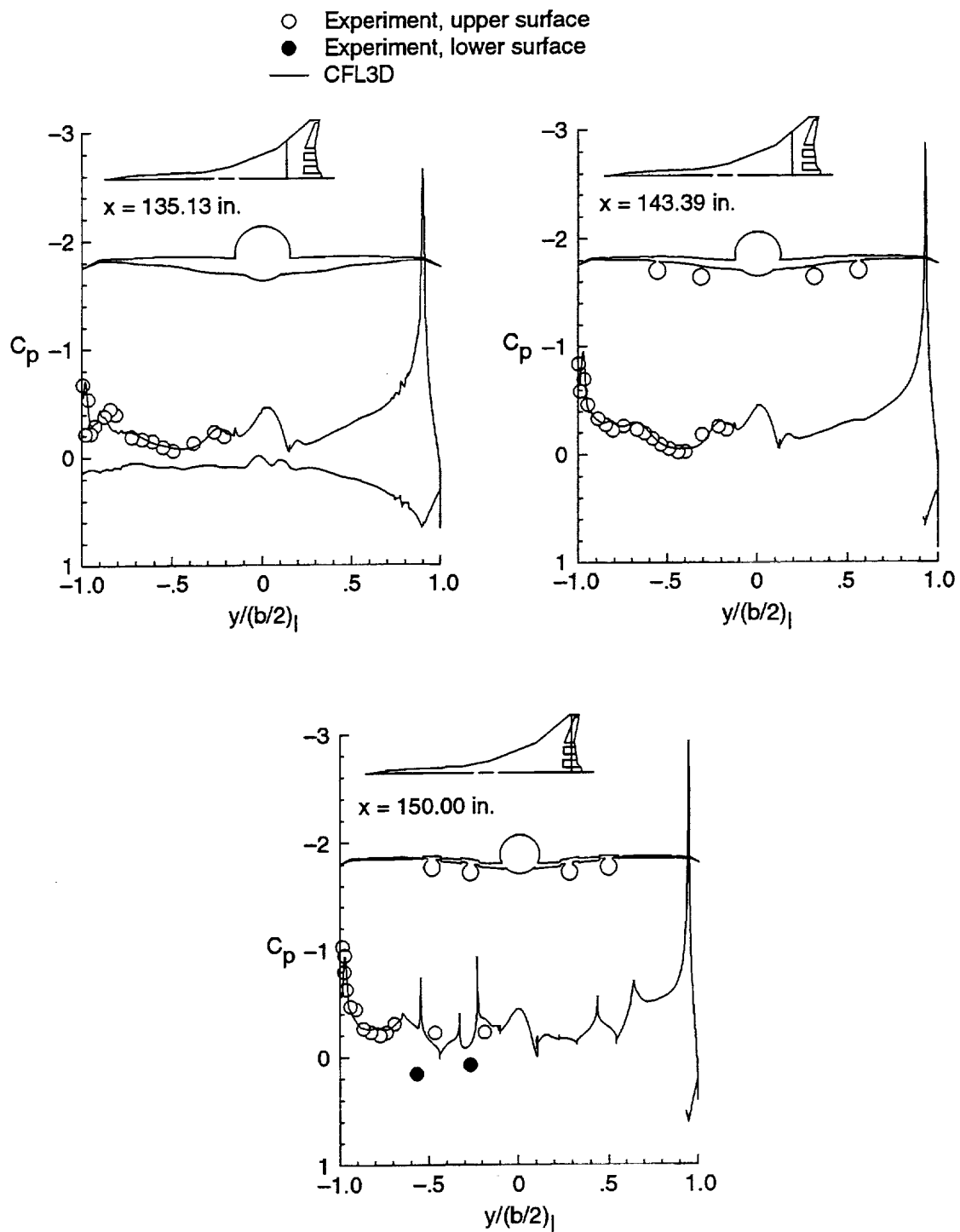


Figure 46. Concluded.

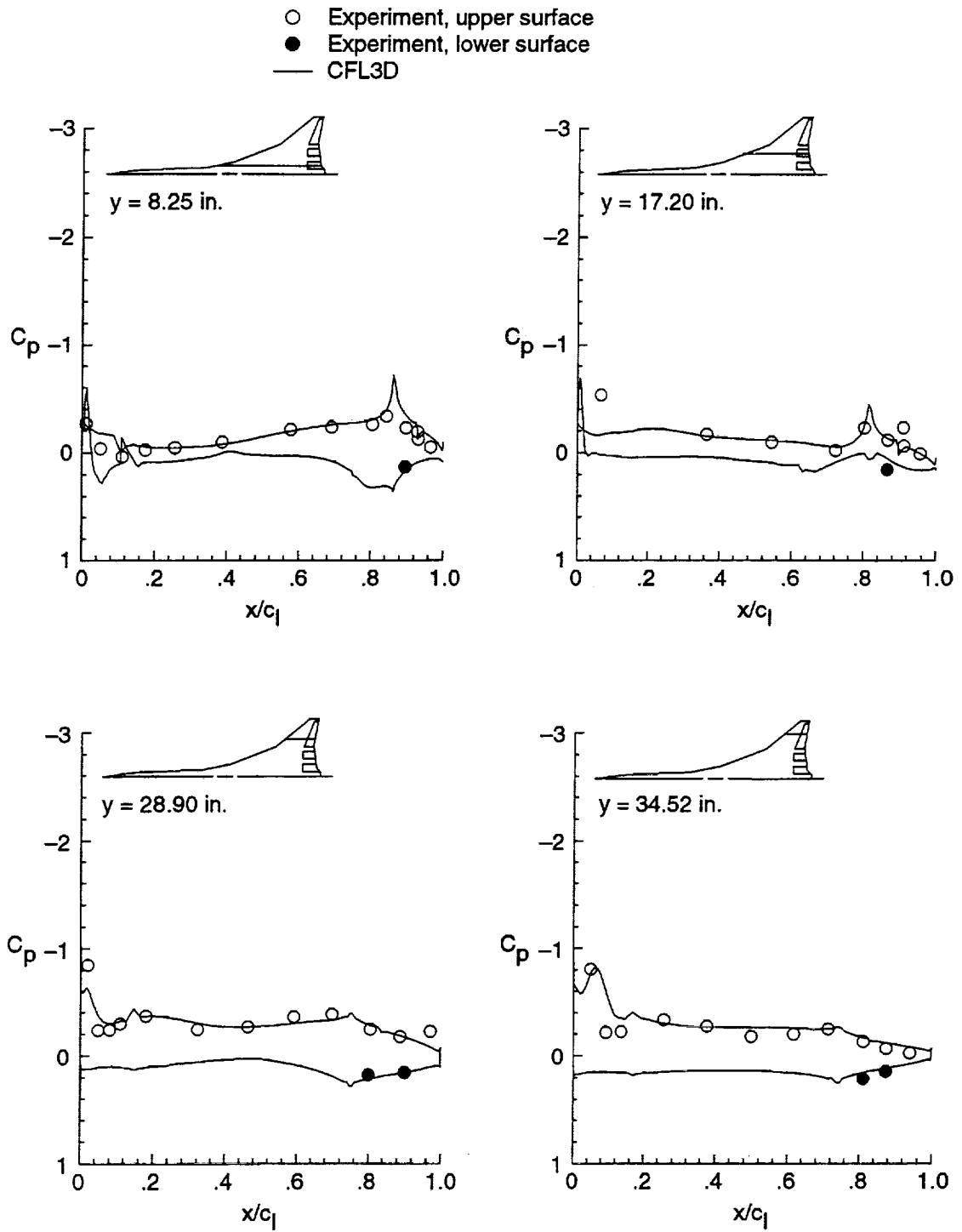


Figure 47. Streamwise distributions of experimental and computational  $C_p$  for Reference H config3 at  $M = 0.24$ ,  $\alpha = 8^\circ$ , and  $\beta = 18^\circ$ .

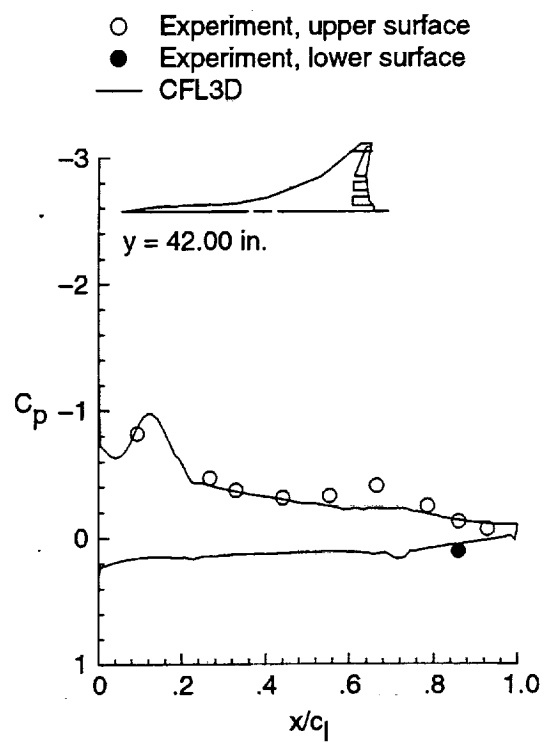


Figure 47. Concluded.

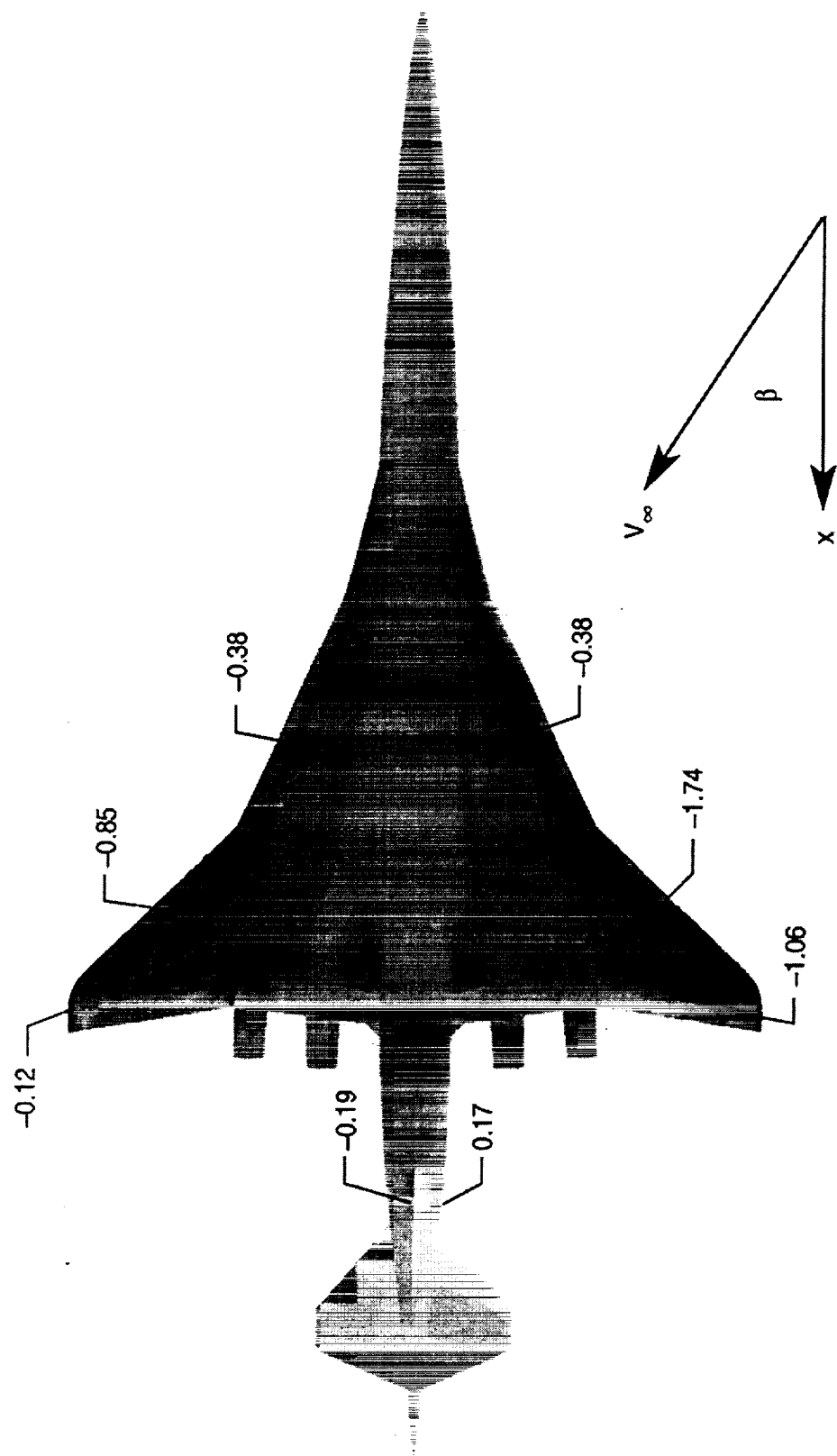


Figure 48. The  $C_p$  contours on surface of Reference H config3 at  $\alpha = 8^\circ$  and  $\beta = 8^\circ$ .



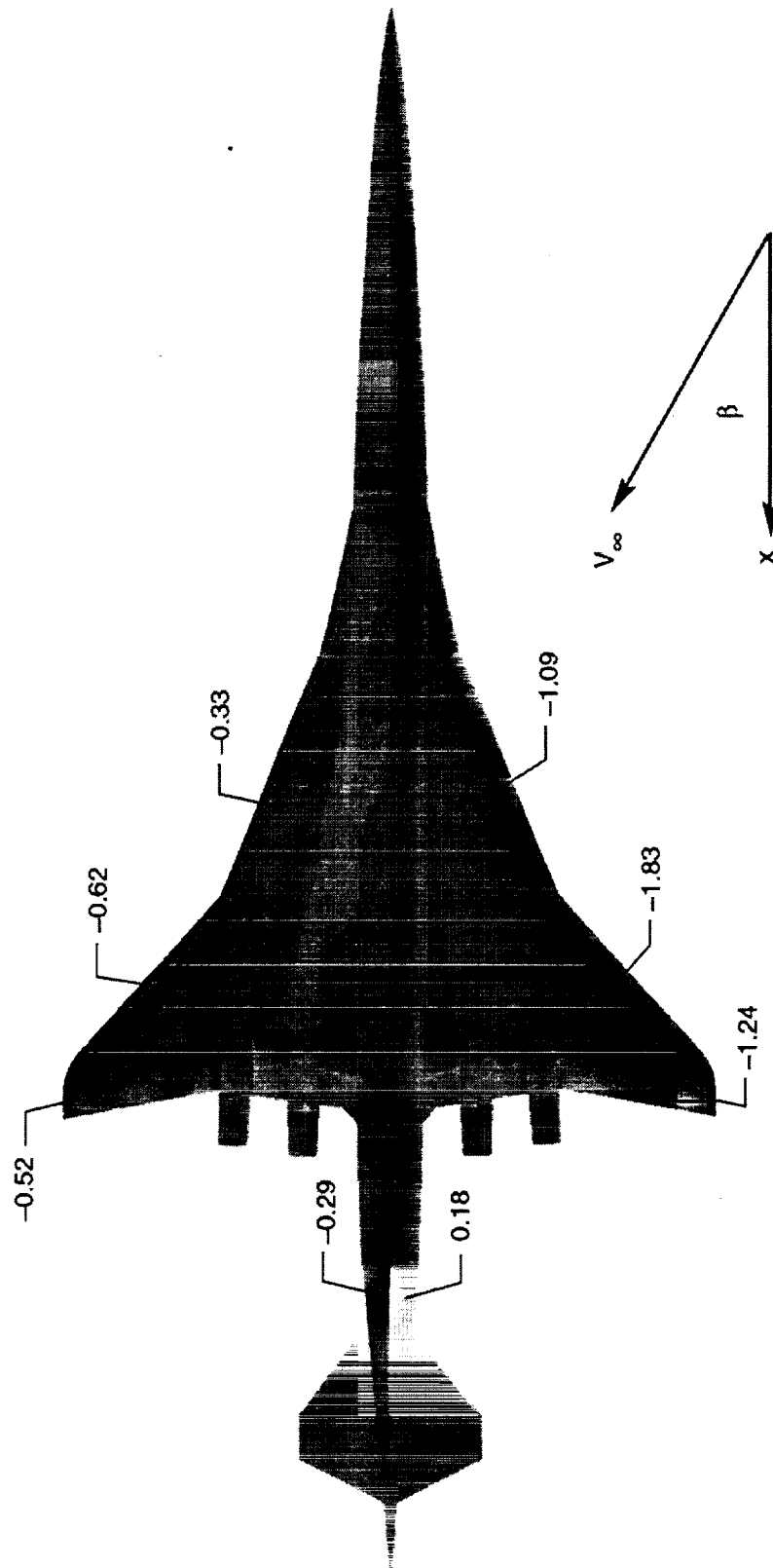


Figure 49. The  $C_p$  contours on surface of Reference H config3 at  $\alpha = 8^\circ$  and  $\beta = 12^\circ$ .

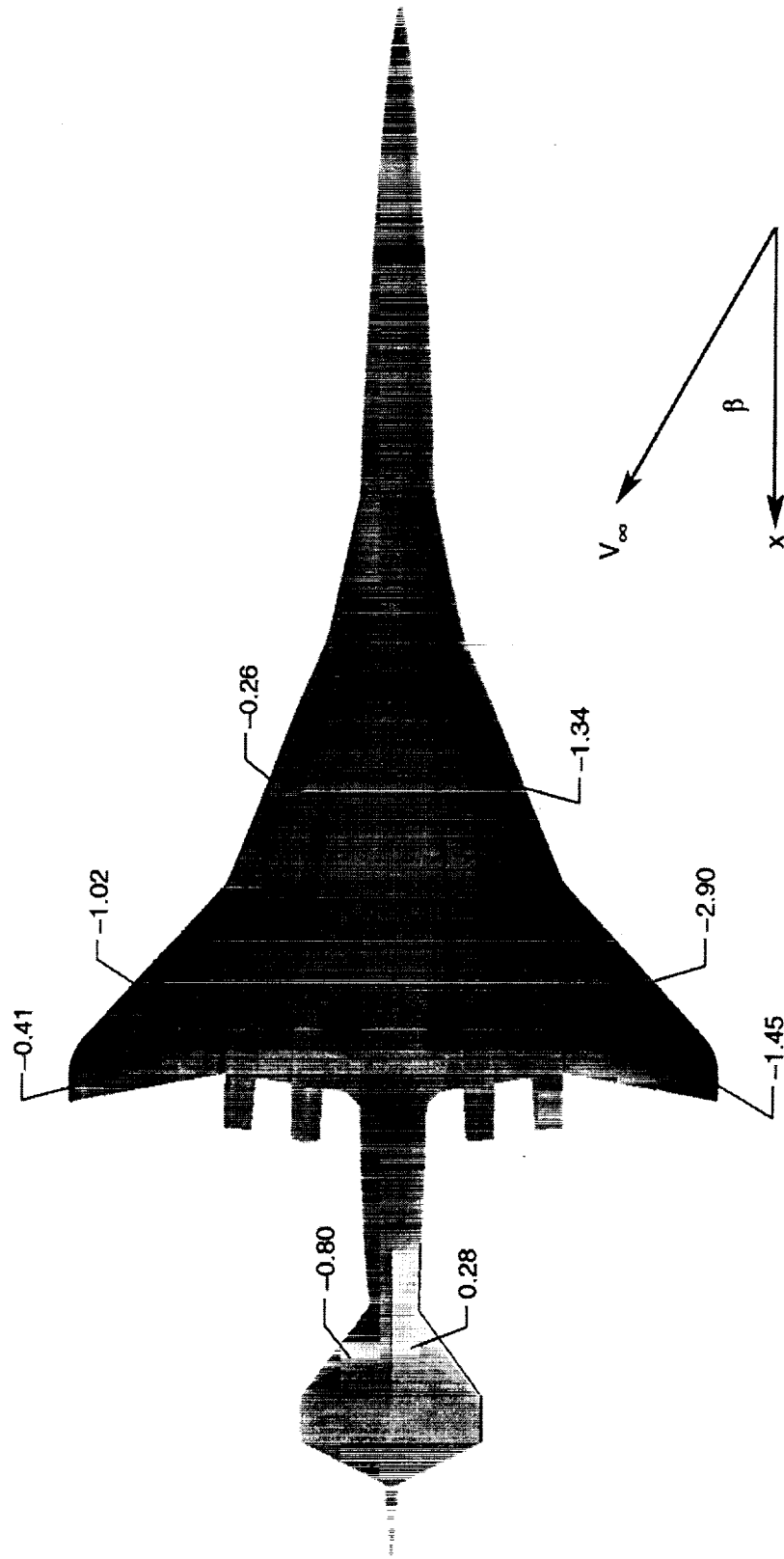


Figure 50. The  $C_p$  contours on surface of Reference H config3 at  $\alpha = 8^\circ$  and  $\beta = 18^\circ$ .

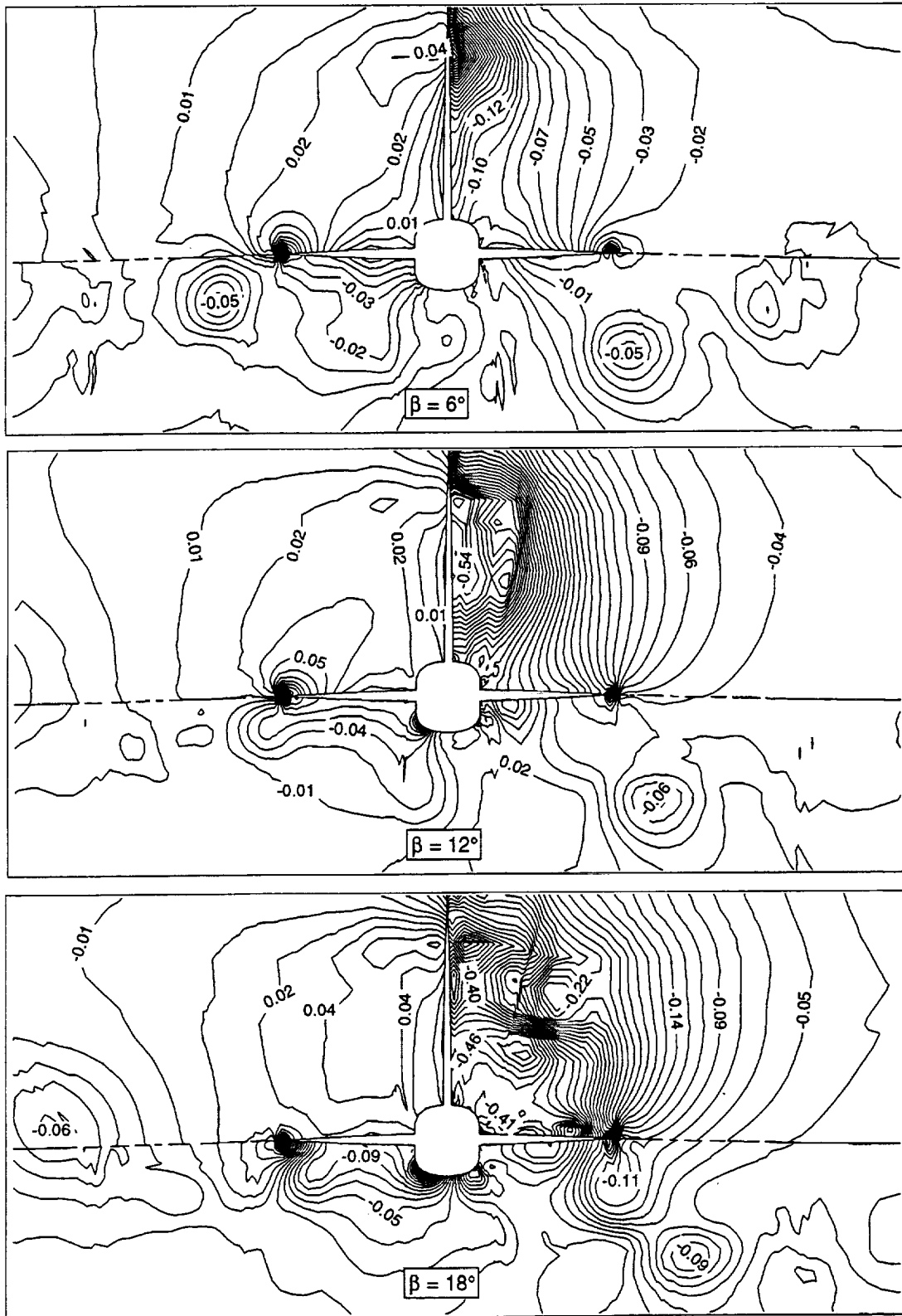


Figure 51. The  $C_p$  contours about empennage as viewed from front of config3 at  $x = 200$  in. and  $\alpha = 8^\circ$ .

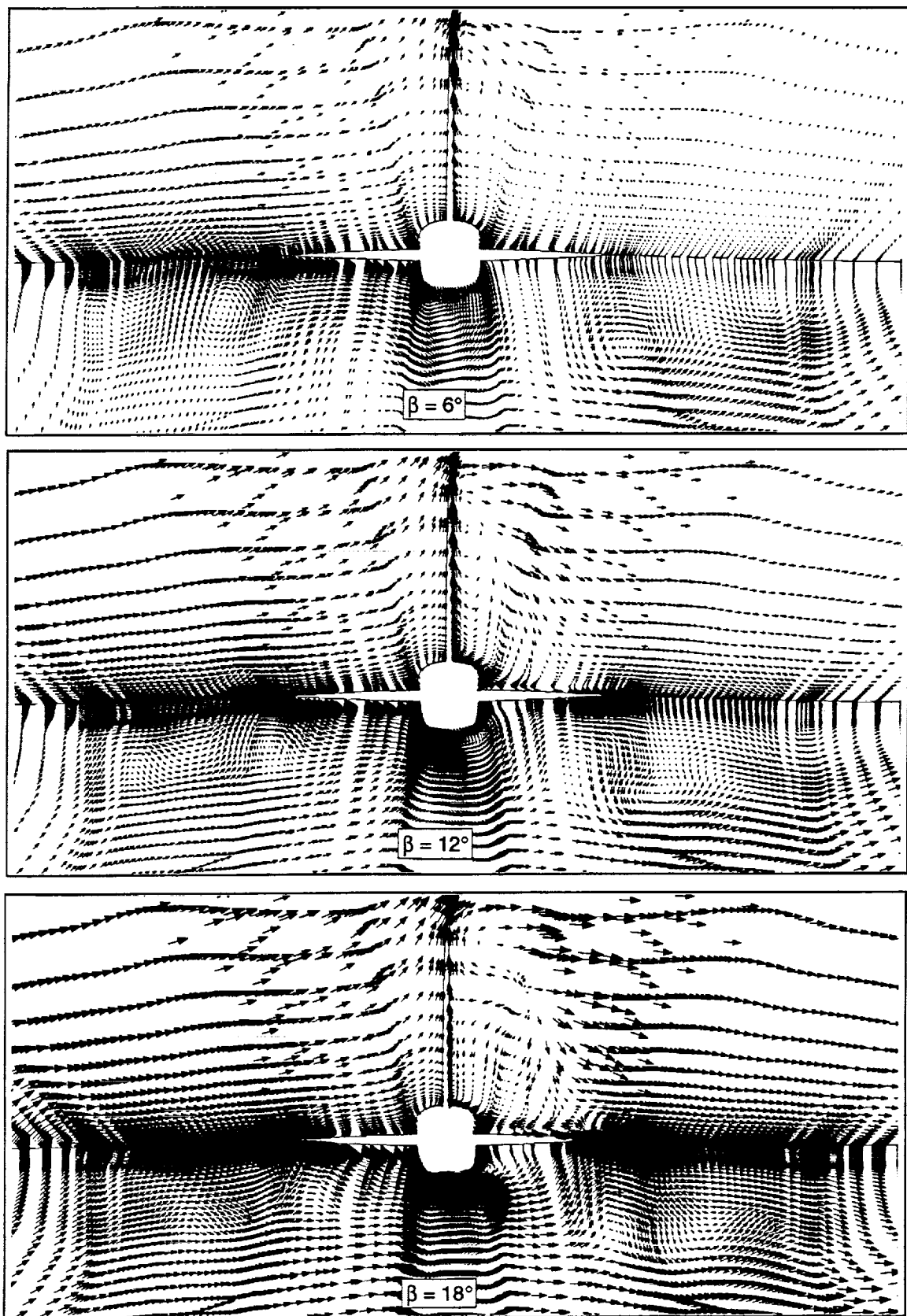


Figure 52. The  $C_p$  velocity vectors about empennage as viewed from front of config3 at  $x = 200$  in. and  $\alpha = 8^\circ$ .

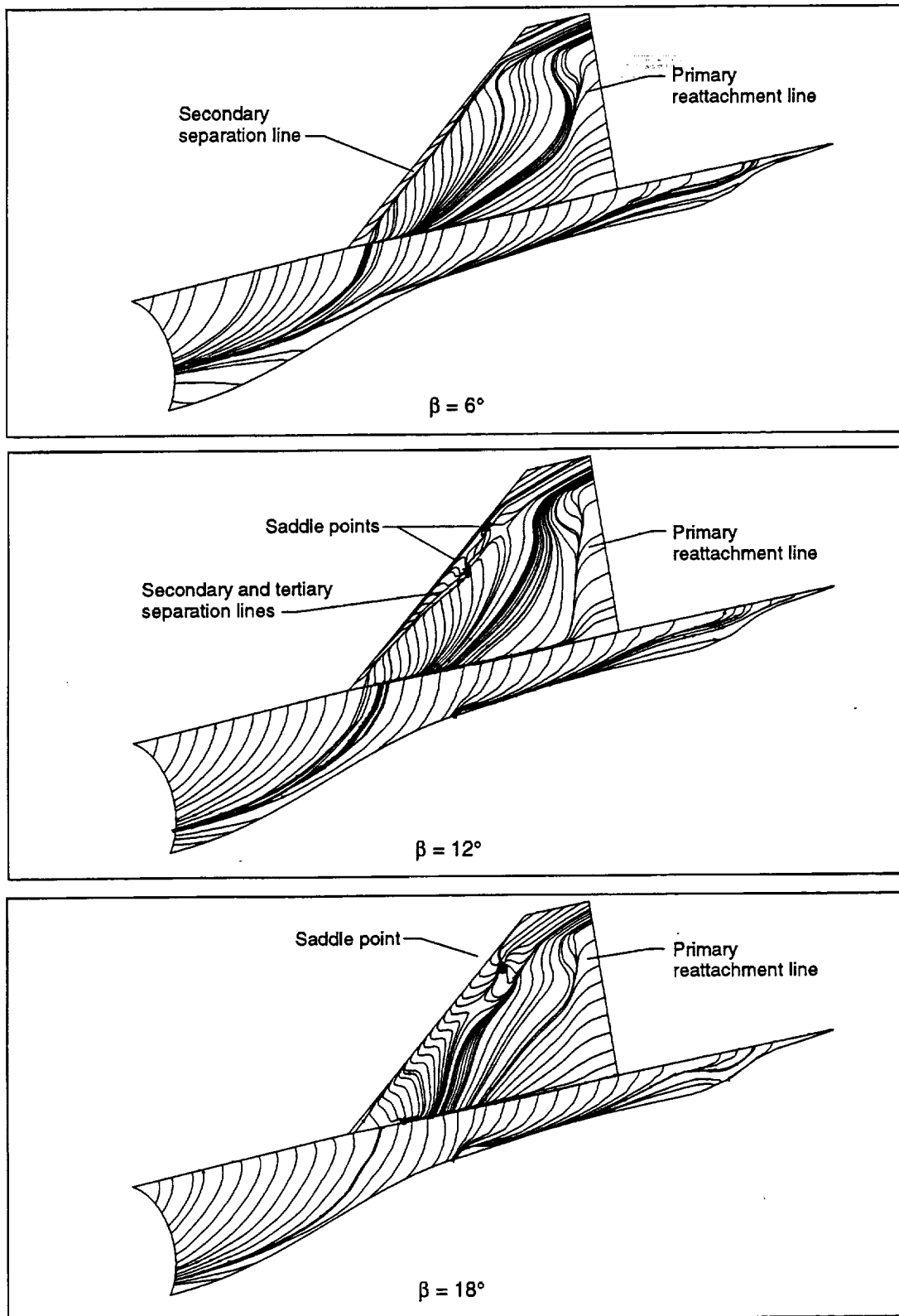


Figure 53. Surface streamlines on left side of vertical tail and fuselage for config3 at  $\alpha = 8^\circ$ .

REPORT DOCUMENTATION PAGE			Form Approved OMB No. 0704-0188	
Public reporting burden for this collection of information is estimated to average 1 hour per response, including the time for reviewing instructions, searching existing data sources, gathering and maintaining the data needed, and completing and reviewing the collection of information. Send comments regarding this burden estimate or any other aspect of this collection of information, including suggestions for reducing this burden, to Washington Headquarters Services, Directorate for Information Operations and Reports, 1215 Jefferson Davis Highway, Suite 1204, Arlington, VA 22202-4302, and to the Office of Management and Budget, Paperwork Reduction Project (0704-0188), Washington, DC 20503.				
1. AGENCY USE ONLY (Leave blank)	2. REPORT DATE December 1999	3. REPORT TYPE AND DATES COVERED Technical Publication		
4. TITLE AND SUBTITLE Navier-Stokes Simulation of Several High-Lift Reference H Configurations		5. FUNDING NUMBERS WU 537-07-22-02		
6. AUTHOR(S) Wendy B. Lessard				
7. PERFORMING ORGANIZATION NAME(S) AND ADDRESS(ES) NASA Langley Research Center Hampton, VA 23681-2199		8. PERFORMING ORGANIZATION REPORT NUMBER L-17636		
9. SPONSORING/MONITORING AGENCY NAME(S) AND ADDRESS(ES) National Aeronautics and Space Administration Washington, DC 20546-0001		10. SPONSORING/MONITORING AGENCY REPORT NUMBER NASA/TP-1999-209541		
11. SUPPLEMENTARY NOTES				
12a. DISTRIBUTION/AVAILABILITY STATEMENT Unclassified-Unlimited Subject Category 02 Availability: NASA CASI (301) 621-0390		12b. DISTRIBUTION CODE Distribution: Nonstandard		
13. ABSTRACT (Maximum 200 words) The subsonic flow field was numerically simulated around several High Speed Research Reference H configurations at various pitch and yaw angles. A sequence of structured-viscous grids were generated; the first grid modeled the wing-body high-lift geometry, and the second grid incorporated the nacelles and the horizontal tail. The third grid modeled the full-span geometry for sideslip calculations, and was obtained by mirroring a coarser version of the second grid. The CFL3D code, a Reynolds averaged, thin-layer Navier-Stokes flow solver for structural grids, was used for the flow solver and modeled the free-air Reference H high-lift configuration at wind tunnel conditions of Mach number 0.24 and Reynolds number of $1.4 \times 10^5$ per in. Pitch sweeps were performed at angles of attack from $6^\circ$ to $15^\circ$ . Sideslip angle sweeps at $0^\circ \leq \beta \leq 18^\circ$ were performed at an angle of attack of $8^\circ$ . The lateral and longitudinal performance characteristics were well predicted and very good force and moment comparisons were obtained. A very complex multiple vortical system develops at the higher angles of attack, and detailed postprocessing of the solutions provided a comprehensive three-dimensional understanding of the flow which helps to correlate and interpret the wind tunnel data.				
14. SUBJECT TERMS High-speed civil transport; High speed supersonic transport			15. NUMBER OF PAGES 94	
			16. PRICE CODE A05	
17. SECURITY CLASSIFICATION OF REPORT Unclassified	18. SECURITY CLASSIFICATION OF THIS PAGE Unclassified	19. SECURITY CLASSIFICATION OF ABSTRACT Unclassified	20. LIMITATION OF ABSTRACT UL	